

University of Alberta

Preparation and Characterization of Electrolyte Materials for Proton
Conducting Fuel Cells

by

Stephen B. Gibson

A thesis submitted to the Faculty of Graduate Studies and Research
in partial fulfillment of the requirements for the degree of

Master of Science

in

Materials Engineering

Department of Chemical and Materials Engineering

©Stephen B. Gibson

Spring 2012

Edmonton, Alberta

Permission is hereby granted to the University of Alberta Libraries to reproduce single copies of this thesis and to lend or sell such copies for private, scholarly or scientific research purposes only. Where the thesis is converted to, or otherwise made available in digital form, the University of Alberta will advise potential users of the thesis of these terms.

The author reserves all other publication and other rights in association with the copyright in the thesis and, except as herein before provided, neither the thesis nor any substantial portion thereof may be printed or otherwise reproduced in any material form whatsoever without the author's prior written permission.

Abstract

Experiments were conducted to test and characterize proton conducting electrolyte materials and layers formed by solid state reactions. Screen printed layers of yttrium doped ceria and alkaline earth carbonates were reacted at high temperatures on NiO-YSZ and NiO-CGO substrates with the intent of forming thin and dense $A^{2+}B^{4+}O_3$ based perovskite layers. The layers were investigated and characterized using scanning electron microscopy, energy dispersive x-ray spectroscopy and x-ray diffraction analysis. The influence of dopant (M = Nd, Eu, Gd, Y, Yb) and atmosphere on the protonic conductivity of sintered $BaCe_{0.5}Zr_{0.4}M_{0.1}O_{2.95}$ pellets was investigated through impedance spectroscopy.

The layer synthesis method showed promise for producing thin and dense layers of barium and strontium cerates as well as barium, strontium and calcium zirconates. The perovskite tolerance factor, a measure of the deviation from the cubic lattice, seems to correlate to the selective reactivity in the layer synthesis. Proton conduction was found to be predominant in hydrogen containing atmospheres in the low to intermediate temperature range (300-600°C) with increased competition from alternative charge carriers as temperature increased. The highest protonic conduction was found in Yb doped $BaCe_{0.5}Zr_{0.4}M_{0.1}O_{2.95}$ samples. Dopants with smaller ionic radii resulted in improved tolerance factors, decreased likelihood of A-site doping and higher conductivities.

Acknowledgments

To be succinct, I simply would not be writing the acknowledgement section of my graduate thesis if it were not for the assistance, support and opportunities provided by others.

Let me start from the very beginning. I would like to thank Alex Harmer for suggesting and initiating the opportunity for me to travel to Germany and to the Forshungszentrum Jülich. I was paired there with the most understanding, patient and helpful supervisor, Dr. Mariya Ivanova. I would also like to thank all of my colleagues from the Forshungszentrum who were all so friendly, welcoming and helpful. I especially wish to express my gratitude to Dr. Wilhelm Meulenberg for providing me the opportunity for my nine month research project, Mirko Ziegner for XRD analysis, Dr. Doris Sebold for her SEM analysis, and to the machine shop workers who suffered through all of my broken and lost bicycles without complaint. It was a time I will never forget and was made all the better through the friendships. To Sean Prestie, Andreas Hospach, Felix Hauler, Dorothee Mönch, Bryan O'Connell, Marius Dederichs, Manuel Kohl and all the other wonderful people I met; you made life and work exciting.

Moving back to the University of Alberta, I would like to thank my professor, Dr. Tom Etsell, for all his help, knowledge and enthusiasm for this research collaboration. Without his support from the beginning, none of this would have happened. I would also like to thank Dr. Partha Sarkar and Luis Yamarte for their generosity in sharing their time, knowledge and laboratory equipment. I would like to express my sincerest gratitude to Shiraz Mirali, whose XRD analysis and scientific knowledge were irreplaceable. I would like to thank my fellow grad students, Patrick Kerr, Marc Parent and Kevin Scott, for all the help, discussions and breakfast meetings.

Lastly, I would like to thank my family for their patience, support and encouragement throughout the entirety of this project.

Contents

1.0	Introduction	1
2.0	Background	4
2.1	Proton Conducting Fuel Cells (PCFC).....	4
2.2	PCFC Electrolyte Materials	5
2.3	Synthesis Methods	6
2.3.1	Powder Synthesis	6
2.3.2	Supported Membrane Synthesis	8
3.0	Theory.....	10
3.1	Ceramic Structures of Interest	10
3.1.1	Fluorite Structure	10
3.1.2	Perovskite Structure	11
3.2	Electrical Conductivity in a Solid	13
3.2.1	Ionic Conduction	14
3.2.2	Proton Chemistry and Conduction Mechanisms	15
3.3	Characterization Methods.....	21
3.3.1	Electrochemical Measurements	21
3.3.2	X-Ray Diffraction (XRD)	23
3.3.3	Differential Thermal Analysis/Thermogravimetry (DTA/TG).....	23
3.3.4	Particle Size Analysis	24
3.3.5	Scanning Electron Microscopy/Energy Dispersive X-Ray Spectroscopy.....	24
3.3.6	Laser Surface Scanning	25

4.0	Experimental.....	26
4.1	Powder Synthesis	27
4.1.1	Doped Ceria Synthesis	27
4.1.2	Doped Cerate Perovskite Synthesis	27
4.1.3	Doped Barium Cerate-Zirconate Synthesis.....	28
4.1.4	Powder Characteriztion	29
4.2	Sintered Bar and Pellet Synthesis	30
4.2.1	Bars	30
4.2.2	Pellets.....	30
4.2.3	Bar and Pellet Characterization	32
4.3	Electrochemical Testing	33
4.4	Supported Membrane Synthesis.....	35
4.4.1	Support (Substrate) Synthesis	35
4.4.2	Layer Screen Printing and Synthesis	35
4.4.3	Membrane Characterization.....	36
5.0	Results and Discussion.....	37
5.1	Cerate Synthesis.....	37
5.1.1	Dopant Solubility.....	37
5.2	Doped Cerate Perovskite Synthesis	40
5.3	Supported Layer Synthesis.....	48
5.3.1	Paste Preparation, Screen Printing, and Synthesis.....	48
5.3.2	NiO-8YSZ Substrates	49

5.3.3	CGO-NiO Substrates.....	65
5.4	Doped Cerate-Zirconate Synthesis.....	76
5.4.1	Solid State Synthesis	79
5.4.2	Powder Size Reduction	82
5.4.3	Pellet Fabrication and Sintering.....	86
5.4.4	Conductivity	90
6.0	Summary.....	105
7.0	Conclusions.....	109
8.0	Suggestions for Future Work.....	110
	Bibliography	113
	Appendix I: EDX Analysis.....	122
	Appendix II: Additional Conductivity and Impedance Data.....	136

List of Tables

Table 1: Commercially obtained chemicals (powders).....	26
Table 2: Heat treatments.....	27
Table 3: Summary of heat treatments used for barium cerate-zirconate samples	29
Table 4: Doped ceria compositions and summary of XRD results.....	38
Table 5: Perovskite synthesis starting powders and particle sizes.....	40
Table 6: Attempts at perovskite synthesis via DCC method.....	43
Table 7: Mixed oxide method perovskite synthesis	44
Table 8: Density and porosity data for a sintered BaY10 bar	48
Table 9: Prepared pastes	48
Table 10: Screen printed samples on NiO-8YSZ substrates.....	50
Table 11: Screen printed samples on NiO-CGO substrates	65
Table 12: Ionic radii of selected relevant species.....	78
Table 13: Perovskite tolerance factors for the barium cerate-zirconate compositions.....	78
Table 14: Synthesis methods and densities of final sintered samples for conductivity measurements	89
Table 15: Conductivities of all compositions in different atmospheres at different temperatures	96
Table 16: Low temperature activation energies.....	98

Table of Figures

Figure 1: Schematic of a proton conducting fuel cell	5
Figure 2: Schematic diagram of the procedure for producing thin-film BaCe _{0.8} Gd _{0.2} O _{3-δ} membranes [32]	8
Figure 3: The fluorite (AO ₂) oxide structure. The red spheres represent the A cation sites and the blue spheres the oxygen sites [52].....	10
Figure 4: Schematic of the perovskite structure with oxygen as the anion [23]	12
Figure 5: Proton translocation mechanism involving reorientation of H ₂ O [55,62]	18
Figure 6: Energy profile for H ⁺ transport in the translocation model [55]	19
Figure 7: Effect of the orthorhombic distortion of BaCeO ₃ and SrCeO ₃ on the basicity of O1 and O2 (basicity indicated by the darkness of the oxygens). The arrows indicate the predominant proton transfers [11].....	21
Figure 8: (A) Arrangement of the impedance measurement system consisting of sample holder (1), gas mixer (2), furnace (3), frequency analyzer (4) with 4-wire interface (5), (B) a detailed inner view of the Probostat™ sample holder and (C) a schematic of the measurement circuit [69].....	34
Figure 9: Schematic of the screen printing process [70]	36
Figure 10: XRD results from sample CeGd10.....	39
Figure 11: XRD results from sample CeSm10	39
Figure 12: XRD results from sample CeSm15	39
Figure 13: XRD results from sample CeSm20	39
Figure 14: XRD results from sample CeY10.....	39
Figure 15: XRD results from sample CeY15.....	39

Figure 16: XRD results from sample CeY20.....	40
Figure 17: XRD analysis of commercially obtained CeGd20 nanopowder	40
Figure 18: DTA for reaction of $Ce_{0.90}Gd_{0.10}O_{1.95}$ with $CaCO_3$	41
Figure 19: DTA for reaction of $Ce_{0.90}Gd_{0.10}O_{1.95} + CaCO_3 + Al_2O_3$	42
Figure 20: DTA for reaction of $Ce_{0.90}Gd_{0.10}O_{1.95} + CaCO_3 + ZrO_2$	42
Figure 21: XRD results from BaY10 sample (MO, Perovskite3)	45
Figure 22: XRD results from BaY15 sample with marked peaks indicating the presence of a monoclinic phase (MO, Perovskite3)	45
Figure 23: XRD results from BaY20 sample with marked peaks indicating the presence of a monoclinic phase (MO, Perovskite3)	45
Figure 24: XRD results from BaSm10 sample (MO, Perovskite3)	45
Figure 25: XRD results from BaGd10 sample (MO, Perovskite3).....	46
Figure 26: XRD results from CaY10 (MO, Perovskite3).....	46
Figure 27: XRD results for sample CaY10 (MO, Perovskite3+Perovskite1)	46
Figure 28: XRD results for sample SrY10 (MO, Perovskite3)	46
Figure 29: XRD results for sample SrY10 (MO, Perovskite3+Perovskite1)	47
Figure 30: XRD results for samples SrY10 (TO, Perovskite1)	47
Figure 31: Sintered BaY10 bars	47
Figure 32: SEM cross-section of a NiO-8YSZ substrate	49
Figure 33: Laser topography data for the CeY10 dried first layer	51
Figure 34: Laser topography data for the CeY10 sintered first layer	52
Figure 35: Sintered CeY10 first layer on NiO-8YSZ substrate	53
Figure 36: SEM cross-sections of sintered CeY10 first layer on NiO-8YSZ substrate	54

Figure 37: Photographs of samples: (a) BCY10-2020-YSZ and (b) BCY10-2040-YSZ.....	55
Figure 38: SEM micrographs of samples: (a-b) BCY10-2020-YSZ and (c-d) BCY10-2040-YSZ	56
Figure 39: XRD analysis of the surface of sample BCY10-2020-YSZ.....	57
Figure 40: Photographs of samples: (a) SCY10-2020-YSZ and (b) SCY10-2040-YSZ.....	58
Figure 41: SEM micrographs of samples: (a-b) SCY10-2020-YSZ and (c-d) SCY10-2040-YSZ	60
Figure 42: XRD analysis of the surface of sample SCY10-2020-YSZ.....	61
Figure 43: Photographs of samples: (a) CCY10-2020-YSZ and (b) CCY10-2040-YSZ.....	62
Figure 44: SEM micrographs of samples: (a-b) CCY10-2020-YSZ and (c-d) CCY10-2040-YSZ	63
Figure 45: XRD analysis of the surface of sample CCY10-2020-YSZ.....	64
Figure 46: SEM cross-section of a NiO-8YSZ substrate.....	65
Figure 47: Sintered CeY10 first layer on CGO-NiO substrate.....	66
Figure 48: SEM cross-sections of sintered CeY10 first layer on NiO-CGO substrate	67
Figure 49: Photographs of samples: (a) BCY10-2020-CGO and (b) BCY10-2040-CGO.....	67
Figure 50: SEM micrographs of samples: (a-b) BCY10-2020-CGO and (c-d) BCY10-2040-CGO	69
Figure 51: XRD analysis of the surface of sample BCY10-2020-CGO	70
Figure 52: Photographs of samples: (a) SCY10-2020-CGO and (b) SCY10-2040-CGO.....	71
Figure 53: SEM micrographs of samples: (a-b) SCY10-2020-CGO and (c-d) SCY10-2040-CGO.....	72

Figure 54: XRD analysis of the surface of sample SCY10-2020-CGO	73
Figure 55: Photographs of samples: (a) CCY10-2020-CGO and (b) CCY10-2040-CGO	74
Figure 56: SEM micrographs of samples: (a-b) CCY10-2020-CGO and (c-d) CCY10-2040-CGO	75
Figure 57: XRD analysis of the surface of sample CCY10-2020-CGO	76
Figure 58: Plot of tolerance factor vs. dopant ionic radii for the barium cerate-zirconate compositions	79
Figure 59: BCZY reacted at 1000°C	80
Figure 60: XRD patterns of BCZY precursor powders reacted at different temperatures	81
Figure 61: XRD patterns of all doped barium cerate-zirconate compositions	82
Figure 62: Particle size analysis of unmilled BCZYb powder (Fraunhofer method)	84
Figure 63: Particle size analysis of planetary ball milled BCZYb powder (Fraunhofer method)	84
Figure 64: Particle size analysis of unmilled BCZYb powder (pseudo-Fraunhofer method)	85
Figure 65: Particle size analysis of planetary ball milled BCZYb powder (pseudo-Fraunhofer method)	85
Figure 66: Comparison of total conductivities of the doped samples in wet Ar-4%H ₂ measured at 126 kHz	92
Figure 67: Comparison of total conductivities of the doped samples in dry Ar-4%H ₂ measured at 126 kHz	93
Figure 68: Comparison of total conductivities of the doped samples in dry Ar measured at 126 kHz	94
Figure 69: Effect of frequency on measured total conductivity (BCZYb in wet Ar-4% H ₂)	94

Figure 70: Comparison of total conductivities of BCZYb in different atmospheres measured at 126 kHz	97
Figure 71: Comparison of total AC conductivities (126 kHz/wet Ar-4%H ₂ /600°C) versus ionic radii of the dopants.....	102
Figure 72: Comparison of total AC conductivities (126 kHz/Wet Ar-4%H ₂ /600°C) versus tolerance factors of the doped compounds.....	102
Figure 73: EDX analysis of sample CeY10-YSZ.....	122
Figure 74: EDX analysis of sample BCY10-2020-YSZ	123
Figure 75: EDX analysis of sample BCY10-2040-YSZ	124
Figure 76: EDX analysis of sample SCY10-2020-YSZ	125
Figure 77: EDX analysis of sample SCY10-2040-YSZ	126
Figure 78: EDX analysis of sample CCY10-2020-YSZ	127
Figure 79: EDX analysis of sample CCY10-2040-YSZ	128
Figure 80: EDX analysis of sample CeY10-CGO	129
Figure 81: EDX analysis of sample BCY10-2020-CGO	130
Figure 82: EDX analysis of sample BCY10-2040-CGO	131
Figure 83: EDX analysis of sample SCY10-2020-CGO	132
Figure 84: EDX analysis of sample SCY10-2040-CGO	133
Figure 85: EDX analysis of sample CCY10-2020-CGO	134
Figure 86: EDX analysis of sample CCY10-2040-CGO	135
Figure 87: AC conductivities of BCZNd in different atmospheres measured at 126 kHz.....	136
Figure 88: AC conductivities of BCZEu in different atmospheres measured at 126 kHz.....	136

Figure 89: AC conductivities of BCZGd in different atmospheres measured at 126 kHz.....	137
Figure 90: AC conductivities of BCZY in different atmospheres measured at 126 kHz.....	137
Figure 91: Low temperature conductivities at 126 kHz in wet Ar/4% H ₂	138
Figure 92: Low temperature conductivities at 126 kHz in dry Ar/4% H ₂	138
Figure 93: Low temperature conductivities at 126 kHz in dry Ar	139

List of Symbols and Abbreviations

8YSZ or YSZ	8% yttria stabilized zirconia ($Zr_{0.852}Y_{0.148}O_{1.926}$)
AC	Alternating current
BCY10	10% yttria-doped barium cerate ($BaCe_{0.9}Y_{0.1}O_{2.95}$)
CCY10	10% yttria-doped calcium cerate ($CaCe_{0.9}Y_{0.1}O_{2.95}$)
CeY10	10% yttria-doped ceria ($Ce_{0.9}Y_{0.1}O_{1.95}$)
CGO	20% gadolinia-doped ceria ($Ce_{0.8}Gd_{0.2}O_{1.90}$)
DCC	Doped ceria-carbonate method of solid state synthesis
E^*	Experimental activation energy for conduction
E_a	Activation energy
EDX	Energy dispersive x-ray analysis
IS	Impedance spectroscopy
MO	Mixed oxide method of solid state synthesis
PCFC	Proton conducting fuel cell
SCY10	10% yttria-doped strontium cerate ($SrCe_{0.9}Y_{0.1}O_{2.95}$)
SEM	Scanning electron microscopy
SOFC	Solid oxide fuel cell
T.F.	Goldschmidt's perovskite tolerance factor
TO	Triple oxide method of solid state synthesis
XRD	X-Ray diffraction
δ	Fraction of oxygen vacancies
λ	X-ray wavelength
ρ	Density
θ	Diffraction angle
σ	Conductivity

1.0 Introduction

In a world of ever increasing energy demands, alternative forms of energy are not only environmentally important, but also critical in replacing dwindling non-renewable energy sources. Thus, the keys to the success of a particular type of alternative energy are tied to its economic viability (or real world applicability) and its potential (and more importantly publicly perceived) environmental impact. Success will depend on many factors including but not limited to reliability, cost, efficiency, energy production and environmental impact. The complexity involved in providing a large scale real world solution is a large and expensive hurdle that cannot be avoided. For this reason, scalable energy solutions that maximize the potential number of uses and applications are preferred by the author.

Solid oxide fuel cells (SOFCs) are the most efficient technology yet invented for the conversion of chemical fuels into electricity and have shown great potential in different uses at various power levels [1]. At the core of these SOFCs are solid oxide electrolytes that facilitate ionic transport. The solid oxide electrolyte, with the addition of a porous anode and cathode, and a dense electrical interconnect, allow electricity to be produced from a fuel (anode side) and an oxidant (cathode side) [1]. The fuel and the oxidant react in the presence of the electrolyte as electrons are routed through an external circuit [1]. Generally, SOFCs operate at relatively high temperatures (700-1000°C) because of insufficient ionic conductivity in the electrolyte at lower temperatures [1]. These high operational temperatures produce some advantages as well as some disadvantages. The most intriguing advantage is the possibility of internal reforming of practical hydrocarbon fuels (such as methane), which eliminates the need for an expensive external fuel reformer that is required in low temperature fuel cells [1]. On the other hand, the high operating temperatures require the use of

specialized and expensive materials [1]. A lower operating temperature would potentially expand the number of materials available and could lower the cost substantially. A possible way to reduce this temperature is the use of a proton conducting solid as an electrolyte. Fuel flexibility would be maintained as proton conducting electrolytes have shown to be effective in reforming methane [2] as well as in fuel cells running in wet, hydrogen and/or ammonia containing atmospheres [3–6]. Since the proton is the smallest positive ion, a sufficient protonic conductivity may be able to be obtained in certain materials at lower temperatures [1]. Proton conducting electrolytes have the additional advantage in that when hydrogen is used in a proton conducting fuel cell, water is condensed on the cathode side and, therefore, does not contaminate the fuel stream on the anode side. Considerable research has been directed towards proton conducting solids and the potential of using proton conducting electrolytes [7–11] resulting in the possibility of what are called intermediate temperature solid oxide fuel cells (ITSOFC) or proton conducting fuel cells (PCFC). These fuel cells are targeted to operate in the intermediate temperature (IT) range of approximately 400-800°C [12].

As electrolyte materials for PCFCs, perovskite-type oxides such as doped barium or strontium cerates have received a lot of attention due to their high protonic conductivity at elevated temperatures in hydrogen containing atmospheres [13–15]. Similarly, doped calcium and strontium zirconates also show protonic conduction, although not as high as the aforementioned cerates [1,16]. They do, however, exhibit far superior chemical stability. For example, barium and strontium cerates readily decompose in carbon dioxide containing atmospheres, whereas the corresponding zirconates do not [12,17]. The combination of the high conductivities of barium cerates with the stability of barium zirconates has been discussed and studied, and it is generally found that increased Zr content leads to higher stabilities, but lower conductivities [12,18–22]. In his excellent

review of proton conduction in oxides [11], Kreuer discusses how the addition of barium cerate has some positive effects on the properties of yttrium-doped barium zirconate proton conductors including a slight increase in bulk conductivities at low barium cerate contents, lower sintering temperatures and lower grain boundary impedance. At higher contents of barium cerate, the conductivity decreases as yttrium is not the ideal dopant for barium cerate based proton conductors (gadolinium shows some of the highest conductivities) [11]. This is based, in part, on how well the ionic radii of the dopants match within the perovskite lattice which can be described via Goldschmidt's tolerance factor [23–25]. It was found that dopant selection has a significant effect on conductivity [20,26] as well as on stability [20].

Producing thin and dense electrolyte membranes poses another challenge. Many different methods of membrane synthesis have been reported in the literature including methods involving layer screen printing [27–29], in-situ spray printing [30], spin coating [31] and vacuum slip casting. In terms of cost, screen printing has a clear advantage in both laboratory and industrial applications and is thus of great interest.

This work focuses on material selection and preparation of thin and dense proton conducting electrolyte membranes via screen printing for potential use in proton conducting fuel cells. A solid state synthesis method has been used to investigate the influence of a matrix of materials (specifically the partial or total replacement of A- and B-site cations in the $A^{2+}B^{4+}O_3$ perovskite structure) on the properties and production of proton conducting perovskite-based solids. In addition, the potential of the screen printing process described by Meulenberg et al. [32] as a method for preparing a variety of different membrane layer compositions on different substrates has been investigated.

2.0 Background

Proton conducting materials can be applied, in theory, to many devices including hydrogen sensors and energy conversion devices as well as in chemical synthesis and the separation of hydrogen. The proton conducting solid in these devices functions as the electrolyte in electrochemical cells [16].

2.1 Proton Conducting Fuel Cells (PCFC)

The high operational temperatures of conventional SOFCs, such as those based on oxygen ion conducting YSZ, allow for low ohmic losses, low electrode overpotentials and the use of multiple types of fuel. These high temperatures, however, limit the number of materials that can be used to construct SOFCs as they often lead to fast degradation kinetics, long start up times and the need for sufficient insulation [15,33]. Proton conducting fuel cells differ from the traditional solid oxide fuel cells in that the electrolyte membrane transports protons instead of oxygen ions. They also operate at lower temperatures, which help to alleviate problems caused by the high operational temperatures of traditional solid oxide fuel cells. A simple schematic of a PCFC is shown in Figure 1. Starting with the anode side of the cell, hydrogen is oxidized to H^+ and then is conducted through the electrolyte until finally combining with oxygen to produce water at the cathode. The electrons from this reaction are routed through an external circuit and thus electricity is produced. The H^+ ions must move through the electrolyte in order for any electricity to be produced and, therefore, the ionic conductivity of the electrolyte is an extremely important factor in the performance of the fuel cell. Ideally, the protonic conduction through the electrolyte needs to be high enough for adequate performance of the cell, while still operating at a low temperature. The most studied electrolyte materials are of the perovskite type, especially rare-earth doped barium cerates and zirconates.

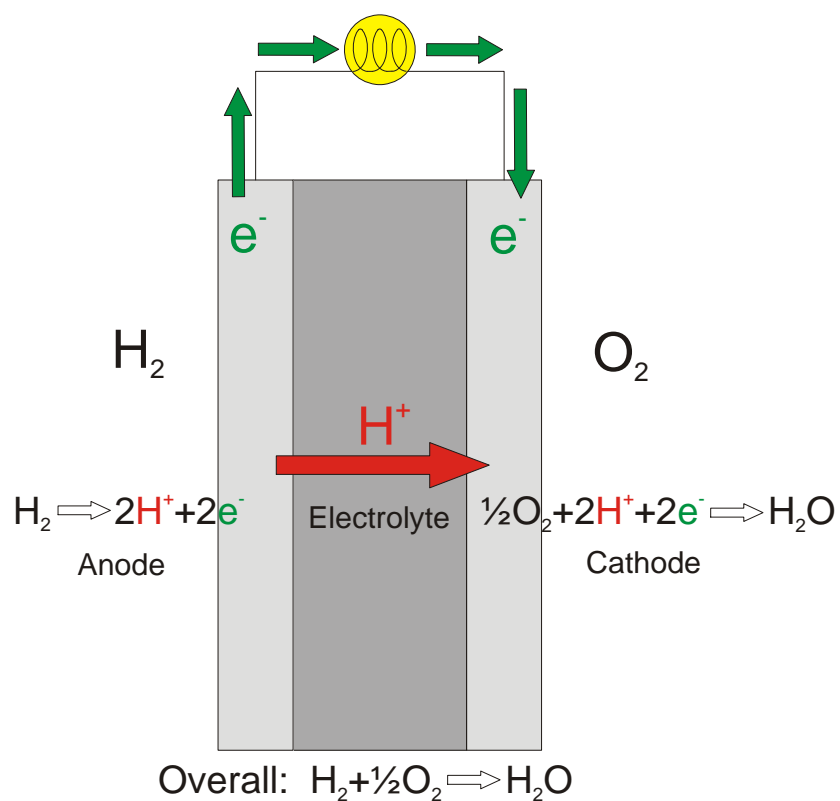


Figure 1: Schematic of a proton conducting fuel cell

2.2 PCFC Electrolyte Materials

The first materials reported to have almost pure high proton conductivity were those of the perovskite crystallographic structure type based on SrCeO_3 and BaCeO_3 [11,13,34]. Oxides of this structure remain among the best proton conductors known and are still heavily studied for this application.

Proton conducting perovskite based oxides have the general form of $\text{AB}_{1-x}\text{M}_x\text{O}_{3-y}$ in which a lower valence metal ion (M) is substituted into the lattice position of the B atom and were first described by Iwahara et al. [13]. This substitution results in the formation of positively charged oxygen ion vacancies which are compensated M^{3+} ions on B^{4+} sites which have negative effective charges. The

oxygen vacancies allow for the formation of protonic defects which are essential for protonic conduction [35–37]. This requirement for oxygen vacancies is demonstrated by undoped oxides such as SrCeO_3 which do not exhibit protonic conduction [23].

The B-site materials most studied are Ce and Zr, where the cerate based perovskites show higher conductivities, but the zirconates show better stabilities [19,38]. As potential M-site metals, yttrium and gadolinium have been studied extensively [7,34,39–41]. Additional studies have focused on other possible dopants such as europium, scandium, samarium and terbium [10,29,42–47]. To produce a compound with a perovskite structure, the A-site cation must be larger than the B-site cation. The most studied materials for the A-site are Ba, Sr and Ca.

2.3 Synthesis Methods

2.3.1 Powder Synthesis

Various methods have been used and researched for the synthesis of monophasic perovskite powders.

2.3.1.1 Solid State Synthesis

The most common method of solid state synthesis is the mixed oxide method beginning with the original descriptions by Iwahara et al. [13,34] of protonic conduction in perovskite-type oxides based on SrCeO_3 and BaCeO_3 . In this method, the component oxides (ceria, alkaline earth carbonate, dopant aliovalent oxide) are mixed and then calcined to form the perovskite powder. This powder is then pressed and sintered (usually into pellets or bars) in order to test for a variety of properties including conductivity. Due to the relative simplicity of this process, it is ideally suited for testing various perovskite

compositions before they are fabricated into membranes for use in solid oxide fuel cells.

2.3.1.2 Oxalate Coprecipitation

The powders can also be prepared via a solution based approach [48,49]. In the work done by Chen et al. [49], $\text{Ba}(\text{NO}_3)_2$, $\text{Ce}(\text{NO}_3)_3 \cdot 6\text{H}_2\text{O}$ and $\text{Nd}(\text{NO}_3)_3 \cdot 6\text{H}_2\text{O}$, in stoichiometric ratios, were dissolved and heated to the boiling point in deionized water. The mixture was stirred vigorously while hot ammonium oxalate was added resulting in instantaneous coprecipitation. This precipitate was then allowed to crystallize at room temperature, and filtered and dried in an oven at 100°C for 24 h. This method is more complex than solid state synthesis, but could potentially lead to lower sintering temperatures [50]. If solid state synthesis cannot be used or does not produce acceptable results, this method would be an option.

2.3.1.3 Spray Pyrolysis of Nitrate Salt Solutions

Perovskite powders have been synthesized using a spray pyrolysis of nitrate salt solutions method by Dahl et al. [14]. Using this method, powders of SrCeO_3 and $\text{SrCe}_{0.95}\text{Yb}_{0.05}\text{O}_{3-\delta}$ were synthesized from aqueous solutions of cerium nitrate ($\text{Ce}(\text{NO}_3)_2 \cdot x\text{H}_2\text{O}$) and ytterbium nitrate ($\text{Yb}(\text{NO}_3)_3 \cdot 5\text{H}_2\text{O}$) that were mixed with dried strontium nitrate ($\text{Sr}(\text{NO}_3)_2$). The mixed solutions were then atomized in a furnace and calcined to produce pure powders. The method proved to be a good method for the synthesis of fine strontium cerate powders although the powders did have to be calcined afterwards to remove secondary phases. It does, however, result in spherical shaped particles that increase the surface energy which leads to lower calcination/synthesis temperatures.

2.3.2 Supported Membrane Synthesis

A variety of methods have been reported for the production of thin and dense proton conducting membranes and three of particular interest are described below.

2.3.2.1 Layer Screen Printing

Proton conducting membranes can be synthesized through a solid state reaction of screen-printed layers over top of porous substrates. In the process described by Meulenbergh et al. [32], macroporous substrates of either a graded porosity NiO-8YSZ cermet or a 20% gadolinia-doped ceria (CGO) were used as porous supports (substrates). Doped ceria with the fluorite structure (in this case 20% gadolinia doped ceria) is then screen printed or vacuum slip cast onto the top surface of the support. The sample is then dried and calcined before a stoichiometric amount of carbonate (BaCO_3) is screen printed over top. The support complete with the two screen printed layers was then sintered in order to effect the solid state reaction and synthesize the proton conducting perovskite layer. A schematic of the process for the synthesis of a thin and dense layer of $\text{BaCe}_{0.8}\text{Gd}_{0.2}\text{O}_{3-\delta}$ is shown in Figure 2.

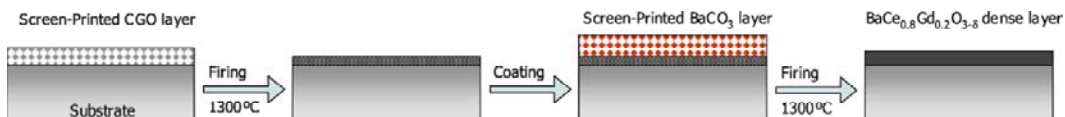


Figure 2: Schematic diagram of the procedure for producing thin-film $\text{BaCe}_{0.8}\text{Gd}_{0.2}\text{O}_{3-\delta}$ membranes [32]

2.3.2.2 In Situ Spray Printed Method

A novel method for membrane synthesis was presented by Bi et al. [46]. In this method, a homogenized mixture of BaCO_3 , CeO_2 and Sm_2O_3 is sprayed directly onto the anode substrate. After sintering at 1400° for 5 h, a very dense electrolyte membrane of about $10\ \mu\text{m}$ is formed. This method is interesting as

no calcination is required before the actual layer synthesis. A very well homogenized mixture of the starting materials is critical to achieve a uniform and dense membrane.

2.3.2.3 Sol-Gel

A sol-gel method was used by Eschenbaum et al. [51] to produce Yb-doped SrZrO_3 thin films at low sintering temperatures. In this method, precursor solutions were prepared from strontium acetate-hemihydrate, ytterbium acetate-tetrahydrate and zirconium *n*-propoxide with glacial acetic acid and acetyl acetone. Using dip-coating, thin films were prepared from the precursor solutions on silicon, fused silica and steel substrates. The films were dried at 130°C for 10 minutes to remove any residual solvents before being calcined at 600°C . Successive dip-coatings onto previously calcined layers were used to obtain higher film thicknesses before being finally sintered at $700\text{-}1000^\circ\text{C}$. The authors found that sintering temperatures of 700°C were sufficient for quantitative formation of crystalline SrZrO_3 films. This method is very fascinating due to the very low sintering temperatures required. Further work would have to be done with this method to determine if gas tight thin layers could be formed to be used as part of a proton conducting fuel cell.

3.0 Theory

3.1 Ceramic Structures of Interest

In the chosen perovskite-type proton conducting solid synthesis, both the fluorite and perovskite structures are important.

3.1.1 Fluorite Structure

The fluorite structure derives its name from the mineral fluorite (CaF_2) and oxides of this structure have been traditionally used as oxygen ion conductors [52]. Fluorite oxides have the general formula of AO_2 where A is a large tetravalent cation. Figure 3 shows the fluorite structure that consists of a cubic oxygen lattice with cations occupying alternating body centers [52].

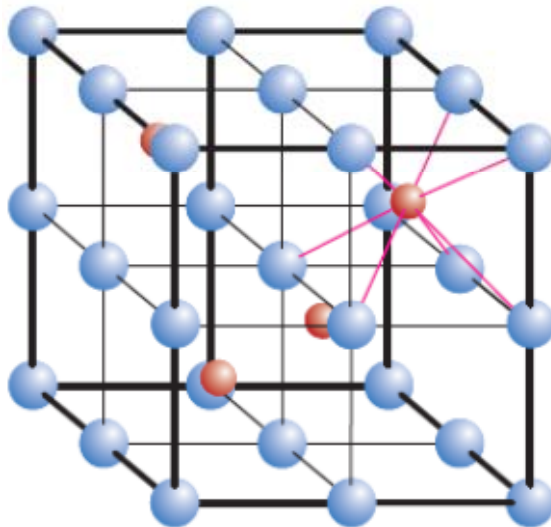


Figure 3: The fluorite (AO_2) oxide structure. The red spheres represent the A cation sites and the blue spheres the oxygen sites [52]

If the cation is not large enough, the fluorite structure is not able to be formed [52]. For example, zirconia does not exist in the fluorite structure at room temperature unless doped with a large cation such as yttrium [52]. This substitution or doping can also be used to introduce oxygen vacancies into the

fluorite structure. Using the Kröger-Vink notation for defect chemistry, the oxygen vacancy reaction for dopant oxides with cations of lower valence (acceptor type of doping) can be shown as:



where B''_A is the bivalent B-ion at A-position with an effective negative charge (2-), B'_A is the trivalent B-ion at A-position negatively charged (1-), O_O^x is oxygen in the crystal lattice with neutral charge and $V_O^{\bullet\bullet}$ is an oxygen vacancy with an effective positive charge (2+).

3.1.2 Perovskite Structure

The word perovskite is both the name of the mineral $CaTiO_3$ and the structure associated with it which sometimes leads to a certain amount of confusion regarding the nomenclature [24]. Perovskites have the general formula of ABX_3 consisting of two cations (A and B site) with an anion that bonds them together [24]. Figure 4 [23] shows a schematic of the perovskite structure. It consists of a cubic structure with the A-site cation occupying the body centre, the 8 B-site cations at the corners, and the 12 oxygen ions located at the centre of the cube edges [23]. Thus, each B-site is octahedrally coordinated by 6 oxygen ions.

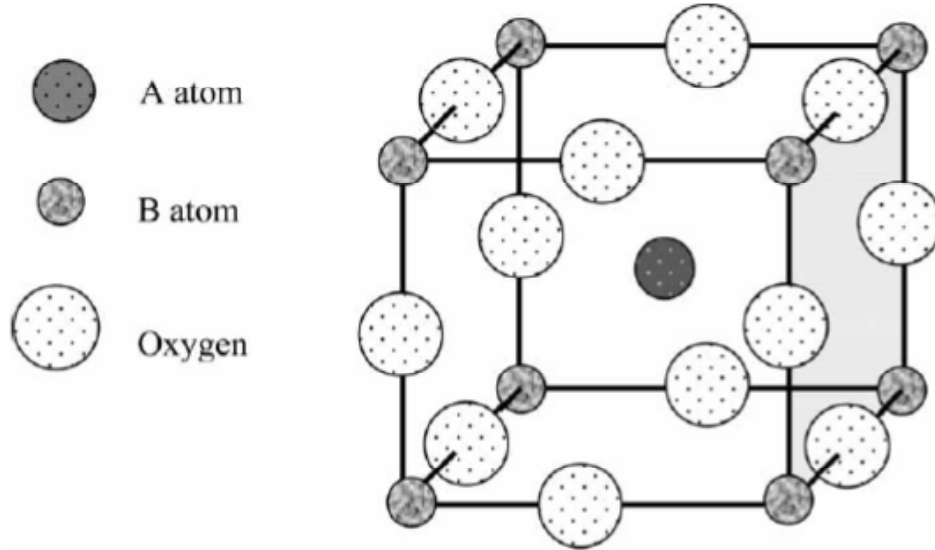


Figure 4: Schematic of the perovskite structure with oxygen as the anion [23]

The A-site cation is generally larger than the B-site cation and a tolerance factor is used in determining the strain of the cubic lattice [23]. The tolerance factor for determining the deviation from the cubic lattice is defined as [23]:

$$T.F. = \frac{r_A + r_O}{\sqrt{2}(r_B + r_O)} \quad (3)$$

where r_A , r_B and r_O are the radii of the A-site cation, B-site cation and oxygen anion, respectively.

As first described by Goldschmidt [24,25], the perovskite structure is stable in the range of $0.80 < T.F. < 1.00$ where the ideal perovskite structure has a tolerance factor of ~ 1.00 . For example, the optimal tolerance factor for oxygen ion conduction in $A^{III}B^{III}O_3$ perovskites was found to be 0.96 [53]. Furthermore, by using large cations, larger free volumes are obtained which aid in ionic conductivity [53].

Oxygen vacancies are generally incorporated into the perovskite structure via the following reaction:



where the trivalent metal oxide (M_2O_3) is doped onto the tetravalent B-site of the perovskite (ABO_3) lattice, which results in two metal ions on B-sites with negative effective charges and one oxygen vacancy.

3.2 Electrical Conductivity in a Solid

Trovarelli [54] describes the total electrical conductivity in a solid (σ_t) which is defined as the sum of the conductivity contributions from each of the charge carriers present. The charge carriers can be atomic (anion or cation defects) or electronic (electrons or holes) and their contribution to the total conductivity is represented by a partial conductivity, σ_j .

$$\sigma_t = \sum_j \sigma_j \quad (5)$$

These partial conductivities can be determined using the expression:

$$\sigma_j = c_j z_j e \mu_j \quad (6)$$

where σ_j is in Siemens per cm, c_j is the carrier concentration per cm^3 , $z_j e$ is the carrier charge in Coulombs and μ_j is the carrier mobility ($\text{cm}^2/\text{V}\cdot\text{s}$). Using these partial conductivities, a transport (or transference) number can be determined which defines the fraction of the total conductivity contributed by each individual charge carrier:

$$t_n = \frac{\sigma_n}{\sum_j \sigma_j} \quad (7)$$

where t is the transport number of species n .

For mixed conductors that exhibit both electronic and ionic conductivity, the following expression applies:

$$\sigma_t = \sigma_i + \sigma_{el} = t_i \sigma_t + t_{el} \sigma_t \quad (8)$$

where $t_i + t_{el} = 1$ and $t_{el} = t_e + t_h$.

3.2.1 Ionic Conduction

Ionic conductors conduct via anion or cation defects and can be divided into three classes based on their defect concentrations: dilute point defects ($\sim 10^{18}$ defects/cm³), concentrated point defects ($\sim 10^{18-20}$ defects/cm³) and liquid-like or molten salt sublattice materials ($\sim 10^{22}$ defects/cm³). For both dilute and concentrated point defects, conductivity occurs via an ion hopping mechanism, whereas the ions in the sublattice of a molten salt sublattice material behave more like a liquid and will move along conduction pathways. In the case of protonic conduction, proton movement occurs by either lone proton migration or as proton-carried migration (for example as H₃O⁺). In both cases, the earlier subdivisions of dilute point defects, concentrated point defects and molten salt sublattice still apply [55].

In solid state chemistry, it is common for the Arrhenius relation to be used to model the temperature dependence of conduction in dielectric materials. The

Arrhenius relation is named after Svante Arrhenius (1859-1927) and has the general form:

$$r = Ae^{-E_a/kT} \quad (9)$$

where r is the reaction rate, A is the constant pre-exponential factor, T is the temperature in Kelvin, k is Boltzmann's constant (8.617×10^{-5} eV/K) and E_a is the activation energy or the minimum energy for a chemical or physical process to occur. For the modeling of conduction processes in solid state chemistry, the equation takes on a slightly different general form:

$$\sigma = \sigma_0 e^{-E^*/kT} \quad (10)$$

where σ is conductivity, σ_0 is often described as a temperature independent constant and E^* is the experimental activation energy for conduction. With σ_0 constant, a plot of the natural logarithm of conductivity against the inverse of temperature results in a slope that corresponds to the activation energy (E^*/kT). This plot is most commonly referred to as an Arrhenius plot [56].

3.2.2 Proton Chemistry and Conduction Mechanisms

Proton conduction is a special type of ionic conduction [55]. Hydrogen contains only one electron in its neutral state. Thus, the positive hydrogen ion, essentially a bare 'proton', is the only ion without an electron shell [57]. Consequently, protons strongly interact with the electron density in their surrounding environments and are usually solvated [55,57]. In metals, protons interact with the delocalized electron density in the conduction band while, in non-metallic compounds, they interact with the valence shell electron density of only one or two of their nearest neighbours [57]. The hydrogen bond has comparatively weak directional interaction as it is approximately one order of magnitude lower

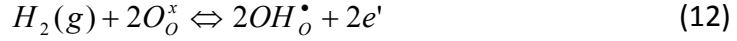
in energy than primary chemical bonds [57]. The proximity of the electronegative nearest neighbour species to one another has an effect on the type of interaction [57]. For example, protons dissolved in oxides will interact primarily with oxygen ions. If the proton interacts with a single oxygen that is well separated from other electronegative species, an O-H bond (or hydroxide ion) of less than 100 pm in length is formed which is less than the 'ionic' radius of the oxide ion [57,58]. Alternatively, if the oxygen-to-oxygen distance is very short (~240 pm), a symmetrical hydrogen bond may be formed in which the proton forms two equivalent bonds [57]. For moderate oxygen to oxygen distances (~250-280 pm), an asymmetrical hydrogen bond with directional character may be formed [57].

For the large band gap perovskites under discussion, the most important reaction that leads to protonic defect formation at moderate temperatures is the dissociative absorption of water [55]. This reaction, however, requires oxygen vacancies, V_o^{**} , to be present in the structure [55]. To create these vacancies, substitution or doping of up to 25% of the B-site cations by a lower valent cation is used [55]. The general structure of the perovskite then becomes $AB_{1-x}M_xO_3$, where M is the lower valent cation. In the case of $BaCeO_3$ and $BaZrO_3$ -type perovskites, for example, yttrium is often used as the dopant [59,60]. To form the protonic defects, water from the gas phase dissociates into a hydroxide ion that fills an oxygen vacancy and a proton that forms a hydrogen bond with a lattice oxygen [11]. Using Kröger-Vink notation, this reaction can be written as:



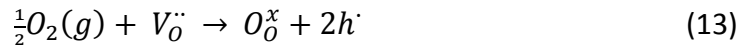
where two protonic defects (OH_o^\bullet) are formed [11]. These defects can, therefore, only diffuse through the bulk of the material if there is a counter

diffusion of oxide ion vacancies ($V_o^{\bullet\bullet}$) [11]. In hydrogen containing atmospheres, the protonic defect formation reaction can be shown as:



where, again, two protonic defects are formed [36].

In addition to oxide ion vacancies that exist at lower water vapour concentrations, electron holes (h^\bullet) are an important consideration at high oxygen activities. P-type defects or electron holes are produced according to:



where the dissolution of oxygen into an oxygen vacancy ($V_o^{\bullet\bullet}$) produces two electron holes (h^\bullet) [61]. For the large band gap perovskites discussed here, the electron hole contribution may not be important at temperatures less than 750°C [11]. At low oxygen partial pressures, loss of oxygen leads to the generation of electrons (e') and oxygen vacancies as follows:



It is apparent that a low oxygen pressure should lead to more n-type electronic conductivity [61].

It should be noted that, for these oxides, the main proton conducting mechanism involves proton transport between neighbouring OH^- and O^{2-} through the reorientation of OH^- (Grotthuss mechanism or lone proton migration) [57]. Lone proton migration involves the transport of a proton

between relatively stationary host anions through the reorientation of single species or more extended structures [57,59]. Thus, the proton is transported through reorganization of the structural pattern along its diffusion path [57]. This is often achieved through reorientation of solvent dipoles such as H₂O (shown in its three steps in Figure 5) [57].

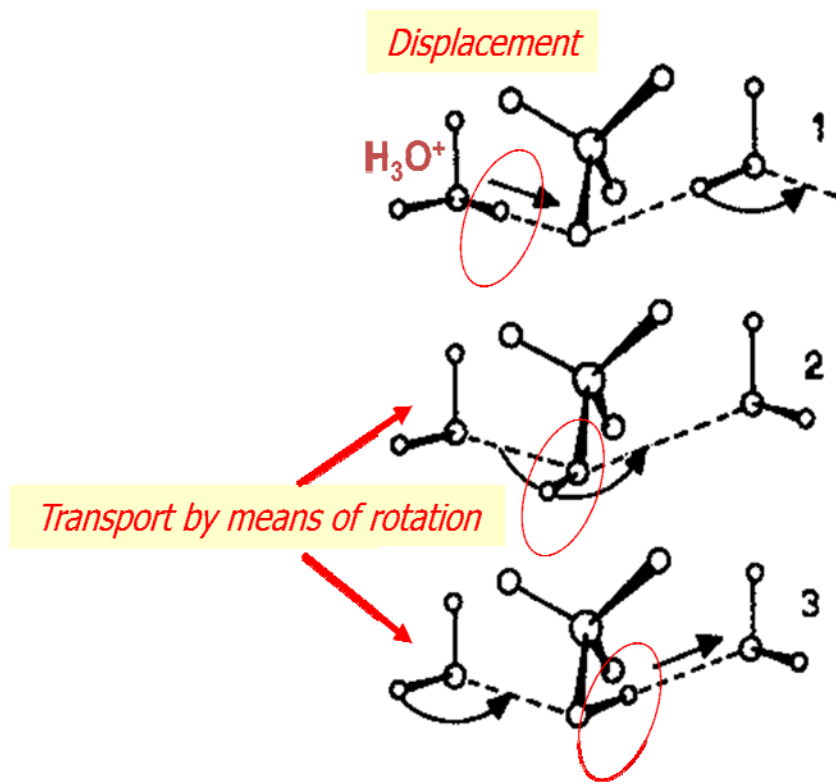


Figure 5: Proton translocation mechanism involving reorientation of H₂O [55,62]

The transport of protons in the translocation model is dependent on overcoming both the energy required for the displacement of a proton along a hydrogen bond (the transfer energy barrier, E_{bar}) and the transport of the a proton from this hydrogen bond to the next (the bond breaking energy, E_{bond}) [55]. If this model is refined to account for the reorientation of a molecule like H₂O, E_{bond} is replaced by the energy barrier to reorientation, E_{reor} [55]. All of these energy barriers are thus dependent on the host ion-to-host ion distance as can be seen when energies are plotted versus oxygen-to-oxygen distance (or the

displacement of H^+ along a hydrogen bond) as shown in Figure 6a and in the schematic representations of the energy barriers for both short and long oxygen-to-oxygen distances shown in Figure 6b [55]. If it is assumed that maximum values for these energy barriers are less than the activation energy for proton conduction, E_{σ} , of ~ 0.9 eV or ~ 83.7 kcal/mol, the range of distances A-B should permit proton conduction [55]. If the lower energy barrier for reorientation, E_{reor} , is used instead of the bond breaking energy, E_{bond} , the range of distances A-C should permit proton conduction [55]. Thus, the optimum value of d_{o-o} for translocation corresponds to the point at which the $E_{barrier}$ and E_{reor} curves cross [55].

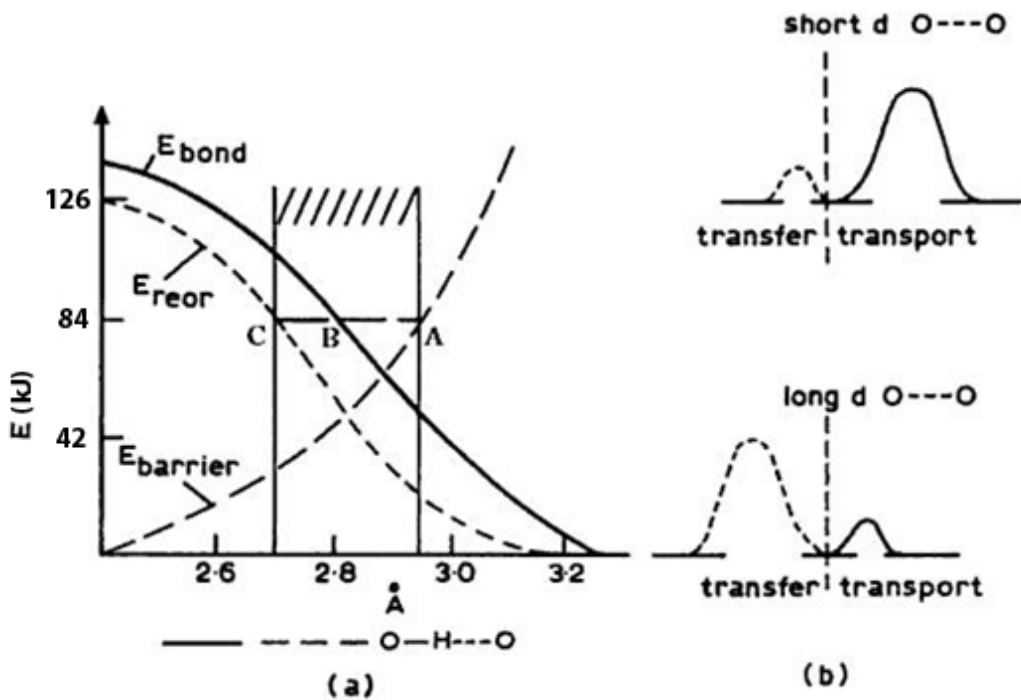


Figure 6: Energy profile for H^+ transport in the translocation model [55]

In the ideal cubic perovskite structure, there is only one type of oxygen site and the hydroxide ions (protonic defects) formed in the dissociation reaction of water reside on structurally identical lattice positions [11]. However, a distortion

from this ideal structure could result in a differentiation among oxygen sites and thus an increase in the mobility activation enthalpy for protonic defects [11]. In comparing the structures of Y-doped SrCeO_3 and Y-doped BaCeO_3 , the larger orthorhombic distortion of Y-doped SrCeO_3 has a large effect on the arrangement of lattice oxygen [11]. The result of distortion is the degeneration of the oxygen site into two different sites with probabilities of 1/3 (O1) and 2/3 (O2) [11]. These oxygen sites have different electron densities (basicities) due to different chemical interactions with the cations (especially the A-site strontium) and thus different binding energies for the proton [11]. As can be seen in Figure 7, the O1 oxygen is the most basic in SrCeO_3 , whereas the O2 oxygen is the most basic in BaCeO_3 [11]. If it is assumed that most of the time protons are associated with these sites, long-range proton transport in BaCeO_3 may occur through the more frequent O2 sites, whereas in SrCeO_3 , long-range proton transport has to occur between the chemically different O1 and O2 sites [11]. This is one of the main reasons thought to cause the higher activation enthalpy and lower proton conductivity in SrCeO_3 compared with BaCeO_3 [11].

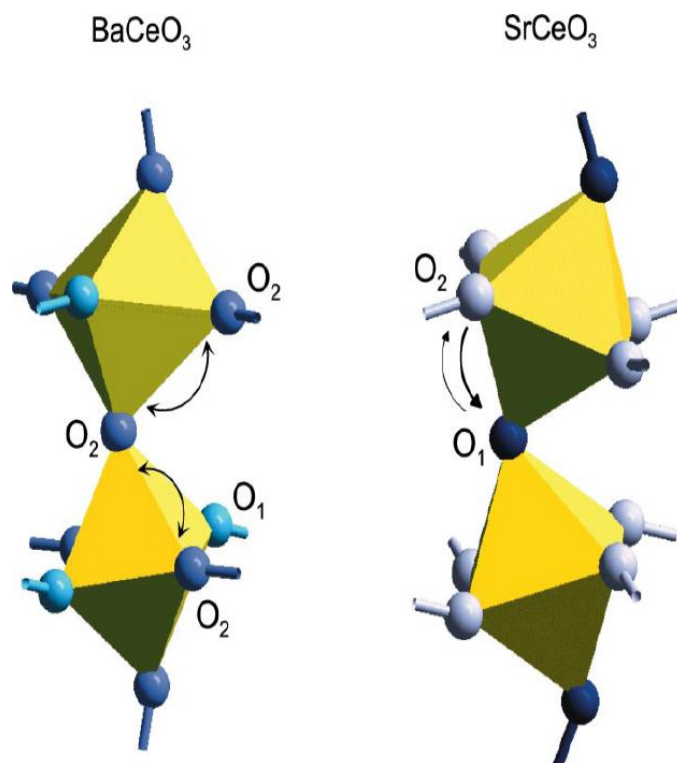


Figure 7: Effect of the orthorhombic distortion of BaCeO₃ and SrCeO₃ on the basicity of O1 and O2 (basicity indicated by the darkness of the oxygens). The arrows indicate the predominant proton transfers [11].

In the other main proposed method of conduction (the proton-carrying mechanism or vehicle mechanism), the proton is aided by the translational movement of a bigger species (vehicles) such as H₂O or NH₃. The proton migrates in one direction as H₃O⁺ or NH₄⁺, while the neutral species (H₂O or NH₃) migrate in the opposite direction resulting in a net transport of protons through the solid [55,57].

3.3 Characterization Methods

3.3.1 Electrochemical Measurements

Impedance spectroscopy (IS) can be used to characterize many of the electrical properties of materials as well as their interfaces using the frequency response of an electrode-material system to an applied alternating current (AC) [63]. The impedance of a system is measured over a range of frequencies allowing for the

separation of different processes that have different time constants [64]. An excellent working background for the practical application of impedance spectroscopy can be found in the first chapter of the Macdonald and Barsoukov edited book, "Impedance Spectroscopy: Theory, Experiment, and Application" [63]. More complex electrochemical descriptions are found later in the book as well as in the paper by Archer and Armstrong [65] which specifically discusses how AC impedance methods can be applied to solid electrolytes. Excellent specific examples of the application of AC impedance methods to proton conductivity experiments can be found in the papers by Amsif et al. [26] and Haile et al. [66]. The following is a brief overview of the method and how it applies to the author's research.

Characterization of the electrochemical behavior of electrolyte and/or electrode materials is generally done by applying identical electrodes to the faces of circular cylinders or pellets. Under a controlled atmosphere, an electrical stimulus is applied (a known voltage or current) and the response of the material is observed. It is almost always assumed that the properties of the electrode-material system do not vary with time and thus IS can be used to determine the effect on these properties of changing controllable variables such as temperature, atmosphere (i.e., oxygen partial pressure or moisture content) and applied static current bias or voltage. Of the three different types of electrical stimuli used for IS, the most often used and standard one is to measure the impedance by applying a voltage or current at a single frequency. Measuring and analyzing the phase shift and amplitude (real and imaginary parts) of the resulting current at that frequency allows for the response of the material to be investigated [63].

Many commercial instruments are available that can measure the impedance as a function of frequency and are easily connected to laboratory computers. For

example, the ProboStat™ cell by Norwegian Electro Ceramics AS can be used in combination with various measurement systems to provide a wide array of electrochemical data, and has been used by the author specifically for temperature and atmosphere dependent conductivity measurements of proton conducting solid ceramic electrolytes.

3.3.2 X-Ray Diffraction (XRD)

X-ray diffraction is a non-destructive analytical method in which information about a sample is acquired by bombarding it with x-rays and observing the scattered intensity of these beams. The constructive and destructive interference of the scattered beams produce a pattern that can be analyzed. The interference is fully constructive for every phase shift of 2π and Bragg's Law describes this by use of the following equation:

$$n\lambda = 2d \cdot \sin \theta \quad (15)$$

where n is an integer multiple of the wavelength, λ is the wavelength of the x-rays, d is the spacing between the planes in the atomic crystal lattice and θ is the angle between the incident x-rays and the scattering planes (the diffraction angle).

3.3.3 Differential Thermal Analysis/Thermogravimetry (DTA/TG)

Differential thermal analysis is a thermoanalytic technique in which a sample and an inert reference material are subjected to identical thermal cycles and any differences in temperature between the two are recorded. This is based on the principle that during endothermic or exothermic transitions in the sample, a different temperature will be recorded with respect to the reference material. This difference can be plotted versus temperature or time and used to give

information about the transformations that have occurred such as reactions, phase transformations, crystallization and melting.

Thermogravimetry measures the weight change of a sample with respect to a programmed temperature change. This makes it possible to observe mass loss resulting from factors such as chemical decomposition, sorbed water evolution, and the amount of organic and inorganic material present in a sample.

3.3.4 Particle Size Analysis

Laser particle size analysis uses the principle of light scattering in which a laser shines through a powder sample suspended in a solvent and into a detector. A basic overview of a typical process can be found on the Fritsch GmbH website [67] and is briefly summarized here. The sample scatters the light and this intensity distribution causes a series of concentric rings of laser light to form, which are picked up by the detector. The spacing of these rings corresponds to the particle size. There are two main theories used for the analysis of the light scattering data: The Fraunhofer theory and the Mie theory. The Fraunhofer theory is generally used for particle sizes in the range of 1-200 μm [68] and has a major benefit in that the optical properties of the material being studied do not need to be known. For smaller particle sizes, the Mie theory is used, but the refraction index and absorption index of the examined material must be known.

3.3.5 Scanning Electron Microscopy/Energy Dispersive X-Ray Spectroscopy

A scanning electron microscope uses a beam of electrons that scans the surface using a raster pattern. When an electron hits and is absorbed by an atom very near to the surface, the atom is ionized briefly and then re-emits this electron as a 'secondary electron'. These secondary electrons are detected and are the primary method for image production. Back scattered electrons are electrons that are not absorbed by atoms, but instead are elastically scattered back to the

detector. The intensity of the back scattered electrons detected are very closely related to the atomic number and, therefore, one can obtain some data about the composition of the sample surface. Characteristic x-rays are produced by the interaction of the electrons with the sample meaning information about the composition of the material can be obtained (EDX analysis).

3.3.6 Laser Surface Scanning

The laser surface scanner scans the surface of a sample in a raster pattern and relies on the information provided by the reflected light. Using this gathered information, a three dimensional image can be produced showing the samples surface topography.

4.0 Experimental

For reference, the commercially obtained reactant powders are listed in Table 1 and the various solid state heat treatments used are shown in Table 2.

Table 1: Commercially obtained chemicals (powders)

Powder	Particle Size	Purity	Supplier	Product Code
CeO ₂	nanopowder, <25 nm (BET)	-	Sigma-Aldrich	544841-25G
ZrO ₂	nanopowder, <100 nm (BET)	-	Sigma-Aldrich	544760-25G
Ce _{0.8} Gd _{0.20} O _{1.90}	nanopowder, <100 nm (BET)	-	Sigma-Aldrich	572357-25G
Ce _{0.8} Y _{0.15} O _{1.925}	nanopowder	-	Sigma-Aldrich	572381-25G
Ce _{0.8} Sm _{0.15} O _{1.925}	nanopowder	-	Sigma-Aldrich	572365-25G
Eu ₂ O ₃	nanopowder, <150 nm (BET)	99.5%	Sigma-Aldrich	634298-25G
Gd ₂ O ₃	nanopowder, <100 nm (BET)	99.8%*	Sigma-Aldrich	637335-10G
Sc ₂ O ₃	-	99.999%*	Sigma-Aldrich	294020-5G
Sm ₂ O ₃	nanopowder, <100 nm (BET)	99.9+%	Sigma-Aldrich	637319-10G
Tb ₂ O ₃	-	99.99%	Sigma-Aldrich	590509-10G
Y ₂ O ₃	nanopowder, <50 nm (BET)	-	Sigma-Aldrich	544892-25G
Yb ₂ O ₃	nanopowder, <100 nm (BET)	99.7+%	Sigma-Aldrich	637300-10G
Nd ₂ O ₃	nanopowder, <100 nm (BET)	99.90%	Sigma-Aldrich	634611-5G
BaCO ₃	d ₅₀ =24.49 μm , d ₉₀ =43.37 μm**	99.98%*	Sigma-Aldrich	329439-100G
CaCO ₃	d ₅₀ =28.26 μm , d ₉₀ =43.38 μm**	99.0+%*	Sigma-Aldrich	C4830-500G
SrCO ₃	d ₅₀ =1.25 μm , d ₉₀ =3.36 μm**	99.9%*	Sigma-Aldrich	472018-500G
Glyceryl tristearate	-	-	Sigma-Aldrich	69498-250G-F
Stearic acid	-	97.0%	Acros Organics	AC17449-0010

*Trace metals basis

**Measured particle sizes

Table 2: Heat treatments

Heat Treatment	Atm.	Ramp Rate to Dwell 1 (K/min)	Dwell 1		Ramp Rate to Dwell 2 (K/min)	Dwell 2		Ramp Rate Down (K/min)
			Temp. (°C)	Time (h)		Temp. (°C)	Time (h)	
Cerate1	Air	3	800	3	3	1250	6	3
Perovskite1	Air	3	1400	8	-	-	-	3
Perovskite2	Air	3	1400	16	-	-	-	3
Perovskite3	Air	3	1200	8	-	-	-	3
Perovskite4	Air	3	1300	8	-	-	-	3
Perovskite5	Air	5	1400	10	-	-	-	5
Perovskite6	Air	5	1450	10	-	-	-	5
Perovskite7	Air	5	1500	10	-	-	-	5
Electrodes1	Air	8.2	1000	2	1.7	1200	2	9.8
Sinter1	Air	1	1550	10	-	-	-	1
Sinter2	Air	1	500	1	5	1600	10	5
Sinter3	Air	1	500	1	5	1650	10	5

4.1 Powder Synthesis

The powders were all prepared using solid state synthesis methods. The commercially pure reactants can be found in Table 1.

4.1.1 Doped Ceria Synthesis

A solid state synthesis method was used for production of the doped ceria powders. Nano-sized powders of very pure ceria and of the dopant oxides were obtained commercially from Sigma Aldrich. Stoichiometric amounts of these powders were then magnetically stirred and ultrasonically mixed in ethanol. The powders were then dried at 80°C in a vented drying oven and then ground using a mortar and pestle. The powders were then calcined according to heat treatment Cerate1 in Table 2.

4.1.2 Doped Cerate Perovskite Synthesis

Three different methods were used in attempts to produce monophasic perovskite powders. The barium, strontium and calcium carbonates used were

ball milled for 72 h in ethanol with zirconia milling balls, dried, and then crushed by hand with a mortar and pestle before being used for synthesis.

4.1.2.1 **Doped Ceria-Carbonate Method (DCC)**

The starting materials for this process were the pre-doped ceria powders and BaCO₃, CaCO₃ or SrCO₃. Stoichiometric ratios of these powders were mixed and ball milled in ethanol before being dried at 80°C in a vented oven. These powders were heat treated in zirconia crucibles for 8 or 16 h at 1400°C (heat treatments Perovskite1 and Perovskite2 in Table 2).

4.1.2.2 **Mixed Oxide Method (MO)**

Stoichiometric amounts of ceria, dopant oxide, and carbonate were weighed for various compositions. The powders were magnetically stirred, ultrasonically mixed, and ball milled with zirconia milling balls in ethanol. After evaporation of ethanol in a vented drying oven at 80°C, the powders were calcined in zirconia crucibles for 8-16 h between 1200-1400°C (heat treatments Perovskite1, Perovskite2 and Perovskite3 in Table 2).

4.1.2.3 **Triple Oxide Method (TO)**

In this method, barium, strontium and calcium oxides (BaO, SrO and CaO) are used instead of the carbonates, but all other steps are the same as the mixed oxide method. Care was taken to weigh the appropriate amounts of the oxides as soon as possible after removal from their commercially sealed containers to avoid reaction with H₂O_(g) and CO_{2(g)} in air.

4.1.3 **Doped Barium Cerate-Zirconate Synthesis**

The method used for synthesizing the doped cerate-zirconate powders was very similar to the mixed oxide method used for doped cerate synthesis. Stoichiometric amounts of ceria, zirconia, barium carbonate and rare earth dopant oxides (M₂O₃) were measured with the aim of producing a final

compounds with the composition of $\text{Ce}_{0.50}\text{Zr}_{0.40}\text{M}_{0.10}\text{O}_{2.95}$. The rare earth oxides tested as dopants were Y_2O_3 , Gd_2O_3 , Yb_2O_3 , Eu_2O_3 and Nd_2O_3 . The powders were mixed using zirconia milling balls in ethanol in either a simple rolling ball mill for 24 h or a RETSCH PM 100 planetary mill at 500 rpm for 1 h.

The mixed powders were then calcined at 1400-1500°C for 10 h depending on the dopant used. A summary of the furnace conditions for synthesis of the five compositions can be seen in Table 3.

Table 3: Summary of heat treatments used for barium cerate-zirconate samples

Sample Composition	Heat Treatment	Atmosphere	Ramp Rate (K/min)	Dwell 1	
				Temp. (°C)	Time (h)
$\text{BaCe}_{0.50}\text{Zr}_{0.40}\text{Y}_{0.10}\text{O}_{2.95}$	Perovskite5	Air	5	1400	10
$\text{BaCe}_{0.50}\text{Zr}_{0.40}\text{Gd}_{0.10}\text{O}_{2.95}$	Perovskite5	Air	5	1400	10
$\text{BaCe}_{0.50}\text{Zr}_{0.40}\text{Eu}_{0.10}\text{O}_{2.95}$	Perovskite6	Air	5	1450	10
$\text{BaCe}_{0.50}\text{Zr}_{0.40}\text{Nd}_{0.10}\text{O}_{2.95}$	Perovskite6	Air	5	1450	10
$\text{BaCe}_{0.50}\text{Zr}_{0.40}\text{Yb}_{0.10}\text{O}_{2.95}$	Perovskite7	Air	5	1500	10

After the heat treatments, the particle sizes of the powders were reduced by planetary ball milling. To accomplish this, the powders were placed into 120 mL polypropylene jars (Fisher Scientific) with 5 mm zirconia milling balls and ethanol. Teflon tape was used to help with the sealing of the lids of the jars. An approximate 2:1 weight ratio of powder to milling balls was used. Enough ethanol was added to just cover the powder and milling balls which resulted in a ratio of approximately 1.4 mL of ethanol per gram of powder. The jars were then put into a custom machined steel container and then placed into a RETSCH PM 100 planetary mill for 24 h at 500 rpm.

4.1.4 Powder Characterization

Powder x-ray diffraction measurements were performed using a SiemensD5000 diffractometer with CuK_α ($\lambda = 1.54\text{\AA}$) radiation with a diffraction angle (θ) range

of 20° to 80°. XRD data were analyzed using JADE software by MDI. DTA/TG was performed using Netzsch STA 409C equipment under air flow with a 5 K/min heating ramp from room temperature to 1400°C. Alumina crucibles were used for both DTA and TG. Particle size analysis was carried out using a Fritsch laser particle sizer Analysette 22 with powder samples suspended in ethanol.

4.2 Sintered Bar and Pellet Synthesis

In preparation for conductivity tests, bars and pellets of the monophasic perovskite powders were pressed and then sintered with the goal of attaining near theoretical density.

4.2.1 Bars

Uniaxial pressure was applied to cold press the calcined powders into bars (5 mm x 20 mm) of approximately 3 mm in thickness. Two pressure stages were used when pressing the bars: 25-26 MPa was applied for 1 min, which was followed by the application of 80-85 MPa for 2 min. The green bars were sintered in air at 1550°C for 10 h with a 1 K/min ramp rate (heat treatment Sinter1).

4.2.2 Pellets

Sintered pellets of various sizes were made by cold pressing the powders in cylindrical molds using a uniaxial hand press (Carver Laboratory Press – Model C).

After planetary ball milling, the doped barium cerate-zirconate powders were mixed with 2 wt% of each of a dispersant (menhaden fish oil, Tape Casting Warehouse, Yardley, PA), a binder (polyvinyl butyral (PVB), Tape Casting Warehouse, Yardley, PA) and a plasticizer (butyl benzyl phthalate, Tape Casting Warehouse, Yardley, PA). To ensure good mixing, solutions of the binder and

plasticizer were made and then mixed with the powders using zirconia milling balls and ethanol in a planetary ball mill. The first solution was made by mixing 10 wt% menhaden fish oil into an azeotrope of ethanol and toluene. The second solution was made by mixing 10 wt% of each of polyvinyl butyral and butyl benzyl phthalate into the same azeotrope of ethanol and toluene. The suspensions were dried and magnetically stirred on a hot plate until visibly dry. The remaining powder-binder-plasticizer combination was further dried at 60°C overnight. It was then milled with a mortar and pestle and sieved to less than a 60-mesh size fraction.

Weighed out amounts of powders (plus binder and plasticizer) were pressed through various pressure stages up to 138 MPa (20,000 psi) to produce pellets from 0.635 cm to 2.54 cm in diameter. For the pellets made for conductivity tests, 2 g of doped barium cerate-zirconate powder (plus binder and plasticizer) was pressed at 34 MPa (5000 psi) for 1 min, 69 MPa (10000 psi) for 1 min and then at 138 MPa (20000 psi) for 2 min. The molds were lubricated using a 1:2 mixture by weight of stearic acid and odourless kerosene that was homogenized by heating to 60°C. The lubricant was applied to the molds using a cotton swab.

The green pellets were then weighed and measured before being transferred to a porous zirconia sintering plate. The pellets intended for conductivity measurements were sintered on top of larger pellets of the same composition which were then all placed onto the zirconia sintering plate. The BCZNd, BCZEu, BCZGd and BCZY pellets were then sintered at 1600°C for 10 h according to heat treatment Sinter2 in Table 2. The BCZYb pellets were sintered at 1650°C for 10 h according to heat treatment Sinter3 in Table 2. In preparation for conductivity tests, the discoloured surface layer of the pellets was removed using 180 and 400 grit alumina sandpaper (Norton Premium, Home Depot). The sintered

pellets were then weighed and measured for density determination geometrically as well as using volumetric displacement.

Pellets intended for conductivity measurements had platinum electrode layers applied to each side. The samples were placed on an alumina sintering plate which was then placed onto a hotplate set at 60°C. Platinum paste (FERRO) was applied with a brush to one side of the pellets and then left to dry. A second layer was then applied and left to dry before repeating the process and applying two layers of platinum paste to the other side of the pellets. The outside edge of the pellets was cleaned with ethanol to avoid electrical contact between the two sides. The pellets set on the alumina plate were then placed into an oven and heated from room temperature to 1000°C for 2 h and then to 1200°C for 2 h according to heat treatment Electrode1 in Table 2.

4.2.3 Bar and Pellet Characterization

Densities of the sintered bars and pellets were estimated using both geometric and volumetric displacement methods. In both methods, the dry weight of each of the bars was first measured. Using callipers, the geometric values of height, width and length of the bars were measured and bulk volume estimation was obtained. The dry mass divided by the bulk volume then gave the estimated bulk density. In the density measurements using volumetric displacement (Archimedes method), the bars were submerged in isopropanol ($\rho = 0.786 \text{ g/cm}^3$) or ethanol ($\rho = 0.789 \text{ g/cm}^3$) and the volumetric displacement of each was measured. The bars were then left submerged in the isopropanol for 12 h or boiling ethanol for 15 min. The masses of each bar while suspended in the alcohols were measured and the bars were taken out to dry. After external surface alcohol had been wiped away and evaporated, the 'wet' masses of the bars were measured. Using this volume measurement along with the three

masses, the bulk density, open porosity and closed porosity were estimated using the following relations:

$$V_{real} = \frac{m_{dry}}{\rho_{th}} \quad (16)$$

$$V_{cp} = \frac{m_{dry} - m_{sub}}{\rho_a} - V_{real} \quad (17)$$

$$V_{op} = \frac{m_{wet} - m_{dry}}{\rho_a} \quad (18)$$

$$V_{total} = V_{real} + V_{cp} + V_{op} \quad (19)$$

$$\rho_s = \frac{m_{dry}}{m_{dry} - m_{sub}} * \rho_a \quad (20)$$

where m_{dry} is the mass of the bar after sintering, m_{sub} is the mass of the bar submerged in alcohol, m_{wet} is the mass of the bar after drying, V_{real} (or V_{true}) is the volume of the bar minus all porosity, V_{cp} is the volume of the closed porosity within the bar, V_{op} is the volume of the open porosity within the bar, V_{total} is the total or bulk volume, ρ_{th} is the theoretical density of the ceramic matrix, ρ_a is the density of the alcohol at the temperature of testing and ρ_s is the bulk density of the sample bar or pellet.

4.3 Electrochemical Testing

Electrochemical characterization of the polycrystalline sintered pellets was carried out at the Institute for Materials Synthesis and Processing (IEK-1) at the Forschungszentrum Jülich in Germany. The pellets were characterized using impedance spectroscopy in three different atmospheres: wet ($p_{H_2O}=0.025$ atm) 4% H_2 -Ar, dry 4% H_2 -Ar and dry Ar. The ProboStatTM (NorECs AS, Norway) system at IEK-1 (Figure 8A) is comprised of a ProboStatTM cell (1) where the sample is held, positioned and connected to the electrodes (see detailed inner

view of ProboStat™ cell, Figure 8B), a gas mixer (2) to obtain desired gas compositions, a high temperature controlled furnace (3) and a broadband frequency analyzer (4) with a 4-wire interface (5) (schematic of measurement principle shown in Figure 8C) controlled by WinDeta software from Novocontrol Technologies.

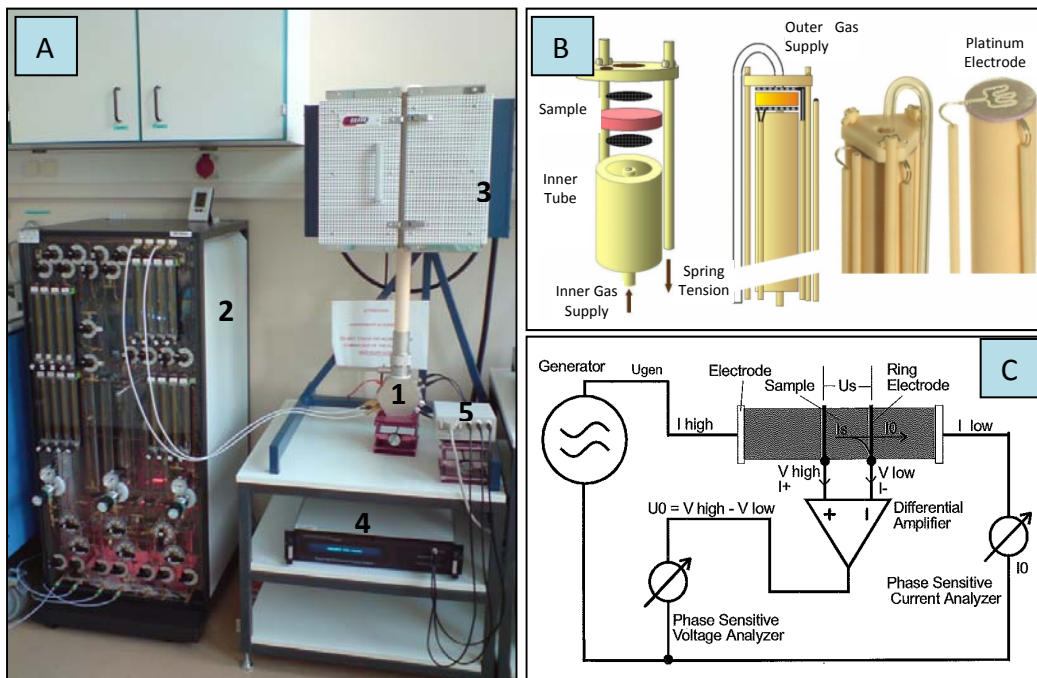


Figure 8: (A) Arrangement of the impedance measurement system consisting of sample holder (1), gas mixer (2), furnace (3), frequency analyzer (4) with 4-wire interface (5), (B) a detailed inner view of the ProboStat™ sample holder and (C) a schematic of the measurement circuit [69]

Impedance spectra were obtained using a frequency response analyzer (Novocontrol-AN) with a frequency range of 50 Hz to 10 MHz with an AC oscillating voltage of 0.4 V or 1.0 V. The samples were heated at a ramp rate of 7.5 K/min to 900°C, held for 11 h and then impedance spectra were obtained during the stepwise cooling process (50°C steps with 30 min dwell times). The impedance measurements were taken for each step at the end of the dwell time. A stray capacitance of 5 pF that originated from the measuring cell wiring was

subtracted from the raw data. Conductivity data from the impedance spectra was determined using ZSimpWin software (Princeton Applied Research).

4.4 Supported Membrane Synthesis

Electrolyte layers were synthesized by the reaction of two screen printed layers on a YSZ or CGO substrate. The first layer consisted of yttrium doped ceria (CeY10) which was then reacted with a layer of BaCO₃, SrCO₃ or CaCO₃.

4.4.1 Support (Substrate) Synthesis

Macroporous substrates were created by warm pressing at 120°C and 1 MPa using powders prepared via the Coatmix® procedure. The powder was composed of the inorganic powders coated with a phenolic resin to produce large and very porous agglomerates. Two basic types of substrates were used: (i) a NiO-8YSZ cermet with a graded porosity and (ii) a NiO-CGO cermet also with graded porosity. Both substrates also included an interlayer (or anode functional layer) of the same composition with smaller particle sizes ($d_{50} = \sim 0.2 \mu\text{m}$) deposited on the pre-sintered substrates (1230°C) by slip casting to smooth the surface. The NiO-8YSZ substrates were further processed and then given a final sintering at 1400°C to achieve a gas tight 8YSZ surface layer (or electrolyte layer) of approximately 8 μm in thickness. Similarly, the CGO-NiO substrates were processed and finally sintered at 1400°C to achieve a gas tight CGO surface layer (or electrolyte layer) of approximately 9-10 μm in thickness. The substrates were then cut into squares with an approximate side length of 2.54 cm.

4.4.2 Layer Screen Printing and Synthesis

The screen printing pastes were prepared from the corresponding inorganic powders with a solution of ethylcellulose (Aldrich) in terpineol (Dupont). Homogeneous fine pastes were achieved by milling of the mixture in a three-roll mill (EXAKT). The pastes were screen printed onto their corresponding

substrates using a constant printing speed, squeegee angle and squeegee pressure. $10 \times 10 \text{ mm}^2$ screens with mesh sizes corresponding to printed (wet) thicknesses of 20 and 40 μm were used. A schematic of the screen printing method can be seen in Figure 9. The CeY10 layer was screen printed onto the centre of the cut substrates to a 20 μm wet thickness, dried at 60°C in a drying oven and then sintered at 1300°C for 8 h (Perovskite4). The second layer of one of the carbonates in either a wet thickness of 20 or 40 μm was then screen printed on top of the sintered CeY10 first layer. The two layers were then reacted at 1300°C (BaCO_3) or 1400°C ($\text{SrCO}_3/\text{CaCO}_3$) for 8 h (heat treatment Perovskite4 or Perovskite1).

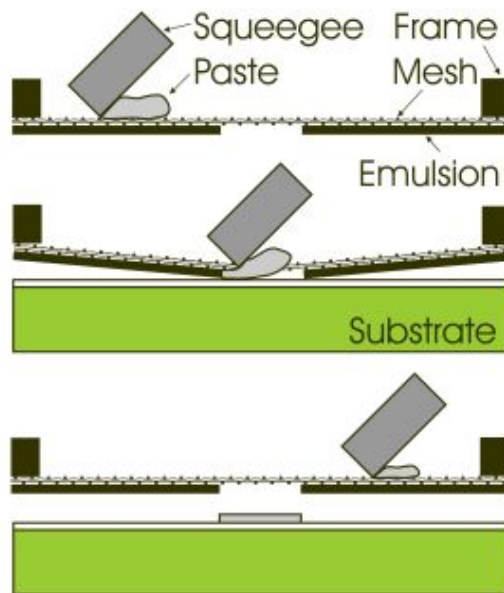


Figure 9: Schematic of the screen printing process [70]

4.4.3 Membrane Characterization

Membranes were cross-sectioned, mounted and then polished before scanning electron microscopy was performed by using a Zeiss Ultra55 electron microscope. Laser topography measurements were made using a Cyberscan

CT200 with a DRS500 sensor. Surface x-ray diffraction measurements were performed using a Siemens D5000 diffractometer with $\text{CuK}\alpha$ ($\lambda = 1.54\text{\AA}$) radiation with a diffraction angle (θ) range of 20° to 80° .

5.0 Results and Discussion

5.1 Cerate Synthesis

Prior to perovskite formation, nanoparticle sized powders of ceria along with similar particle sized powders of Eu_2O_3 , Gd_2O_3 , Sc_2O_3 , Sm_2O_3 , Tb_2O_3 and Y_2O_3 in various compositions were solid state reacted in order to introduce oxygen vacancies into the fluorite matrix.

5.1.1 Dopant Solubility

To test dopant solubility in the ceria fluorite matrix, various compositions of doped ceria samples were synthesized. A summary of the compositions attempted and the XRD results is shown in Table 4.

Table 4: Doped ceria compositions and summary of XRD results

Sample	Desired Composition	Pre-HT Composition (molar ratio)	Heat Treatment	Single/Multi Phase
CeEu10	Ce _{0.90} Eu _{0.10} O _{1.95}	CeO ₂ :Eu ₂ O ₃ (9:0.5)	Cerate1	Multi
CeEu15	Ce _{0.85} Eu _{0.15} O _{1.925}	CeO ₂ :Eu ₂ O ₃ (8.5:0.75)	Cerate1	Multi
CeEu20	Ce _{0.80} Eu _{0.20} O _{1.90}	CeO ₂ :Eu ₂ O ₃ (8:1)	Cerate1	Multi
CeGd10	Ce _{0.90} Gd _{0.10} O _{1.95}	CeO ₂ :Gd ₂ O ₃ (9:0.5)	Cerate1	Single
CeGd15	Ce _{0.85} Gd _{0.15} O _{1.925}	CeO ₂ :Gd ₂ O ₃ (8.5:0.75)	Cerate1	Multi
CeGd20	Ce _{0.80} Gd _{0.20} O _{1.90}	CeO ₂ :Gd ₂ O ₃ (8:1)	Cerate1	Multi
CeSc3	Ce _{0.97} Sc _{0.03} O _{1.985}	CeO ₂ :Sc ₂ O ₃ (9.7:0.15)	Cerate1	Multi
CeSc5	Ce _{0.95} Sc _{0.05} O _{1.975}	CeO ₂ :Sc ₂ O ₃ (9.5:0.25)	Cerate1	Multi
CeSc10	Ce _{0.90} Sc _{0.10} O _{1.95}	CeO ₂ :Sc ₂ O ₃ (9:0.5)	Cerate1	Multi
CeSc15	Ce _{0.85} Sc _{0.15} O _{1.925}	CeO ₂ :Sc ₂ O ₃ (8.5:0.75)	Cerate1	Multi
CeSc20	Ce _{0.80} Sc _{0.20} O _{1.90}	CeO ₂ :Sc ₂ O ₃ (8:1)	Cerate1	Multi
CeSm10	Ce _{0.90} Sm _{0.10} O _{1.95}	CeO ₂ :Sm ₂ O ₃ (9:0.5)	Cerate1	Single
CeSm15	Ce _{0.85} Sm _{0.15} O _{1.925}	CeO ₂ :Sm ₂ O ₃ (8.5:0.75)	Cerate1	Single
CeSm20	Ce _{0.80} Sm _{0.20} O _{1.90}	CeO ₂ :Sm ₂ O ₃ (8:1)	Cerate1	Single
CeTb10	Ce _{0.90} Tb _{0.10} O _{1.95}	CeO ₂ :Tb ₂ O ₃ (9:0.5)	Cerate1	Multi
CeTb15	Ce _{0.85} Tb _{0.15} O _{1.925}	CeO ₂ :Tb ₂ O ₃ (8.5:0.75)	Cerate1	Multi
CeTb20	Ce _{0.80} Tb _{0.20} O _{1.90}	CeO ₂ :Tb ₂ O ₃ (8:1)	Cerate1	Multi
CeY10	Ce _{0.90} Y _{0.10} O _{1.95}	CeO ₂ :Y ₂ O ₃ (9:0.5)	Cerate1	Single
CeY15	Ce _{0.85} Y _{0.15} O _{1.925}	CeO ₂ :Y ₂ O ₃ (8.5:0.75)	Cerate1	Single
CeY20	Ce _{0.80} Y _{0.20} O _{1.90}	CeO ₂ :Y ₂ O ₃ (8:1)	Cerate1	Single

The XRD results show that only the samples CeGd10, CeSm10, CeSm15, CeSm20, CeY10, CeY15 and CeY20 (Figures 10-16) were monophasic and therefore show that there could be incomplete reaction in the other cases. A commercially obtained 20% gadolinium-doped ceria sample was also tested with XRD (Figure 17) and was also monophasic but had much broader peaks. These broader peaks indicate some amorphous properties in the commercially obtained CeGd20 nanopowder. These single phase doped ceria compositions can, therefore, be used as the first layer in the layer screen printing and synthesis.

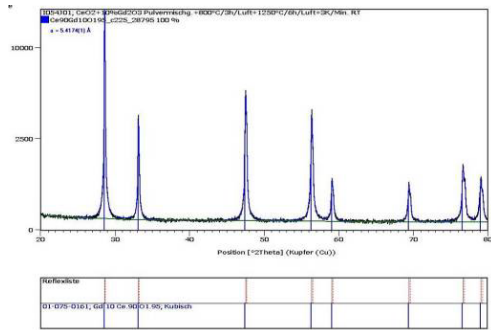


Figure 10: XRD results from sample CeGd10

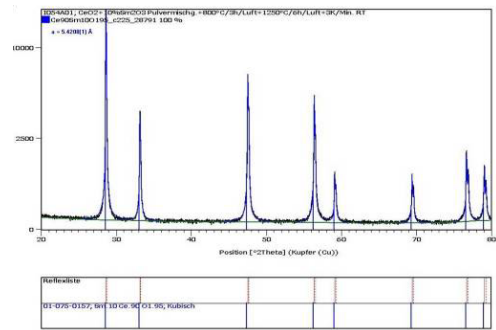


Figure 11: XRD results from sample CeSm10

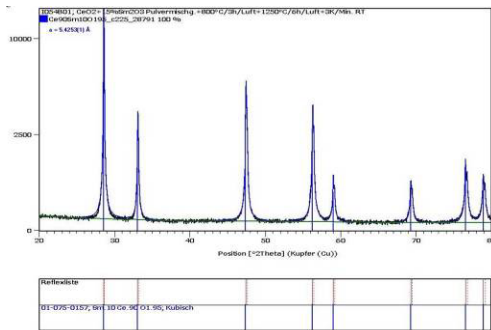


Figure 12: XRD results from sample CeSm15

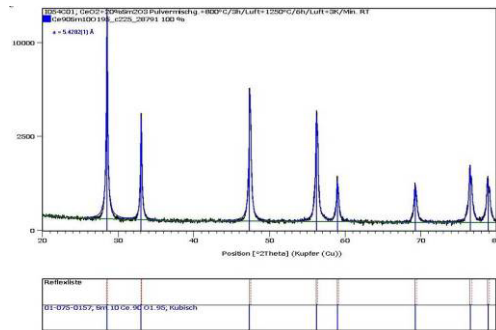


Figure 13: XRD results from sample CeSm20

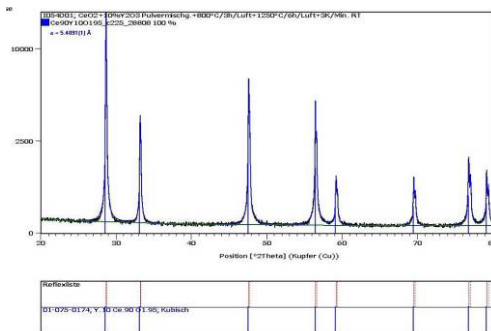


Figure 14: XRD results from sample CeY10

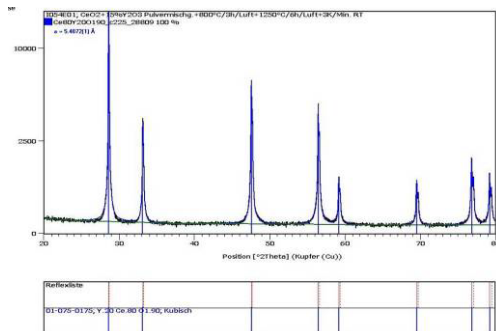


Figure 15: XRD results from sample CeY15

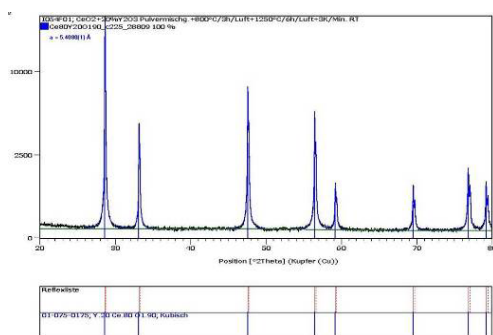


Figure 16: XRD results from sample CeY20

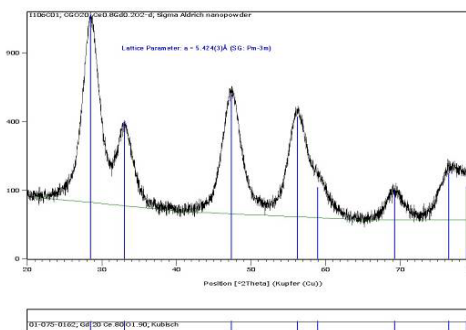


Figure 17: XRD analysis of commercially obtained CeGd20 nanopowder

5.2 Doped Cerate Perovskite Synthesis

The starting powders used and their particle sizes are shown in Table 5. A very noticeable decrease in particle size of the barium and strontium carbonates after milling is seen when compared to the particle sizes of the original commercially obtained powders in Table 1.

Table 5: Perovskite synthesis starting powders and particle sizes

Powder Sample	d50 (µm)	d90 (µm)	Milling Method
CeGd10	0.29	0.56	Mortar and Pestle
CeGd20*	<0.100	<0.100	Mortar and Pestle
CeSc10	0.59	9.02	Mortar and Pestle
CeSm10	0.33	0.63	Mortar and Pestle
CeSm15	2.14	12.53	Mortar and Pestle
CeSm20	1.00	7.00	Mortar and Pestle
CeY10	0.29	0.55	Mortar and Pestle
CeY15	0.47	3.16	Mortar and Pestle
CeY20	0.86	6.80	Mortar and Pestle
BaCO ₃	1.48	3.20	Ball Milling (72h) + Mortar and Pestle
SrCO ₃	1.25	2.86	Ball Milling (72h) + Mortar and Pestle
CaCO ₃	1.78	4.03	Ball Milling (72h) + Mortar and Pestle

*Commercially obtained

All of the perovskite synthesis methods tested involved barium, strontium and calcium oxides. Due to the reactivity of BaO, CaO and SrO, crucible material selection was critical. DTA/TG was used to test for possible unwanted side

reactions. Figure 18 shows the DTA/TG results for the reaction of $\text{Ce}_{0.90}\text{Gd}_{0.10}\text{O}_{1.95}$ with a stoichiometric amount of CaCO_3 . Thermal decomposition of CaCO_3 into CaO and CO_2 accounts for the endothermic peak at 827.2°C on the DTA curve and no other peaks are observed. The mass loss ($\sim 15\%$) due to the evolution of CO_2 gas can clearly be seen on the TG curve.

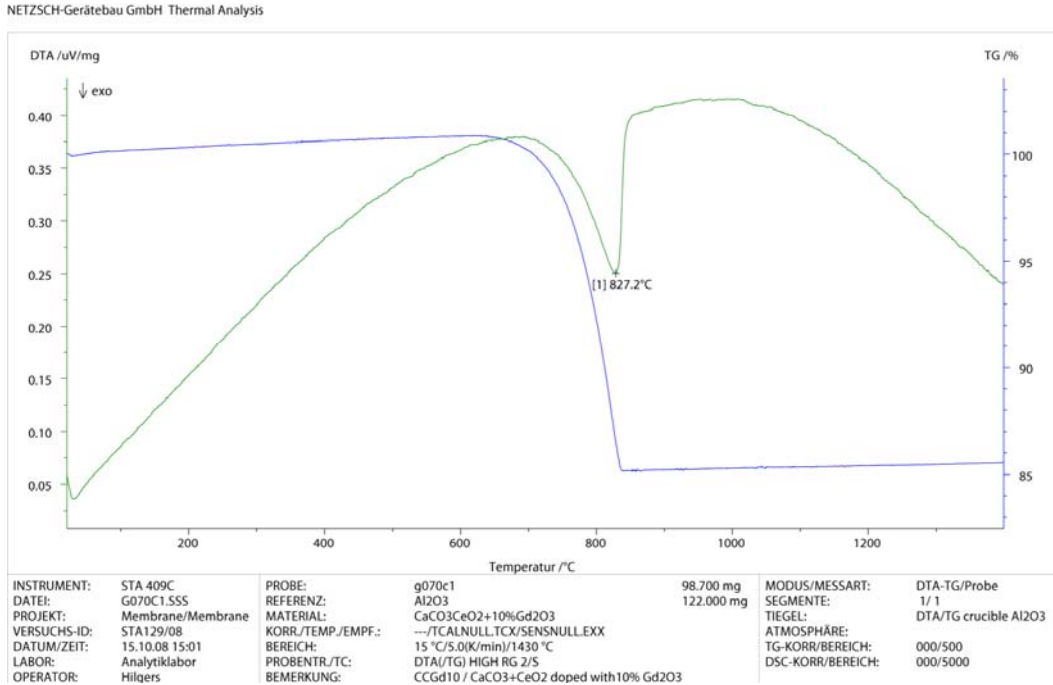


Figure 18: DTA for reaction of $\text{Ce}_{0.90}\text{Gd}_{0.10}\text{O}_{1.95}$ with CaCO_3

Figure 19 shows the reaction of $\text{Ce}_{0.90}\text{Gd}_{0.10}\text{O}_{1.95}$ with a stoichiometric amount of CaCO_3 again but with the addition of an equal mass of Al_2O_3 . As above, the endothermic peak of carbonate decomposition appears just over 800°C along with the corresponding decrease in mass. However, a second endothermic peak is noted at approximately 1380°C . Figure 20 is again $\text{Ce}_{0.90}\text{Gd}_{0.10}\text{O}_{1.95}$ with a stoichiometric amount of CaCO_3 but with an equal mass of ZrO_2 instead of Al_2O_3 . The DTA curve clearly shows the carbonate decomposition peak, but there are no additional peaks. It appears that, at temperatures approaching 1400°C , crucibles made from alumina (Al_2O_3) are not suitable for the current work.

Zirconia (ZrO_2) showed no reactivity with the powders tested and was, therefore, used extensively as the main type of crucible for heat treatment.

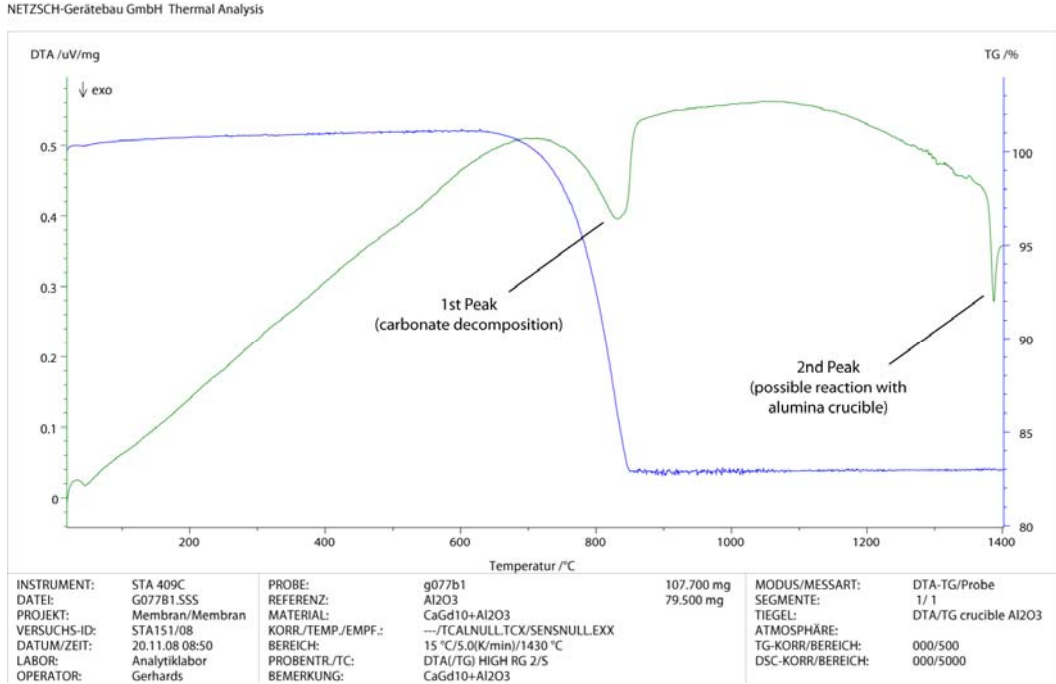


Figure 19: DTA for reaction of $Ce_{0.90}Gd_{0.10}O_{1.95} + CaCO_3 + Al_2O_3$

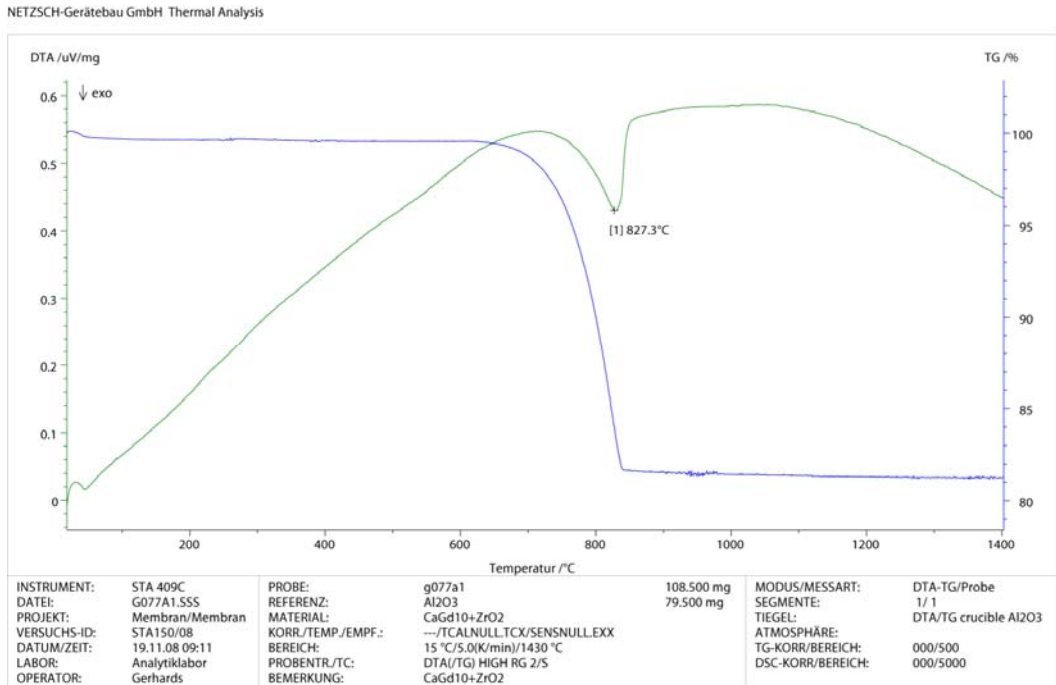


Figure 20: DTA for reaction of $Ce_{0.90}Gd_{0.10}O_{1.95} + CaCO_3 + ZrO_2$

Initial attempts to produce perovskite powders for bar and pellet synthesis focused on a two stage approach (DCC method). This two stage approach was chosen because it was more closely related to the final screen printed layer process. This two stage approach consisted of an initial synthesis of monophasic doped cerate followed by a second solid state reaction with a carbonate for the transformation to perovskite. This method of powder synthesis, however, did not lead to the formation of any monophasic perovskite powders. A summary of the results from this synthesis method can be seen in Table 6. Even in the case where the carbonates were reacted with the commercially obtained CeGd20 powder (samples BaGd20, CaGd20 and SrGd20), no monophasic perovskites were synthesized.

Table 6: Attempts at perovskite synthesis via DCC method

Sample	Desired Composition	Pre-HT Composition (molar ratio)	Heat Treatment	Single/Multi Phase
BaGd10	BaCe _{0.90} Gd _{0.10} O _{2.95}	BaCO ₃ /Ce _{0.90} Gd _{0.10} O _{1.95} (1/1)	Perovskite1	Multi
BaGd10_S	BaCe _{0.90} Gd _{0.10} O _{2.95}	BaCO ₃ /Ce _{0.90} Gd _{0.10} O _{1.95} (1/1)	Sinter1	Multi
BaGd20	BaCe _{0.80} Gd _{0.20} O _{2.90}	BaCO ₃ /Ce _{0.80} Gd _{0.20} O _{1.90} (1/1)	Perovskite2	Multi
BaSc10*	BaCe _{0.90} Sc _{0.10} O _{2.95}	BaCO ₃ /CeSc10 (1/1)	Perovskite1	Multi
BaSm10	BaCe _{0.90} Sm _{0.10} O _{2.95}	BaCO ₃ /Ce _{0.90} Sm _{0.10} O _{1.95} (1/1)	Perovskite1	Multi
BaY10	BaCe _{0.90} Y _{0.10} O _{2.95}	BaCO ₃ /Ce _{0.90} Y _{0.10} O _{1.95} (1/1)	Perovskite1	Multi
CaGd20	CaCe _{0.80} Gd _{0.20} O _{2.90}	CaCO ₃ /Ce _{0.80} Gd _{0.20} O _{1.90} (1/1)	Perovskite2	Multi
CaSc10*	CaCe _{0.90} Sc _{0.10} O _{2.95}	CaCO ₃ /CeSc10 (1/1)	Perovskite1	Multi
SrGd20	SrCe _{0.80} Gd _{0.20} O _{2.90}	SrCO ₃ /Ce _{0.80} Gd _{0.20} O _{1.90} (1/1)	Perovskite2	Multi

***The Sc-doped ceria (BaSc10/CaSc10) was not monophasic prior to reaction with carbonate**

Due to the difficulty in producing monophasic perovskite powders via the DCC method, the mixed oxide (MO) method for synthesis was used in order to test the properties of the materials. A summary of the progress made with this method can be seen in Table 7. After calcination at 1200°C for 8 h (Perovskite3), the BaY10 sample was found to be monophasic by XRD. The XRD results for the BaY10 sample appear in Figure 21 showing only a barium cerate orthorhombic

perovskite phase. Increasing the yttria content further seemed to result in the formation of a monoclinic phase. This can be seen in samples BaY15 and BaY20 in Figures 22 and 23, respectively (the characteristic peaks showing monoclinic distortion are marked). This agrees with studies done by Takeuchi et al. [71] which show that for $\text{BaCe}_{1-x}\text{Y}_x\text{O}_{3-\delta}$ compositions with x greater or equal to 0.15, heat treatments in air result in mixed phase structures and the appearance of a monoclinic phase.

Table 7: Mixed oxide method perovskite synthesis

Sample	Desired Composition	Pre-HT Composition (molar ratio)	Heat Treatment	Single/Multi Phase
BaY10	$\text{BaCe}_{0.90}\text{Y}_{0.10}\text{O}_{2.95}$	$\text{BaCO}_3/\text{CeO}_2/\text{Y}_2\text{O}_3$ (10/9/0.5)	Perovskite3	Single
BaY15	$\text{BaCe}_{0.85}\text{Y}_{0.15}\text{O}_{2.925}$	$\text{BaCO}_3/\text{CeO}_2/\text{Y}_2\text{O}_3$ (10/8.5/0.75)	Perovskite3	Multi
BaY20	$\text{BaCe}_{0.80}\text{Y}_{0.20}\text{O}_{2.90}$	$\text{BaCO}_3/\text{CeO}_2/\text{Y}_2\text{O}_3$ (10/8/1)	Perovskite3	Multi
CaY10	$\text{CaCe}_{0.90}\text{Y}_{0.10}\text{O}_{2.95}$	$\text{CaCO}_3/\text{CeO}_2/\text{Y}_2\text{O}_3$ (10/9/0.5)	Perovskite3	Multi
CaY10	$\text{CaCe}_{0.90}\text{Y}_{0.10}\text{O}_{2.95}$	$\text{CaCO}_3/\text{CeO}_2/\text{Y}_2\text{O}_3$ (10/9/0.5)	Perovskite1	Multi
SrY10	$\text{SrCe}_{0.90}\text{Y}_{0.20}\text{O}_{2.95}$	$\text{SrCO}_3/\text{CeO}_2/\text{Y}_2\text{O}_3$ (10/9/0.5)	Perovskite3	Multi
SrY10	$\text{SrCe}_{0.90}\text{Y}_{0.20}\text{O}_{2.95}$	$\text{SrCO}_3/\text{CeO}_2/\text{Y}_2\text{O}_3$ (10/9/0.5)	Perovskite1	Multi
BaGd10	$\text{BaCe}_{0.90}\text{Gd}_{0.10}\text{O}_{2.95}$	$\text{BaCO}_3/\text{CeO}_2/\text{Gd}_2\text{O}_3$ (10/9/0.5)	Perovskite3	Multi
CaGd10	$\text{CaCe}_{0.90}\text{Gd}_{0.10}\text{O}_{2.95}$	$\text{CaCO}_3/\text{CeO}_2/\text{Gd}_2\text{O}_3$ (10/9/0.5)	Cancelled	Cancelled
SrGd10	$\text{SrCe}_{0.90}\text{Gd}_{0.10}\text{O}_{2.95}$	$\text{SrCO}_3/\text{CeO}_2/\text{Gd}_2\text{O}_3$ (10/9/0.5)	Cancelled	Cancelled
BaSm10	$\text{BaCe}_{0.90}\text{Sm}_{0.10}\text{O}_{2.95}$	$\text{BaCO}_3/\text{CeO}_2/\text{Sm}_2\text{O}_3$ (10/9/0.5)	Perovskite3	Multi
CaSm10	$\text{CaCe}_{0.90}\text{Sm}_{0.10}\text{O}_{2.95}$	$\text{CaCO}_3/\text{CeO}_2/\text{Sm}_2\text{O}_3$ (10/9/0.5)	Cancelled	Cancelled
SrSm10	$\text{SrCe}_{0.90}\text{Sm}_{0.10}\text{O}_{2.95}$	$\text{SrCO}_3/\text{CeO}_2/\text{Sm}_2\text{O}_3$ (10/9/0.5)	Cancelled	Cancelled

Synthesis of BaSm10 and BaGd10 by the MO method at 1200°C for 8 h (Perovskite3) also resulted in only multiphase powders as shown in Figures 24 and 25, respectively. In the BaGd10 sample, one can see a similar peak distortion (marked with arrows) as in the BaY15 and BaY20 samples. This could be indicative of the same monoclinic phase being present. It is possible that reactions at higher temperatures could lead to better results for these samples.

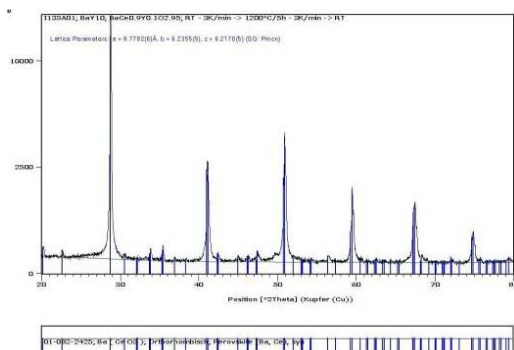


Figure 21: XRD results from BaY10 sample (MO, Perovskite3)

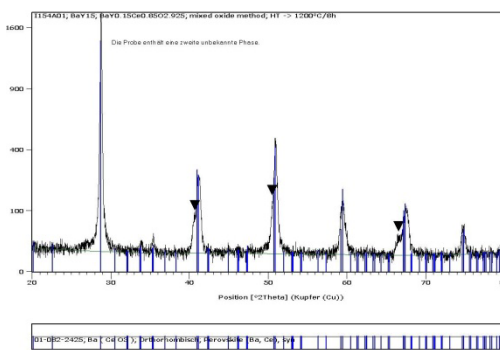


Figure 22: XRD results from BaY15 sample with marked peaks indicating the presence of a monoclinic phase (MO, Perovskite3)

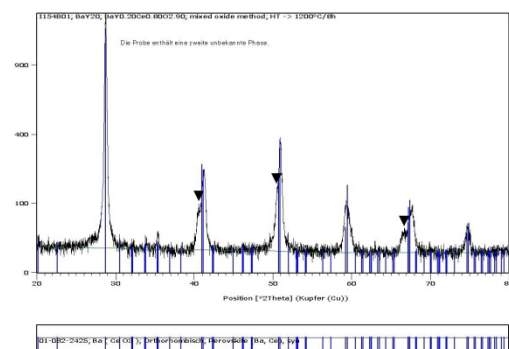


Figure 23: XRD results from BaY20 sample with marked peaks indicating the presence of a monoclinic phase (MO, Perovskite3)

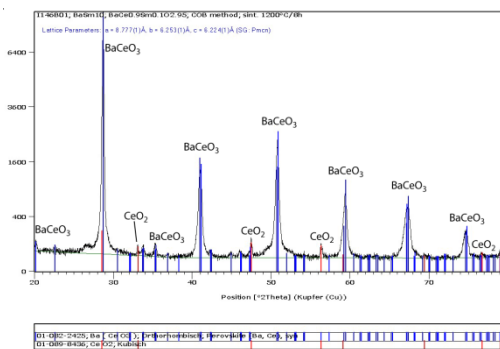


Figure 24: XRD results from BaSm10 sample (MO, Perovskite3)

The XRD results for the MO method of synthesis of CaY10 and SrY10 (Figures 26 and 28) showed incomplete reactions and were heat treated again at a higher temperature (heat treatment Perovskite1). This heat treatment, however, did not lead to much improvement and there were still the same phases present in each sample as can be seen in Figures 27 and 29. Attempts to synthesize $\text{SrCe}_{0.90}\text{Y}_{0.20}\text{O}_{2.95}$ via the triple oxide method (TO), in which SrO was used instead of SrCO_3 , resulted in a multiphase powder after synthesis at 1400°C for 8 h as can be seen in Figure 30 (heat treatment Perovskite1). In future powder synthesis attempts using the triple oxide method, a glove box combined with an

inert atmosphere such as argon should be used when weighing appropriate amounts alkaline earth oxides to avoid any potential reaction with $H_2O(g)$ and $CO_2(g)$ in air. Perovskites with Ca and Sr on the A-site seem to be much more difficult to synthesize than perovskites with Ba. This could be due to the difference in tolerance factors for $BaCeO_3$, $SrCeO_3$ and $CaCeO_3$ which were calculated to be 0.94, 0.88 and 0.85, respectively.

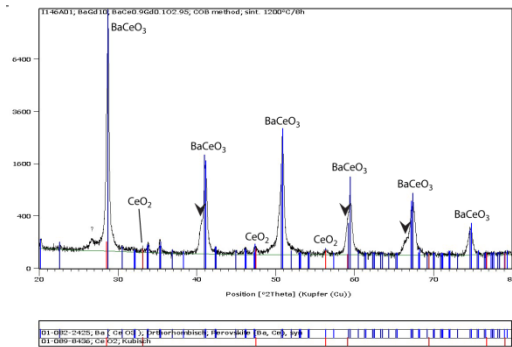


Figure 25: XRD results from BaGd10 sample (MO, Perovskite3)

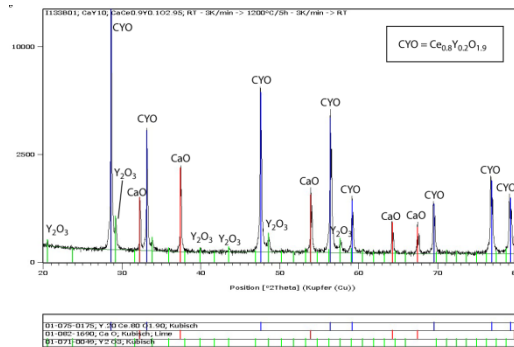


Figure 26: XRD results from CaY10 (MO, Perovskite3)

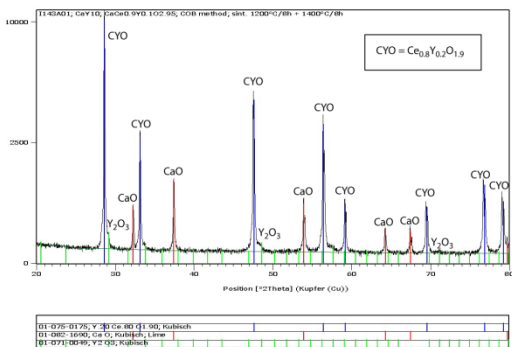


Figure 27: XRD results for sample CaY10 (MO, Perovskite3+Perovskite1)

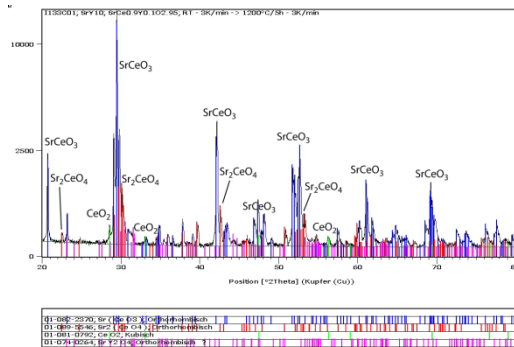


Figure 28: XRD results for sample SrY10 (MO, Perovskite3)

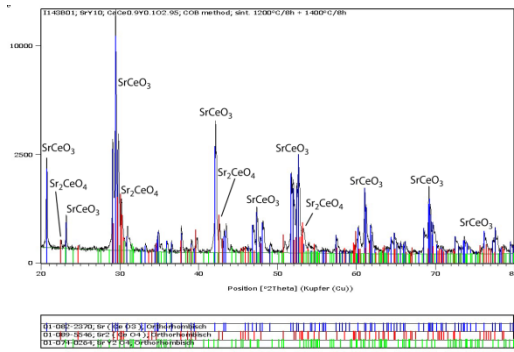


Figure 29: XRD results for sample SrY10 (MO, Perovskite3+Perovskite1)

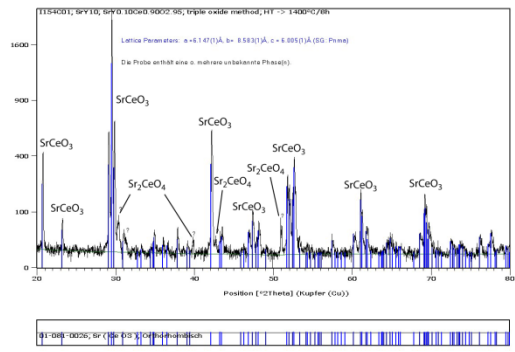


Figure 30: XRD results for samples SrY10 (TO, Perovskite1)

The raw monophasic BaY10 powders were pressed into bars and sintered at 1550°C for 10 h (Sinter1). These bars can be seen in Figure 31.



Figure 31: Sintered BaY10 bars

Densities were measured geometrically as well as using the Archimedes method. The Archimedes method also allowed for porosity information to be gathered. These results are summarized in Table 8.

Table 8: Density and porosity data for a sintered BaY10 bar

Density			Porosity			
Theoretical (g/cm ³)	Geometric		Archimedes		Open	Closed
	(g/cm ³)	(% theor.)	(g/cm ³)	(% theor.)	(% Vol.)	(% Vol.)
6.38	5.35	83.86	5.49	85.99	5.03	8.99

The theoretical density of BaCe_{0.90}Y_{0.10}O_{2.95} was calculated using lattice parameters measured with XRD. Although the bars are fairly dense at ~86% of the theoretical value, there is still room for further densification.

5.3 Supported Layer Synthesis

5.3.1 Paste Preparation, Screen Printing, and Synthesis

Layer deposition was completed using the screen printing method. Pastes were prepared from CeY10, BaCO₃, SrCO₃ and CaCO₃ powders and screen printed onto either NiO-8YSZ or NiO-CGO substrates prepared via the Coatmix[®] method. The screen printing pastes prepared can be seen in Table 9. The binder/solvent solution used was 6% ethyl cellulose in terpineol. Binder to powder mass ratios and powder to liquid volume ratios were adjusted in order to achieve a suitable viscosity for screen printing. Some larger particles and agglomerates were noticed in the carbonate pastes.

Table 9: Prepared pastes

Paste ID	Powder	Mass					Volume
		B/L	B/P	Powder	Binder	Solvent	Powder
Paste 1	CeY10	8.7%	6.8%	56.4%	3.8%	39.7%	14.8%
Paste 2	BaCO ₃	3.3%	2.5%	57.1%	1.4%	41.4%	22.4%
Paste 3	SrCO ₃	3.8%	3.5%	52.3%	1.8%	45.8%	22.6%
Paste 4	CaCO ₃	4.1%	3.5%	54.1%	1.9%	44.0%	27.2%

***B/L = binder/liquid; B/P = binder/powder**

The first layer of Ce_{0.90}Y_{0.10}O_{1.95} (CeY10) paste (Paste 1) was screen printed with a wet thickness of ~20 μm, dried and then sintered at 1300°C for 8 h (Perovskite4).

Pastes of BaCO_3 , SrCO_3 and CaCO_3 (Pastes 2, 3 and 4) were then deposited as second layers with wet thicknesses of $20\ \mu\text{m}$ or $40\ \mu\text{m}$, dried and heat treated at either 1300°C or 1400°C for 8 h (Perovskite4/Perovskite1).

5.3.2 NiO-8YSZ Substrates

The NiO-8YSZ substrates were $30 \times 30\ \text{mm}^2$ (1.5 mm thick) and were composed of a NiO-8YSZ cermet with a surface smoothing interlayer of the same composition (anode functional layer) as well as a screen printed and final sintered (1400°C) gas tight electrolyte layer of 8YSZ. An SEM cross-section of a NiO-8YSZ substrate with the different layers labeled is shown in Figure 32.

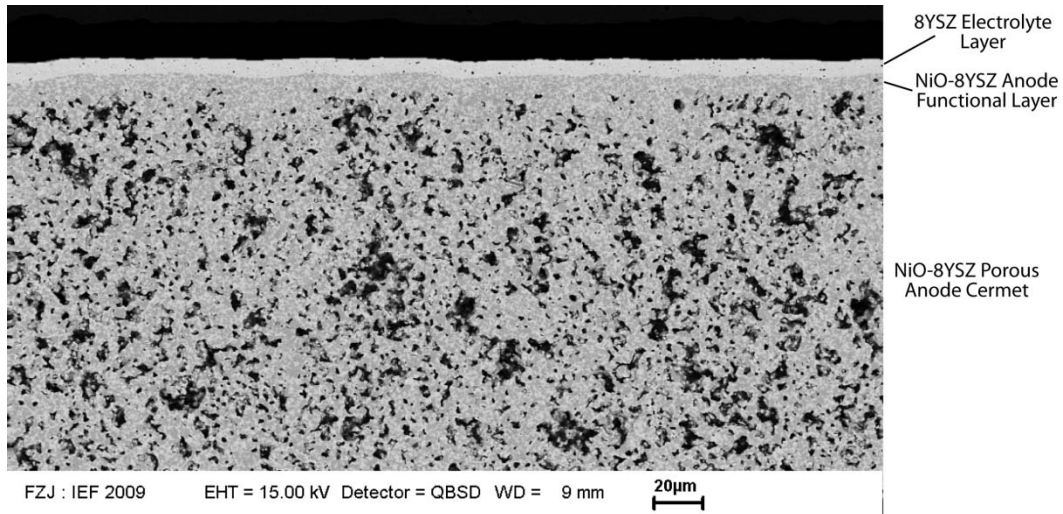


Figure 32: SEM cross-section of a NiO-8YSZ substrate

The screen printed samples and their compositions and synthesis conditions using the NiO-8YSZ substrates can be seen in Table 10.

Table 10: Screen printed samples on NiO-8YSZ substrates

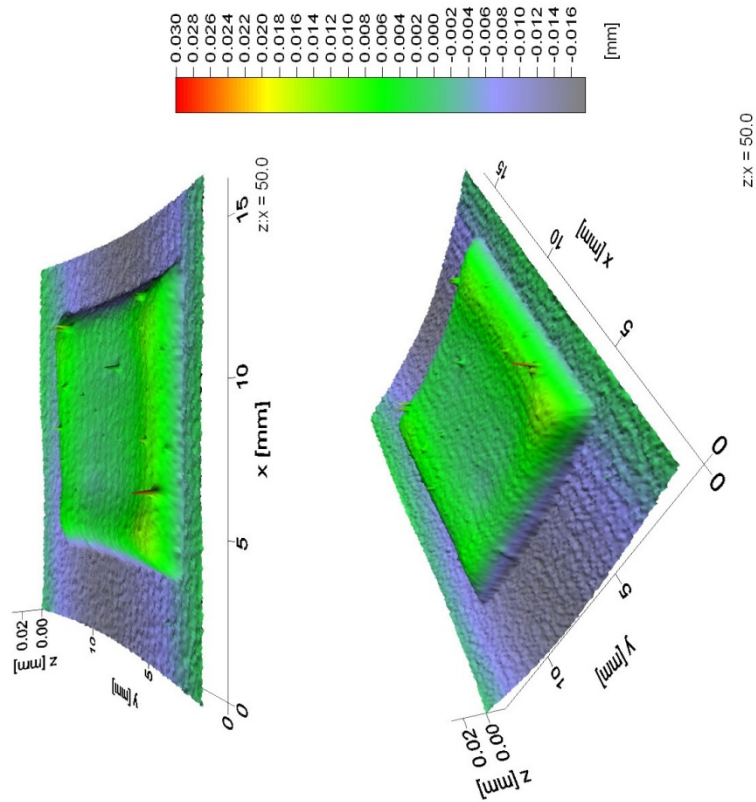
Sample	Substrate		Layers					
			First			Second		
	Type	Temp.	Type	Thickness	Temp.	Type	Thickness	Temp.
BCY10-2020-YSZ	NiO-8YSZ	1400°C	Ce _{0.90} Y _{0.10} O _{1.95}	20 μm	1300°C	BaCO ₃	20 μm	1300°C
BCY10-2040-YSZ	NiO-8YSZ	1400°C	Ce _{0.90} Y _{0.10} O _{1.95}	20 μm	1300°C	BaCO ₃	40 μm	1300°C
SCY10-2020-YSZ	NiO-8YSZ	1400°C	Ce _{0.90} Y _{0.10} O _{1.95}	20 μm	1300°C	SrCO ₃	20 μm	1400°C
SCY10-2040-YSZ	NiO-8YSZ	1400°C	Ce _{0.90} Y _{0.10} O _{1.95}	20 μm	1300°C	SrCO ₃	40 μm	1400°C
CCY10-2020-YSZ	NiO-8YSZ	1400°C	Ce _{0.90} Y _{0.10} O _{1.95}	20 μm	1300°C	CaCO ₃	20 μm	1400°C
CCY10-2040-YSZ	NiO-8YSZ	1400°C	Ce _{0.90} Y _{0.10} O _{1.95}	20 μm	1300°C	CaCO ₃	40 μm	1400°C

5.3.2.1 Doped Ceria Layer

Laser topography was used to investigate the dried and sintered first layer of CeY10 and the results can be seen in Figures 32 and 33, respectively. Using these results, the average thickness of the dried CeY10 layer was determined to be ~15 μm. After sintering, the average thickness was reduced to ~10 μm. There was also noticeable bending in the substrate which was generally only through one axis and was likely a result of differential shrinkage.

(CY10-T2-dried-toprasta)

163 x 140 pts 16.200 x 13.900 x 0.048 mm (step zize: 100.0 x 100.0 µm)



deflection: -0.017 mm
 x curvature: -0.515±2.512 m⁻¹ (-0.148 .. 14.150 m⁻¹)
 y curvature: -0.626±1.976 m⁻¹ (0.573 .. 14.772 m⁻¹)

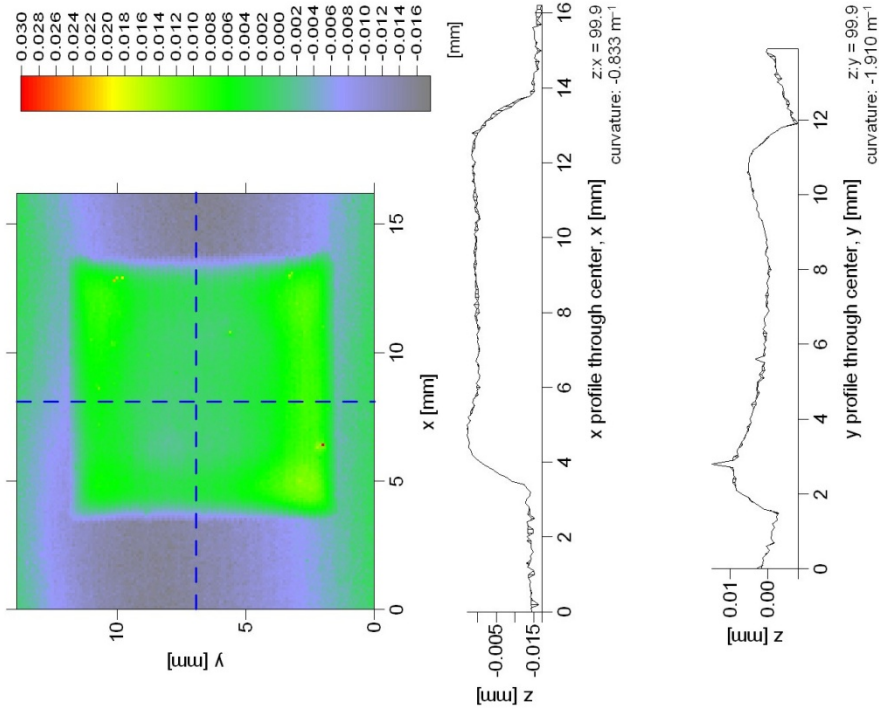
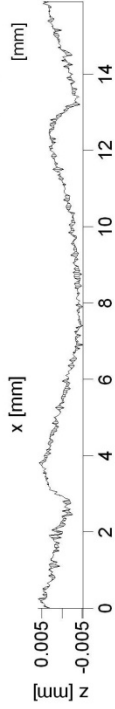
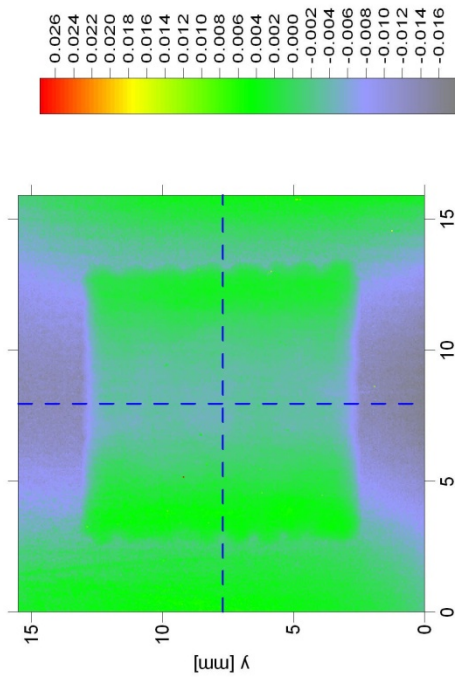
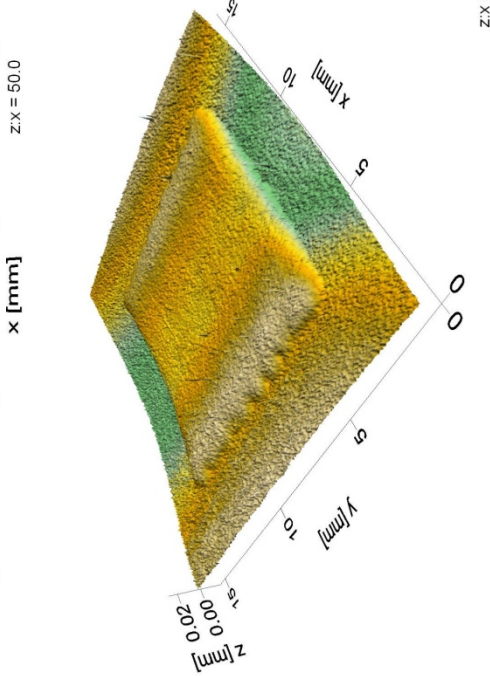
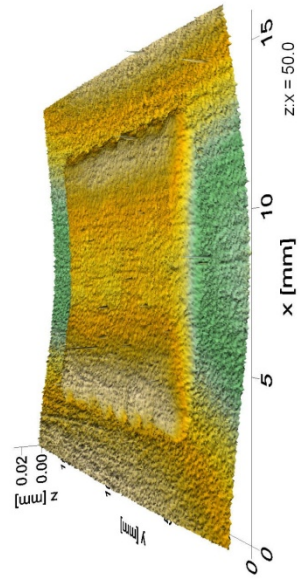


Figure 33: Laser topography data for the CeY10 dried first layer

(CY10_17_sintered_normalized)

319 x 311 pts 15.900 x 15.500 x 0.046 mm (step size: 50.0 x 50.0 μm)



x profile through center, x [mm]
z:x = 106.0
curvature: 0.493 m⁻¹



y profile through center, y [mm]
z:y = 106.0
curvature: -0.575 m⁻¹

deflection: -0.018 mm
x curvature: 0.513±0.065 m⁻¹ (0.405 .. 0.683 m⁻¹)
y curvature: -0.460±0.162 m⁻¹ (-0.176 .. -0.649 m⁻¹)

9.2.2009 13:52 by operator with Banded Surface Script V. 1.1; D:\Scans_2009\Gibson\CY10\Sintered\CY10_17_sintered_normalized_multi.srf

Figure 34: Laser topography data for the CeY10 sintered first layer

A top-view photograph of the sintered CeY10 first layer on the NiO-8YSZ substrate is shown in Figure 35, while SEM cross-sectional micrographs are shown in Figure 36. EDX analysis is shown in Figure 73 (Appendix I). The SEM images clearly show a distinct additional layer on top of the different layers of the substrate. The top layer (I) corresponds to the screen printed CeY10 layer and it can be seen that, although the layer is very porous, a uniform thickness and flat surface was achieved. The application of a thick layer on a pre-sintered substrate results in the electrolyte being sintered under constraint [72] and this could be the reason for limited densification. The second layer (II) is the gas tight 8YSZ layer which rests on top of the functional anode layer (III) composed of NiO and 8YSZ grains.

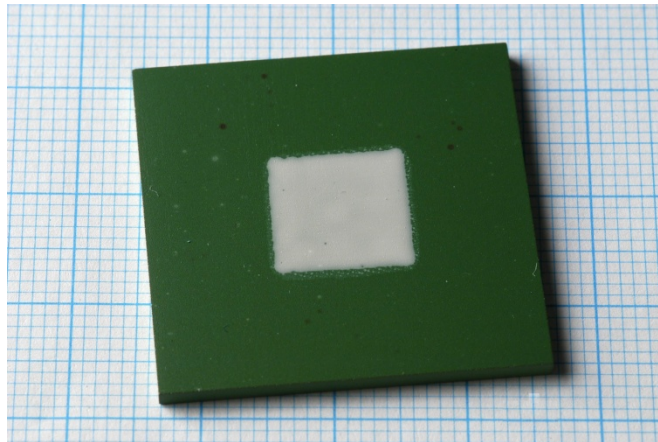


Figure 35: Sintered CeY10 first layer on NiO-8YSZ substrate

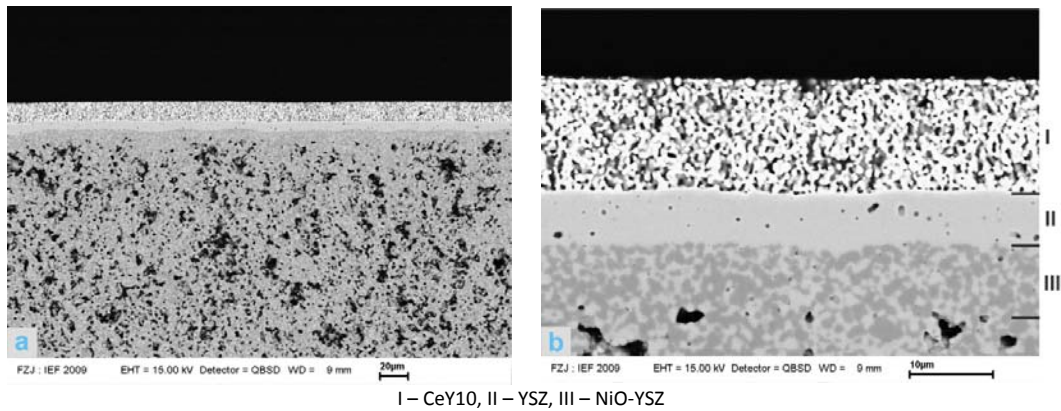


Figure 36: SEM cross-sections of sintered CeY10 first layer on NiO-8YSZ substrate

5.3.2.2 Barium Carbonate Second Layer

Figure 37 shows top view photographs of the final heat treated layers and substrates of (a) sample BCY10-2020-YSZ and (b) sample BCY10-2040-YSZ. A noticeable ring or halo can be seen around the screen printed layers in both samples and corresponds to extended reaction of excess BaO with the YSZ of the substrate forming barium zirconate (BaZrO_3). It can be seen that the thicker layer of BaCO_3 in sample BCY10-2040-YSZ resulted in a larger area of reaction with the substrate and, therefore, a larger ring or halo. A different surface colour and morphology as well as an increased number of surface defects were also noticed in sample BCY10-2040-YSZ. This, again, is likely due to BaCO_3 being present in excess amount.

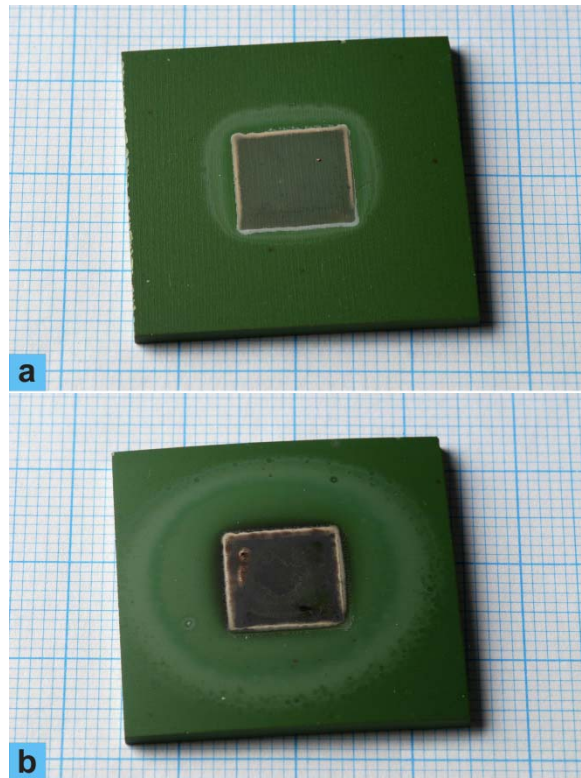


Figure 37: Photographs of samples: (a) BCY10-2020-YSZ and (b) BCY10-2040-YSZ

Figure 38 shows SEM cross-sectional micrographs of (a-b) sample BCY10-2020-YSZ and (c-d) BCY10-2040-YSZ. EDX analyses of the cross-sections of samples BCY10-2020-YSZ (Figure 74) and BCY10-2040-YSZ (Figure 75) are found in Appendix I. Four different regions are present on top of the porous NiO-8YSZ substrate. Section I is very dense and likely composed of $\text{BaCe}_{1-x}\text{Y}_x\text{O}_{3-\delta}$ with the x value most likely being approximately 0.10. It can be noticed that the first section becomes much thicker with an increased amount of BaCO_3 which could mean that there remains some unreacted BaO. Section I* is made up principally of the same composition as section I, but with some Zr enriched grains. The Zr is due to extended diffusion from the YSZ layer. Section II in sample BCY10-2020-YSZ (Figure 38b) contains Ba, Ce and Zr and is most likely of the composition $\text{Ba}(\text{Ce}_{1-x}\text{Zr}_x)_{1-y}\text{Y}_y\text{O}_{3-\delta}$ with the fraction of Ce decreasing towards the YSZ layer (III). These Zr-substituted barium cerates have shown greatly improved stability with limited decreases in conductivity [12,19,50] and future investigations should

focus on the manufacturing of these types of membranes. Section II in sample BCY10-2040-YSZ (Figure 38d) is similar, but is much thicker with a very large lower section composed exclusively of yttria doped BaZrO₃ which is most likely due to the greater amount of BaO available for reaction with the 8YSZ layer. Section III is composed of the remaining unreacted 8YSZ gas tight layer and again, in section IV, the anode functional layer can be seen.

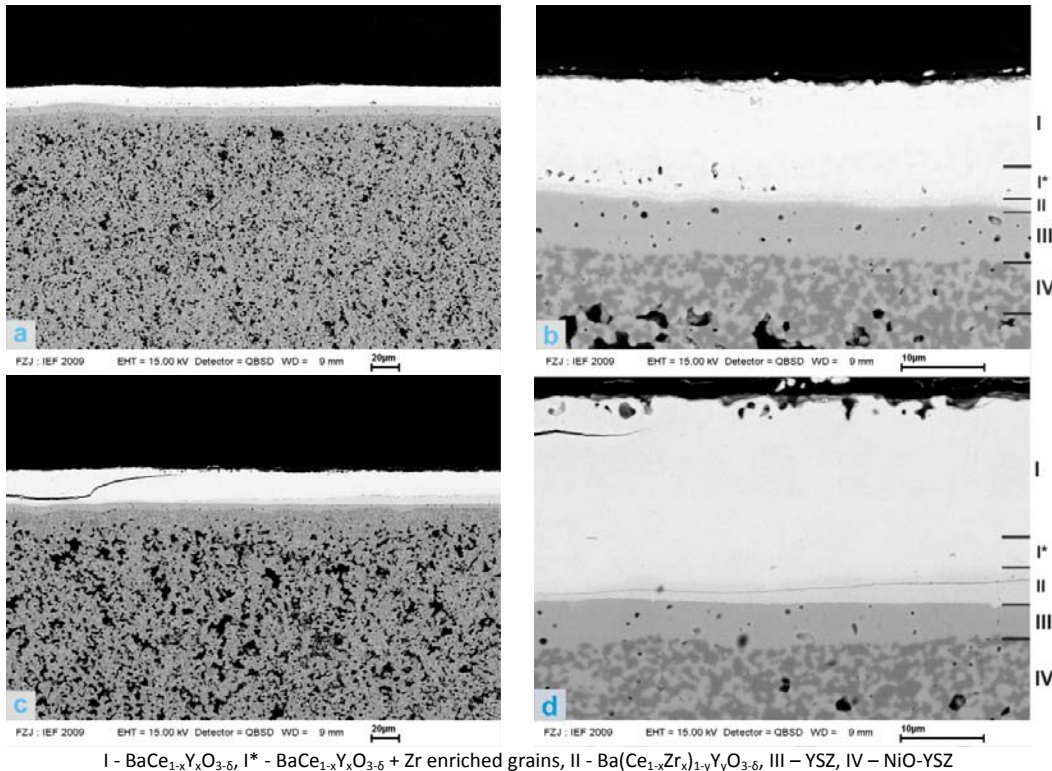


Figure 38: SEM micrographs of samples: (a-b) BCY10-2020-YSZ and (c-d) BCY10-2040-YSZ

It is clear from both samples that the barium carbonate layers do react with the yttria doped ceria layer to form a dense layer. There are some noticeable cracks in both samples, which were likely caused when the samples were fractured (for cross-sectioning) before polishing. In both cases, the reaction continues into the yttria stabilized zirconia layer with the reaction going further into the sample with the thicker barium carbonate layer. The tolerance factors calculated for BaCeO₃ and BaZrO₃ were 0.94 and 1.00, respectively. The tolerance factors of

both perovskite structures are clearly high enough that the BaO reacts readily with both the doped ceria and zirconia. XRD analysis of the BCY10-2020-YSZ sample is shown in Figure 39 and it can be noted that no detectable amounts of BaCO₃ or BaO were found leading one to believe that all of the available Ba was used for reaction with either the yttria-doped ceria or zirconia (both of which were detected on the surface). Adjustment of layer thickness could result in better stoichiometry and less extra reaction with excess BaO. It is interesting to note that sintering temperatures of 1500-1715°C for up to 30 h are normally required for near theoretically dense barium zirconate bars and pellets [17,20,73–75]. Dense layers seem to appear upon reaction of the layers at 1400°C for 10 h which is substantially less than the maximum temperatures used by other authors. Given the reactivity of BaO in this application, it is likely that reaction temperatures could be further reduced and should be studied in further research.

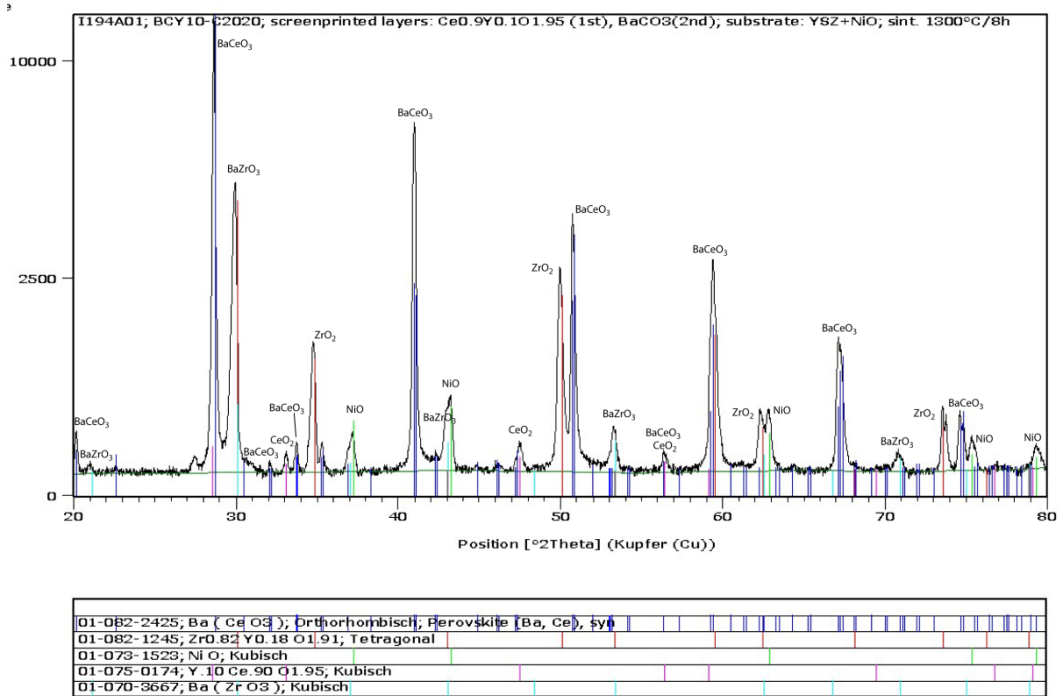


Figure 39: XRD analysis of the surface of sample BCY10-2020-YSZ

5.3.2.3 Strontium Carbonate Second Layer

Figure 40 shows the top-view photographs of samples (a) SCY10-2020-YSZ and (b) SCY10-2040-YSZ. Unlike the BCY10 samples, the two different carbonate thicknesses did not cause much visible difference between the two samples.

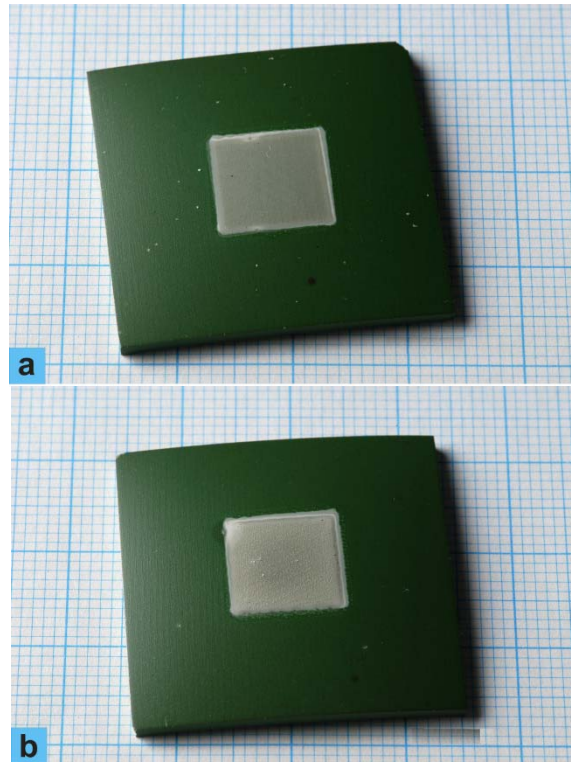


Figure 40: Photographs of samples: (a) SCY10-2020-YSZ and (b) SCY10-2040-YSZ

Figure 41 shows the SEM cross-sectional micrographs of the samples (a-b) SCY10-2020-YSZ and (c-d) SCY10-2040-YSZ. EDX analyses of samples SCY10-2020-YSZ (Figure 76) and SCY10-2040-YSZ (Figure 77) are found in Appendix I. Section I in both samples is likely primarily composed of yttria doped ceria. Section 1 in sample SCY10-2020-YSZ (Figure 41b) also showed small amounts of Zr present, but with only one visible phase. It was also separated from the next noticeable layer (II) by a highly porous region. Section 1 in sample SCY10-2040-YSZ (Figure 41d) did not show this porous detachment with section II, but showed two distinct phases; one composed only of yttria doped ceria (lighter

coloured phase) and the other composed of strontium, yttrium and oxygen with very little cerium present (darker phase). This second darker phase likely was a yttria doped strontium zirconate ($\text{SrZr}_{1-x}\text{Y}_x\text{O}_{3-\delta}$). Section II in both samples is a transition layer between section I and section III. In the case of SCY10-2020-YSZ, again only one phase is visible in this layer and is very porous. It does not contain any detectable Sr and is likely composed of an interdiffusion layer of yttria doped ceria from the layer above and yttria stabilized zirconia from the layer below. Section II in sample SCY10-2040-YSZ appears to be composed of two distinct phases each corresponding to an adjacent layer as opposed to the interdiffusion layer found in the SCY10-2020-YSZ sample. Section III in both samples corresponded to the original 8YSZ gas tight layer. In sample SCY10-2020-YSZ, this layer seemingly has two phases and is likely mostly composed of a yttria doped SrZrO_3 with some ceria enriched grains. Sample SCY10-2040-YSZ is composed of two distinct phases. The darker majority phase contains very little ceria and is likely again yttria doped SrZrO_3 . However, the lighter coloured regions seem to contain much more ceria and are much less grain-like. It is also interesting to note that the SrO continued to react with the NiO-8YSZ in the anode functional layer (section IV) of both samples and that ceria enriched regions are found as well.

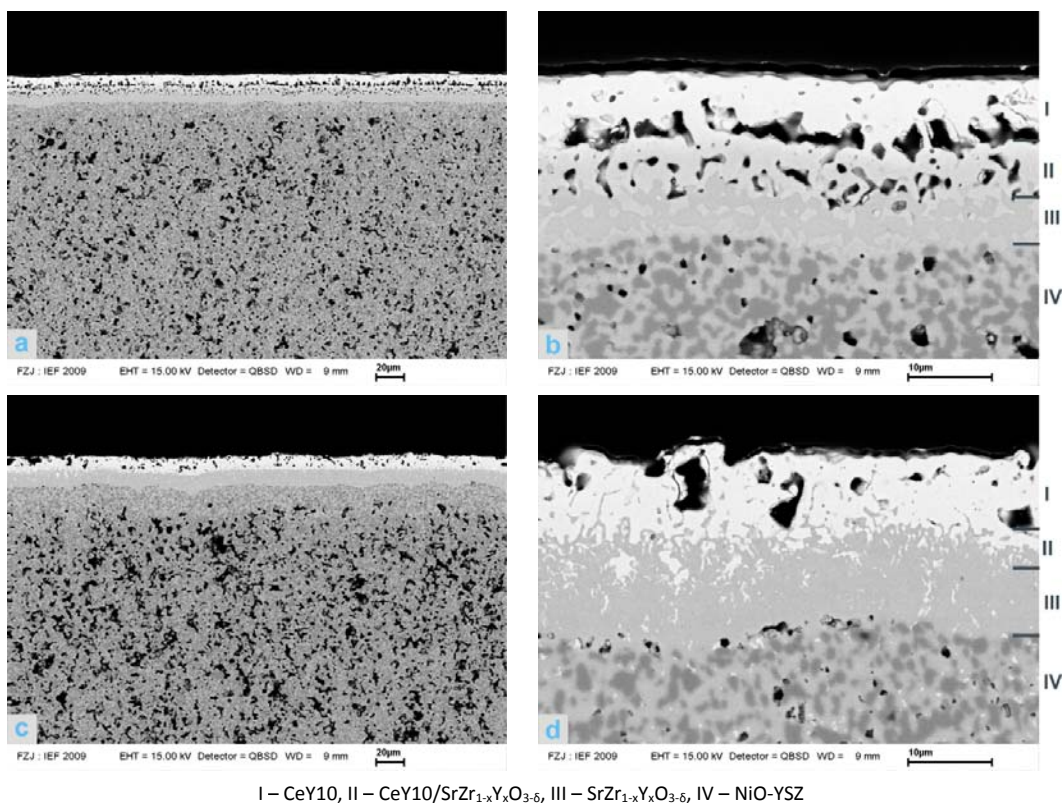


Figure 41: SEM micrographs of samples: (a-b) SCY10-2020-YSZ and (c-d) SCY10-2040-YSZ

It is obvious that the layered reaction of strontium carbonate with yttria doped ceria did not result in dense layers of yttria doped SrCeO₃ as intended. The strontium carbonate layers in both samples seemed to bypass the yttria doped ceria layer and more selectively react with the yttria stabilized zirconia to form SrZr_{1-x}Y_xO_{3-δ} which is consistent given that the perovskite tolerance factor for SrZrO₃ is calculated to be 0.95 compared with 0.88 for SrCeO₃. The SrO seems to continue its reaction through the 8YSZ gas tight layer and into the anode layers. Figure 42 shows the XRD surface analysis of the SCY10-2020-YSZ sample indicating that no detectable amounts of Sr were found. This leads one to believe that all of the strontium diffused and/or reacted with the 8YSZ and anode layers directly beneath the screen printed layers and not further out as in the BCY10 samples.

5.3.2.4 Calcium Carbonate Second Layer

Figure 43 shows the top-view photographs of (a) sample CCY10-2020-YSZ and (b) CCY10-2040-YSZ. A slightly darker colour is noticed in the sample with the thicker layer of carbonate (sample CCY10-2040-YSZ).

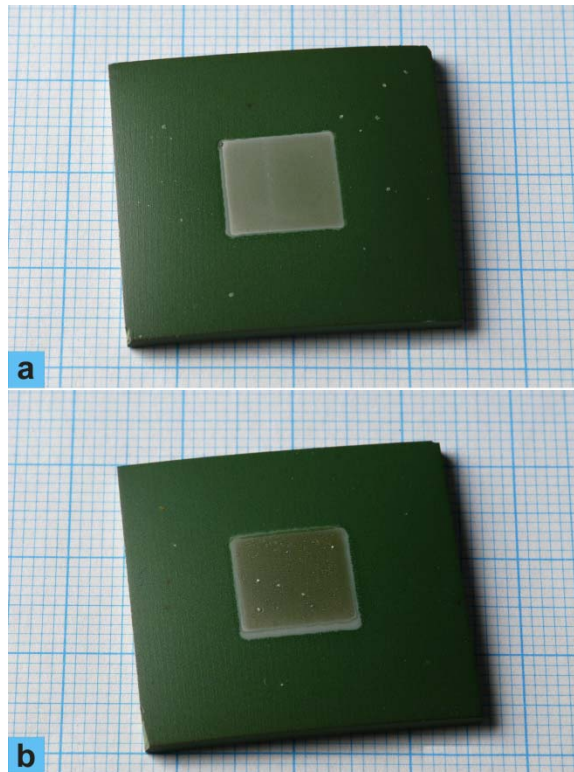


Figure 43: Photographs of samples: (a) CCY10-2020-YSZ and (b) CCY10-2040-YSZ

Figure 44 shows the SEM cross-sectional micrographs of the samples (a-b) CCY10-2020-YSZ and (c-d) CCY10-2040-YSZ. EDX analyses of samples CCY10-2020-YSZ (Figure 78) and CCY10-2040-YSZ (Figure 79) are found in Appendix I. Similar to the SCY10 samples, section I is comprised of primarily yttria doped ceria with a small amount of Zr detected in the CCY10-2020-YSZ sample (Figure 44b). Section II in both samples is composed mainly of 8YSZ with small amounts of Ce and Ca also present. Section III is composed primarily of what are most likely yttria doped CaZrO_3 grains (darker) and grains with compositions similar to

those found in section II (lighter). With more CaO available for reaction with 8YSZ, section III in sample CCY10-2040-YSZ is denser and contains much more yttria doped CaZrO_3 than in sample CCY10-2020-YSZ even though some small grains containing mostly 8YSZ are still present. Calcium and cerium were detected in section IV of both samples suggesting an extended diffusion zone into the substrate which is similar to what was found in the SCY10 samples.

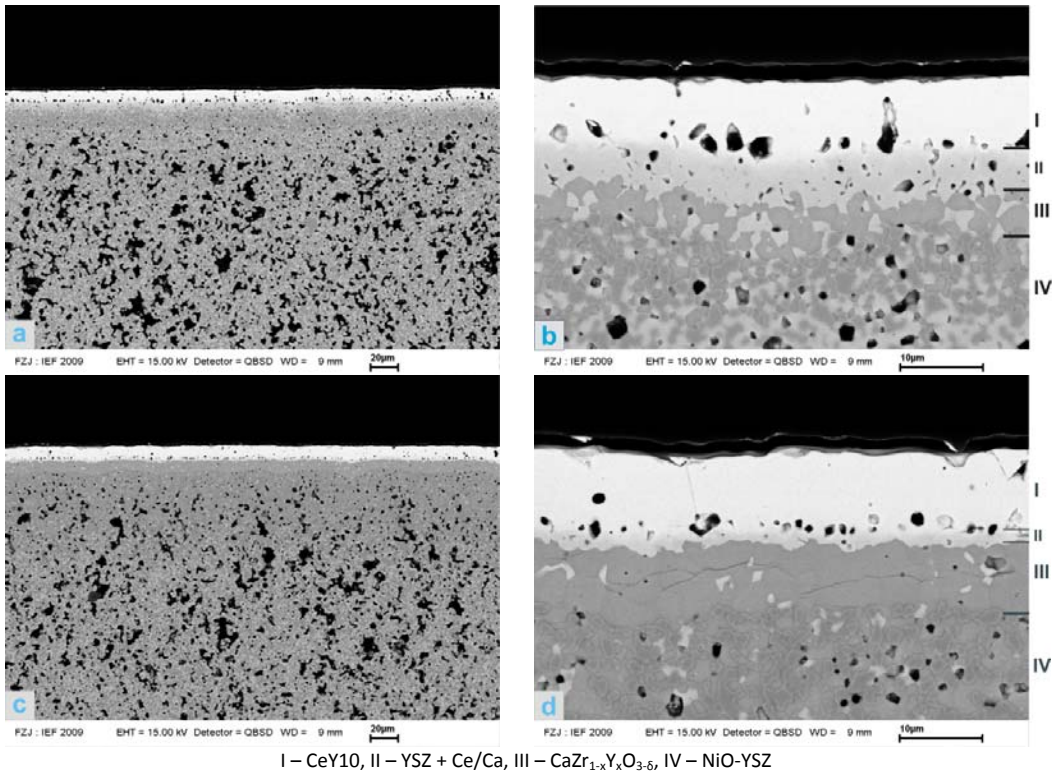


Figure 44: SEM micrographs of samples: (a-b) CCY10-2020-YSZ and (c-d) CCY10-2040-YSZ

Again it can be seen that the CaO selectively reacted with the 8YSZ instead of the yttria doped ceria and again this may be explained by the perovskite tolerance factor for CaZrO_3 (0.91) being larger than that of CaCeO_3 (0.85). Figure 45 shows XRD surface analysis of the CCY10-2020-YSZ sample and very similar to the SCY10-2020-YSZ sample, no detectable amount of Ca was detected on the surface. Again this could mean that all of the Ca diffused and/or reacted downwards directly under the screen printed layers.

5.3.3 CGO-NiO Substrates

The NiO-CGO substrates were 20 x 20 mm² (1.5 mm thick) and were composed of a NiO-CGO cermet with a surface smoothing interlayer of the same composition (anode functional layer) as well as a screen printed and final sintered (1400°C) gas tight electrolyte layer of CGO. An SEM cross-section of a NiO-CGO substrate with the different layers labeled is shown in Figure 46.

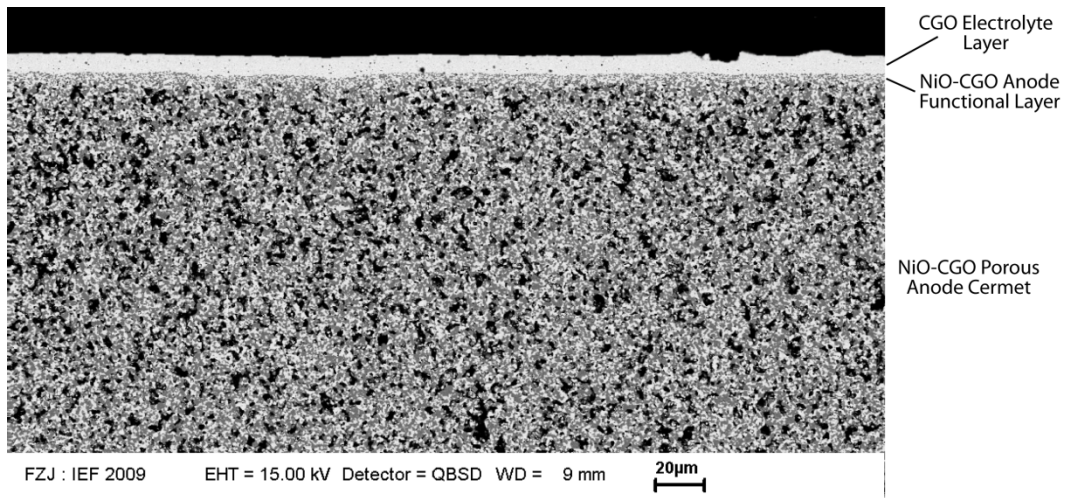


Figure 46: SEM cross-section of a NiO-8YSZ substrate.

The screen printed samples and their compositions and synthesis conditions can be seen in Table 11.

Table 11: Screen printed samples on NiO-CGO substrates

Sample	Substrate		Layers					
			First			Second		
	Type	Temp.	Type	Thick.	Temp.	Type	Thick.	Temp.
BCY10-2020-CGO	NiO-CGO	1400°C	Ce _{0.90} Y _{0.10} O _{1.95}	20 μm	1300°C	BaCO ₃	20 μm	1300°C
BCY10-2040-CGO	NiO-CGO	1400°C	Ce _{0.90} Y _{0.10} O _{1.95}	20 μm	1300°C	BaCO ₃	40 μm	1300°C
SCY10-2020-CGO	NiO-CGO	1400°C	Ce _{0.90} Y _{0.10} O _{1.95}	20 μm	1300°C	SrCO ₃	20 μm	1400°C
SCY10-2040-CGO	NiO-CGO	1400°C	Ce _{0.90} Y _{0.10} O _{1.95}	20 μm	1300°C	SrCO ₃	40 μm	1400°C
CCY10-2020-CGO	NiO-CGO	1400°C	Ce _{0.90} Y _{0.10} O _{1.95}	20 μm	1300°C	CaCO ₃	20 μm	1400°C
CCY10-2040-CGO	NiO-CGO	1400°C	Ce _{0.90} Y _{0.10} O _{1.95}	20 μm	1300°C	CaCO ₃	40 μm	1400°C

5.3.3.1 Doped Ceria Layer

A top-view photograph of the sintered CeY10 first layer on the NiO-CGO substrate is shown in Figure 47, while SEM cross-sectional micrographs are shown in Figure 48. EDX analysis is shown in Figure 80 (Appendix I). The layer was prepared with a wet thickness of approximately 20 μm . The SEM images again clearly show a distinct additional layer on top of the original substrate layers. The top layer (I) corresponds to the screen printed CeY10 and, similar to the NiO-8YSZ substrate, the layer is very porous but with a fairly uniform thickness. Again, the layer being sintered under constraint could be the reason for the limited densification [72]. The second layer (II) is the gas tight CGO layer which rests on top of the functional anode layer (III) composed of NiO and CGO grains.

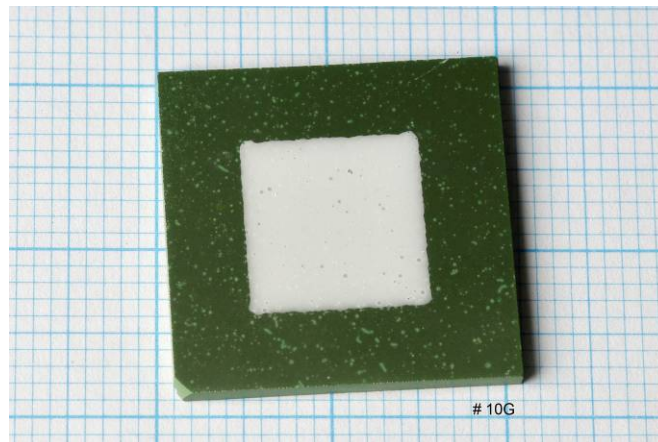


Figure 47: Sintered CeY10 first layer on CGO-NiO substrate

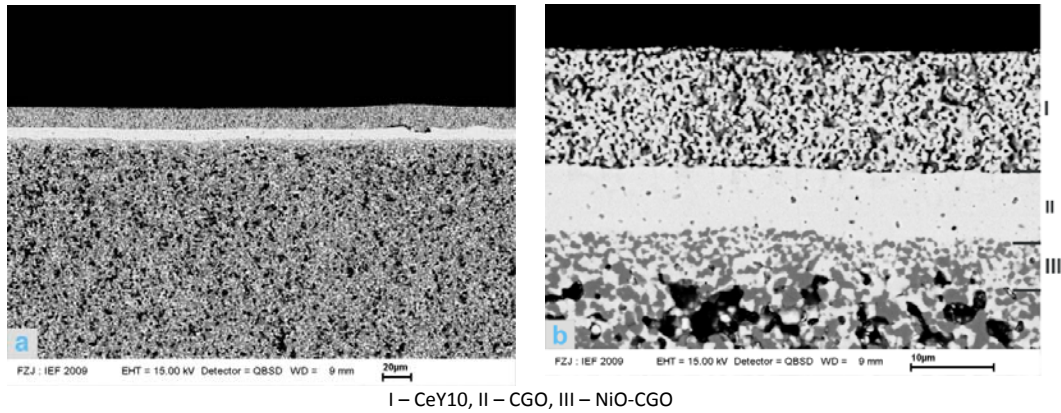


Figure 48: SEM cross-sections of sintered CeY10 first layer on NiO-CGO substrate

5.3.3.2 Barium Carbonate Second Layer

Figure 49 shows the top-view photographs of samples (a) BCY10-2020-CGO and (b) BCY10-2040-CGO. Again, more surface defects and an extended reaction zone are noticed with the thicker BaCO_3 layer in sample BCY10-2040-CGO.

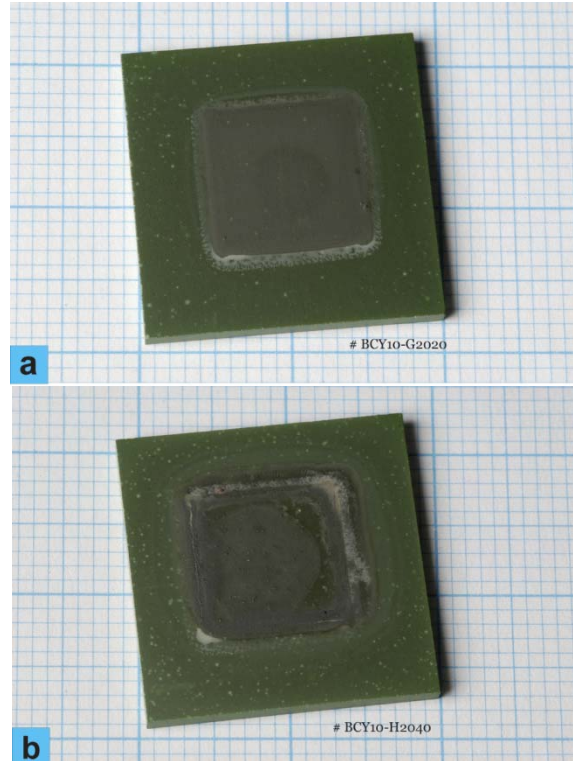


Figure 49: Photographs of samples: (a) BCY10-2020-CGO and (b) BCY10-2040-CGO

Figure 50 shows the SEM cross-sectional micrographs of (a-b) sample BCY10-2020-CGO and (c-d) sample BCY10-2040-CGO. EDX analyses of samples BCY10-2020-CGO (Figure 81) and BCY10-2040-CGO (Figure 82) are found in Appendix I. Layer I in sample BCY10-2020-CGO is composed of a barium cerate primarily doped with yttrium, but with some gadolinium present near the boundary with layer II. This is likely due to the BaO beginning to react with the CGO electrolyte layer as well as Gd diffusion into the upper layer. Layer II is what remains of the CGO layer with some yttrium being present in the ceria matrix near the top due to diffusion from the upper layer. Layer III is the functional anode layer of the NiO-CGO substrates. Sample BCY10-2040-CGO is very similar, but with the additional BaO provided by the thicker BaCO₃ layer, the reaction clearly continues well into the CGO layer. Again, layer I is likely composed of a doped barium cerate with yttrium as the primary dopant starting at the top and moving towards being completely gadolinium doped near the border with layer II. Layer II is again composed of CGO with some yttrium being present near the border with layer I. It can be noticed that the remaining CGO layer in sample BCY10-2040-CGO is thinner than in sample BCY10-2020-CGO and this is due to the increased amount of BaO available for reaction.

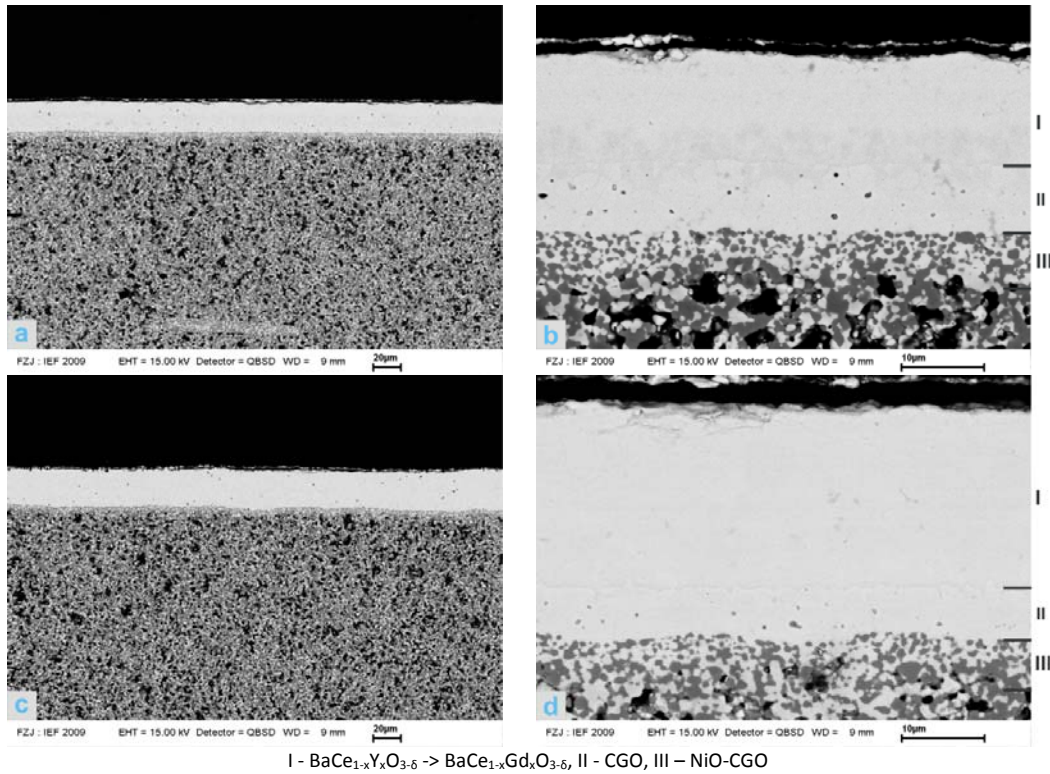


Figure 50: SEM micrographs of samples: (a-b) BCY10-2020-CGO and (c-d) BCY10-2040-CGO

Figure 51 shows an XRD surface analysis of the BCY10-2020-CGO sample. Only barium cerate and gadolinia doped ceria were detected meaning all of the barium carbonate either reacted or diffused into the substrate. Since the substrate is composed of a doped ceria ($\text{Ce}_{0.80}\text{Gd}_{0.20}\text{O}_{1.90}$), it is difficult to determine whether or not some unreacted CeY10 remained. However, as the BCY10-2020-YSZ sample contained some unreacted CeY10, it is likely that the BCY10-2020-CGO sample did as well.

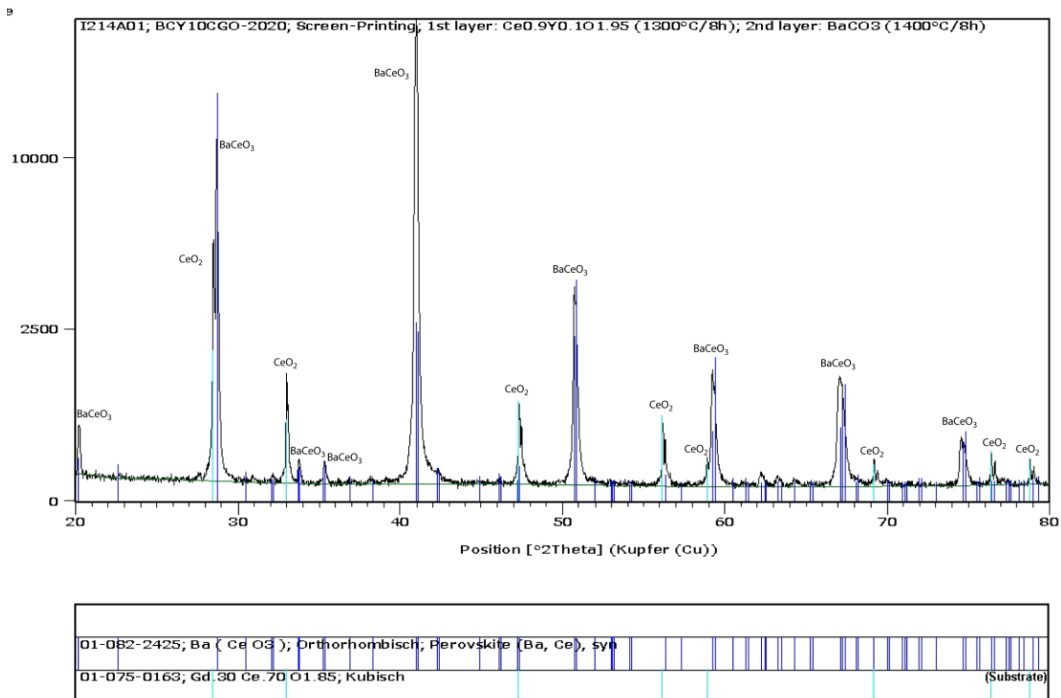


Figure 51: XRD analysis of the surface of sample BCY10-2020-CGO

Dense barium cerate layers are clearly present in both BCY10 samples. It is likely that with enough BaO available for reaction, the reaction would continue into the CGO layer and fully transform it into a gadolinia-doped barium cerate. This method of synthesis seems to work very well for reacting BaCO₃ with a doped ceria layer to create a dense perovskite layer. Thinner layers would likely be possible and would just require the adjustment of initial layer thicknesses.

5.3.3.3 Strontium Carbonate Second Layer

Figure 52 shows top-view photographs of samples (a) SCY10-2020-CGO and (b) SCY10-2040-CGO. The layer in sample SCY10-2040-CGO is slightly darker in colour and less uniform in appearance probably due to an excess amount of SrO present during reaction.

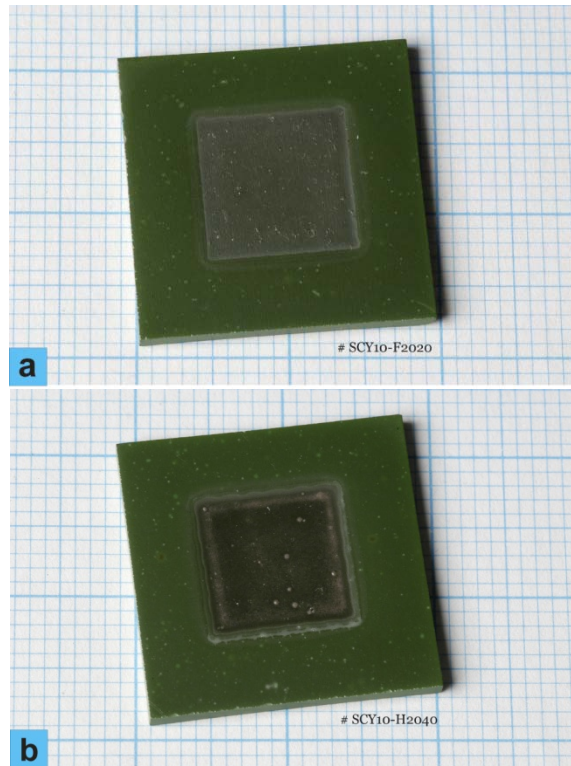


Figure 52: Photographs of samples: (a) SCY10-2020-CGO and (b) SCY10-2040-CGO

Figure 53 shows the SEM cross-sectional micrographs of (a-b) sample SCY10-2020-CGO and (c-d) sample SCY10-2040-CGO. EDX analyses of samples SCY10-2020-CGO (Figure 83) and SCY10-2040-CGO (Figure 84) are found in Appendix I. In sample SCY10-2020-CGO, three different regions are noticed. The top layer (I) is mainly composed of $\text{SrCe}_{1-x}\text{Y}_x\text{O}_{3-\delta}$ with the x value very close to 0.10 as well as some remaining unreacted CeY10 grains. Section II is the remaining CGO electrolyte layer. Some Sr and Y are detected in this CGO layer and likely diffused from the upper layer. Section III is the functional anode layer of the substrate composed of NiO and CGO grains. Sample SCY10-2040 shows a much extended reaction zone as more SrO was available for reaction. The perovskite reaction clearly moves right into the CGO layer resulting in a thicker layer (I) with a perovskite structure going from mostly yttrium doped to mostly gadolinium doped at the bottom with some unreacted CeY10 and CGO grains still present. Interestingly, the reaction results look very different to those of the SrCO_3

second layer on the NiO-8YSZ substrates. Here we see a reaction front that progresses downwards through the CeY10 and CGO layers resulting in a dense layer of predominately strontium cerate.

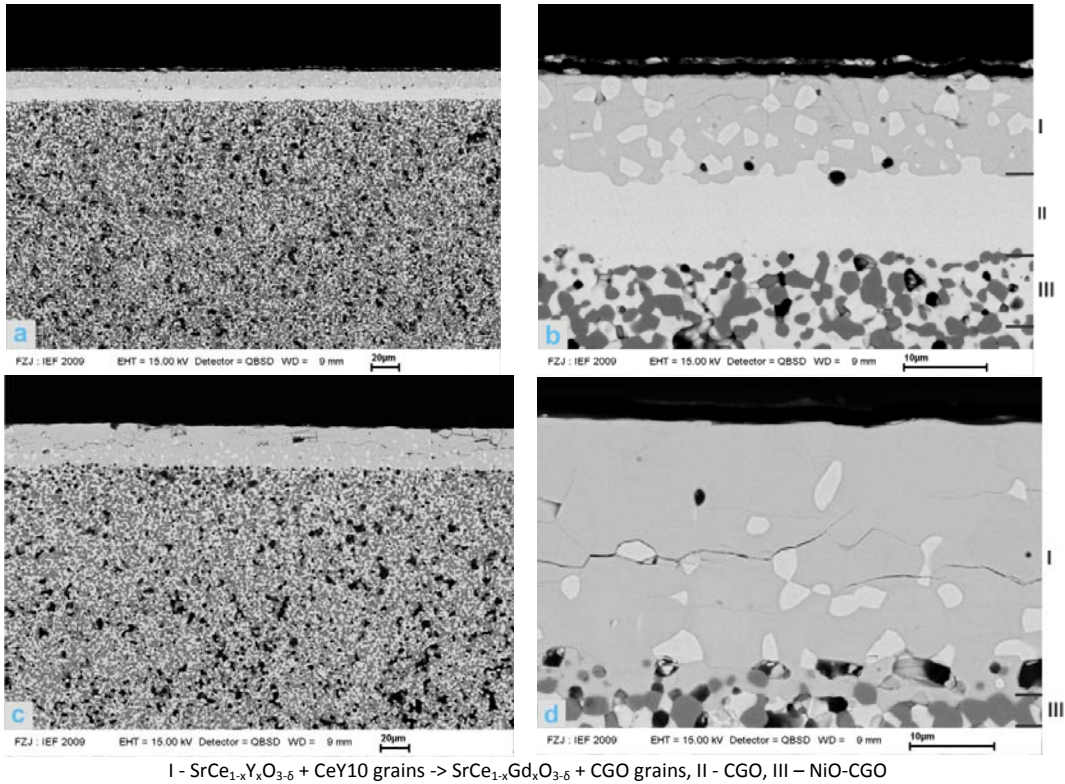


Figure 53: SEM micrographs of samples: (a-b) SCY10-2020-CGO and (c-d) SCY10-2040-CGO

Figure 54 shows an XRD surface analysis of sample SCY10-2020-CGO. Similar to the SCY10-2020-YSZ sample, no strontium carbonate was detected. Only perovskite (strontium cerate) and gadolinia doped ceria were detected and it can be assumed that all of the SrO formed was either reacted with the CeY10 layer or the CGO substrate.

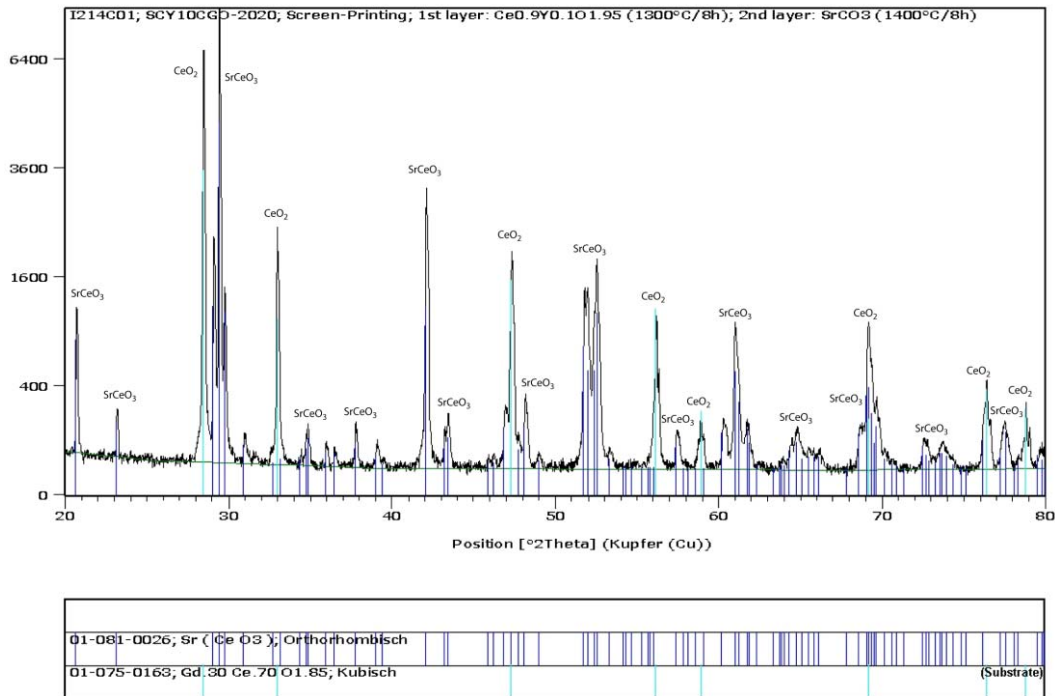


Figure 54: XRD analysis of the surface of sample SCY10-2020-CGO

Dense layers were produced in both of the samples which seemed to contain both Y and Gd doped strontium cerate as well as unreacted CeY10 and CGO grains. It is possible that the unreacted grains would disappear if enough SrO was available for reaction. Increasing the top SrCO₃ layer thickness would likely achieve this and result in a single phase strontium cerate based layer. It is also possible that a higher reaction temperature or a longer reaction time could also lead to a more complete reaction and a single phase strontium cerate based layer. Hence this could be a viable method for producing strontium cerate layers.

5.3.3.4 Calcium Carbonate Second Layer

Figure 55 shows the top-view photographs of samples (a) CCY10-2020-CGO and (b) CCY10-2040-CGO. The samples are very different in appearance and clearly the thickness of the carbonate layer was the cause. In sample CCY10-2040-CGO,

surface defects are noticed as well as some agglomerate particles which are most likely from the CaCO_3 paste.

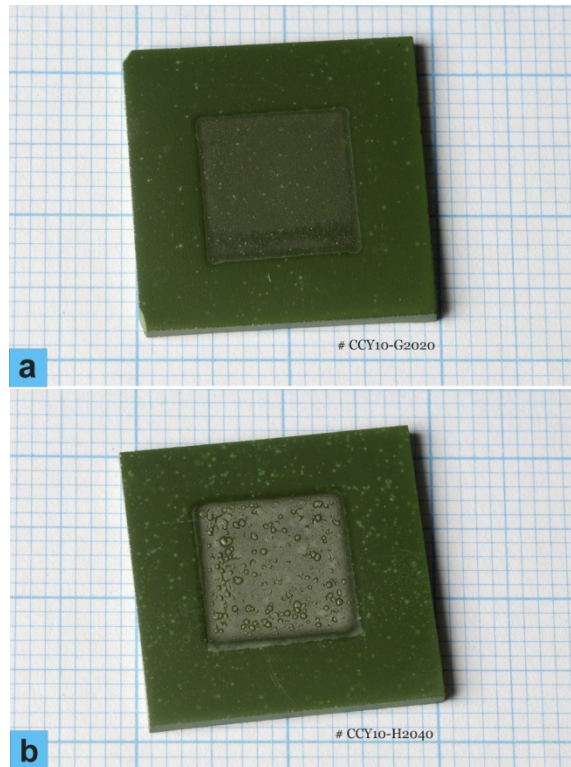


Figure 55: Photographs of samples: (a) CCY10-2020-CGO and (b) CCY10-2040-CGO

Figure 56 shows the SEM cross-sectional micrographs of (a-b) sample CCY10-2020-CGO and (c-d) sample CCY10-2040-CGO. EDX analyses of samples CCY10-2020-CGO (Figure 85) and CCY10-2040-CGO (Figure 86) are found in Appendix I. It is clearly seen in both samples that a very dense layer was formed on top of the porous substrate. Section I in both samples is composed of mainly of CeY10 with some Gd and Ca being detected. Similarly, section II in both samples is composed of mainly CGO with some Y and Ca being detected. Some grains are noticed where Y is not detected and these are composed of almost exclusively CGO with some Ca present. Finally, section III again corresponds to the

functional anode layer and is composed of NiO and CGO grains. It can be noticed that the layer in section I in sample CCY10-2040-CGO is slightly thinner than in sample CCY10-2020-CGO which is contrary to what one may have thought. A similar trend is noticed in the CCY10 samples on the NiO-8YSZ substrates (Figure 44), but this is perhaps due only to the location where the SEM photo was taken as further investigation revealed that on average the layers were very similar in thickness.

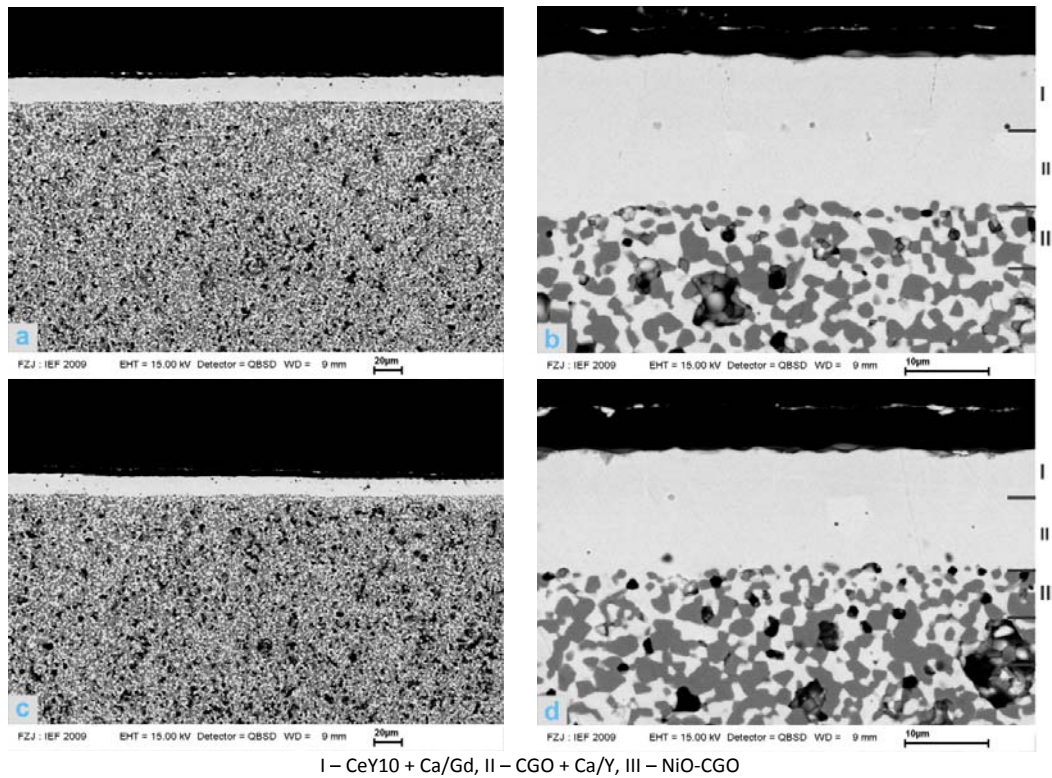


Figure 56: SEM micrographs of samples: (a-b) CCY10-2020-CGO and (c-d) CCY10-2040-CGO

Figure 57 shows XRD surface analysis of sample CCY10-2020-CGO. Calcium oxide and ceria were detected in addition to the CGO and NiO from the substrate. This shows that there was likely very limited reaction between the calcium carbonate and CeY10 layers.

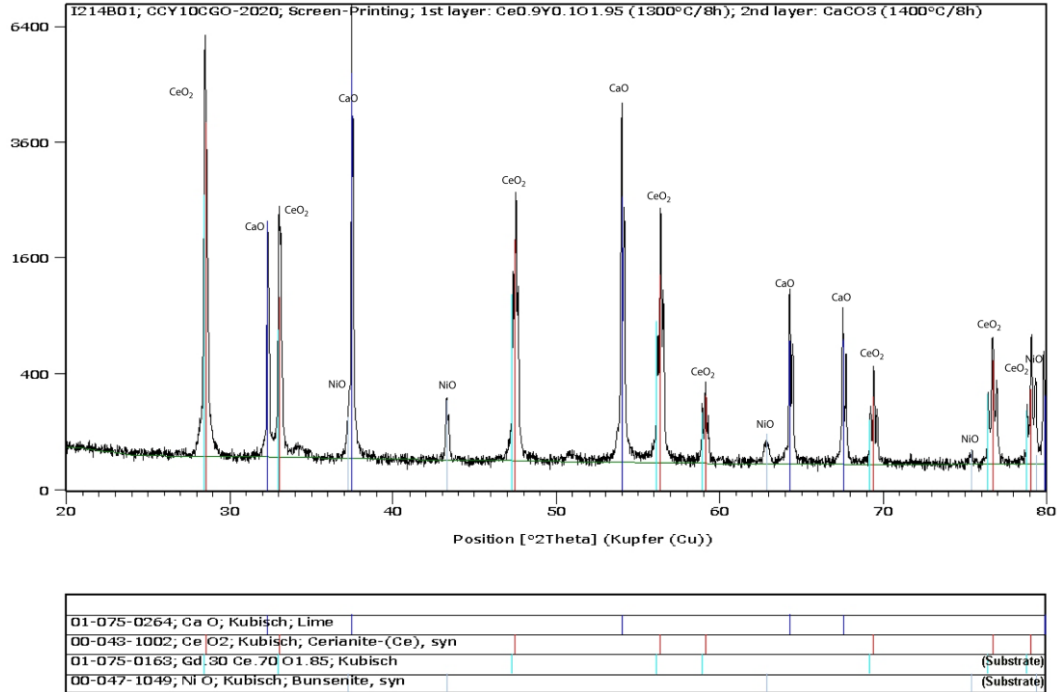


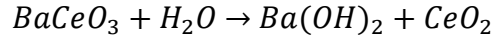
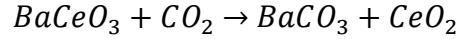
Figure 57: XRD analysis of the surface of sample CCY10-2020-CGO

Although a dense layer was produced, it is believed that a calcium cerate was not formed in these samples. Given the relative weak intensities of the Ca peaks, it is more likely that these layers are still primarily composed of a doped cerate structure. Earlier work has shown that it is possible for Ca to act as a dopant on the B-site of a barium cerate [8]. Perhaps the Ca detected is diffusing into the CeY10 and CGO fluorite structures in a similar manner and replacing some of the Ce. This would result in a composition similar to $Ce_{1-x-y-z}Ca_xY_yGd_zO_{2-\delta}$ with the Y content decreasing from top to bottom and the Gd content doing the opposite.

5.4 Doped Cerate-Zirconate Synthesis

The effect of changing the B-site aliovalent dopant was investigated by performing conductivity tests on five different compositions of doped barium cerate-zirconate, $BaCe_{0.5}Zr_{0.4}M_{0.1}O_{2.95}$, where M is the trivalent dopant cation. Zr

was doped into the B-site of the BaCeO₃ matrix to improve its chemical stability as it can react with CO₂ and H₂O according to the following reactions:



At the operational temperatures expected for the fuel cells (400-700°C), the reaction with H₂O is not significant and, therefore, the stability of the barium cerate-zirconate compounds is only limited in application by the reaction with CO₂ [12]. Katahira et al. [19] showed that the amount of Zr in BaCe_{0.5}Zr_{0.4}M_{0.1}O_{2.95}-based compounds was sufficient enough to inhibit the cerate decomposition reaction with CO₂. In their research, they show that the XRD patterns of their BaCe_{0.5}Zr_{0.4}Y_{0.1}O_{2.95} samples do not change from cubic perovskite after treatment in CO₂ at 900°C for 2 h, while samples with lower Zr content readily decompose. Since a Zr addition to barium cerates lowers the conductivity, the minimum Zr content to achieve sufficient stability was chosen (BaCe_{0.5}Zr_{0.4}M_{0.1}O_{2.95}) to be the basis for the dopant comparison study.

Gd is known to be one of the best dopants for barium cerates for high proton conduction and, similarly, Y is known to be one of the best for barium zirconates [11]. This is potentially a result of the differences in ionic radii between the dopants and their fit within the respective lattices (i.e. Gd³⁺ is closer in size to Ce⁴⁺ and Y³⁺ is closer in size to Zr⁴⁺). From Shannon's tables of ionic radii [77], the crystal (CR) and effective (IR) ionic radii of a number of relevant ionic species are shown in Table 12. The two types of radii only differ because of the use of a different value for the radius of the oxygen ion in the calculations.

Table 12: Ionic radii of selected relevant species

Ion	Coordination #	Crystal Ionic Radius (pm)	Effective Ionic Radius (pm)
Ba ²⁺	12	175	161
O ²⁻	8	128	142
Sr ²⁺	12	158	144
Ca ²⁺	12	148	134
Ce ⁴⁺	6	101	87
Nd ³⁺	6	112.3	98.3
Sm ³⁺	6	109.8	95.8
Eu ³⁺	6	108.7	94.7
Gd ³⁺	6	107.8	93.8
Tb ³⁺	6	106.3	92.3
Y ³⁺	6	104	90
Yb ³⁺	6	100.8	86.8
Sc ³⁺	6	88.5	74.5
Zr ⁴⁺	6	86	72

The dopants were chosen from literature examples so as to investigate the effect of different ionic radii on the properties of BaCe_{0.5}Zr_{0.4}M_{0.1}O_{2.95} and to find the most suitable trivalent dopant ion for this specific mixture of barium cerate and zirconate. The dopants chosen for investigation were: Nd, Eu, Gd, Y and Yb. The tolerance factors for the five compositions with these dopants are shown in Table 13. It can be seen in the table as well as in Figure 58 that the tolerance factor decreases as the ionic radius of the dopant increases.

Table 13: Perovskite tolerance factors for the barium cerate-zirconate compositions

Perovskite Composition	Tolerance Factor (CR)	Tolerance Factor (IR)
BaCe _{0.5} Zr _{0.4} Eu _{0.1} O ₃ (BCZEu)	0.957	0.957
BaCe _{0.5} Zr _{0.4} Gd _{0.1} O ₃ (BCZGd)	0.958	0.958
BaCe _{0.5} Zr _{0.4} Nd _{0.1} O ₃ (BCZNd)	0.956	0.956
BaCe _{0.5} Zr _{0.4} Y _{0.1} O ₃ (BCZY)	0.961	0.959
BaCe _{0.5} Zr _{0.4} Yb _{0.1} O ₃ (BCZYb)	0.959	0.961

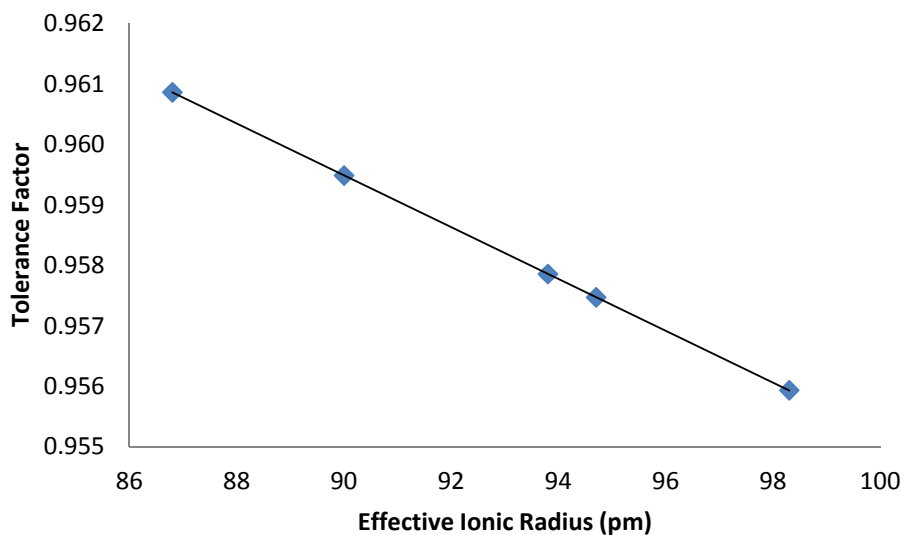


Figure 58: Plot of tolerance factor vs. dopant ionic radii for the barium cerate-zirconate compositions

5.4.1 Solid State Synthesis

The commercially obtained powders used for the solid state reaction can be seen in Table 1. The effect of solid state reaction temperature was first investigated with the BCZY composition. Figure 59 shows a plot of the XRD pattern from the BCZY precursor powders reacted at 1000°C for 10 h. It can be seen that the powder consists of two major phases, BaCeO₃ and BaZrO₃.

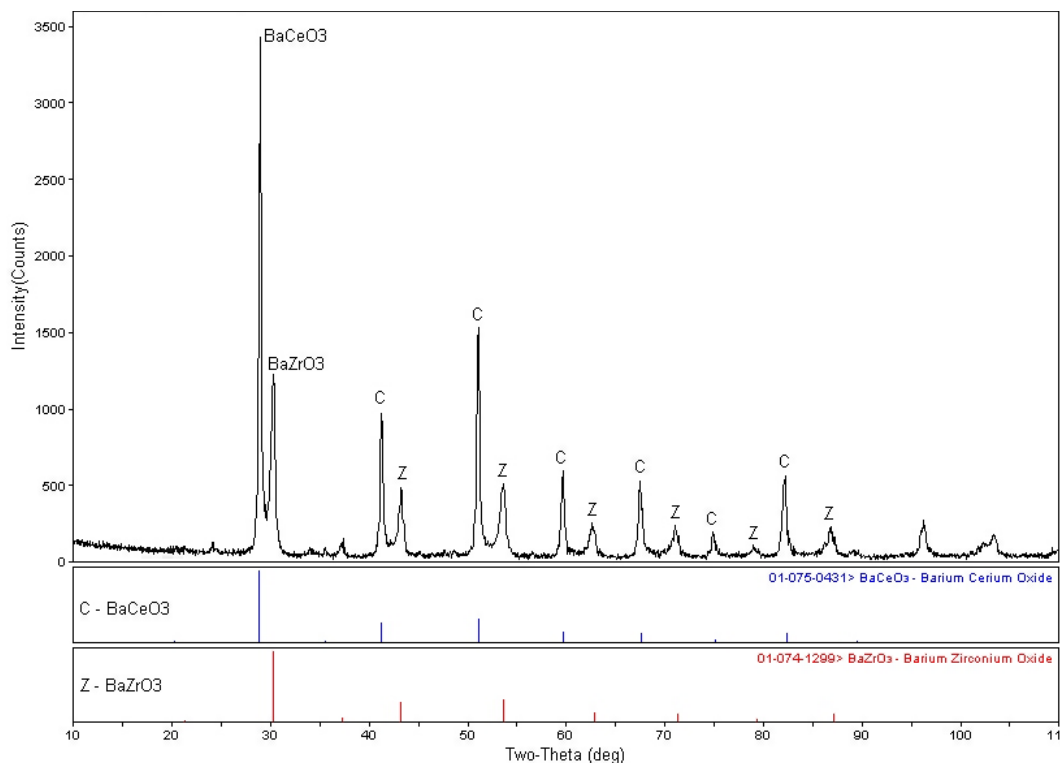


Figure 59: BCZY reacted at 1000°C

The BCZY precursor powders were reacted from 1000-1400°C for 10 h and the resulting XRD patterns can be seen in Figure 60. After the reaction at 1100°C, the resultant powder composition is very similar to the pattern at 1000°C in that it contains both cubic barium cerate and zirconate. Moving upwards to the 1200°C pattern, we still see the two previous phases, but begin to see them merging into a third phase: a combination of barium cerate and zirconate. At 1300°C, we see that this combination is nearly complete with the only major phase being that of cubic barium cerate-zirconate. Moving on, one can see that the powders reacted at 1400°C show only the fully combined single phase of barium cerate-zirconate. Clearly, for the formation of the BCZY composition, 1400°C for 10 h (or heat treatment Perovskite5 in Table 2) was sufficient. Starting with the heat treatment used for BCZY, a similar process was used to determine a sufficient solid state reaction procedure for the four other compositions. 1400°C for 10 h (heat treatment Perovskite5) was found to be

sufficient for BCZGd, but the final three compositions required slightly higher temperatures. BCZNd and BCZEu were found to only contain the single barium cerate-zirconate phase after 1450°C for 10 h (heat treatment Perovskite6) and, finally, BCZYb required 1500°C for 10 h (heat treatment Perovskite7). The XRD patterns for all the single phase reacted powder compositions can be seen in Figure 61. The patterns very closely match that of the cubic perovskite $\text{BaCe}_{0.4}\text{Zr}_{0.6}\text{O}_3$ from the pattern database.

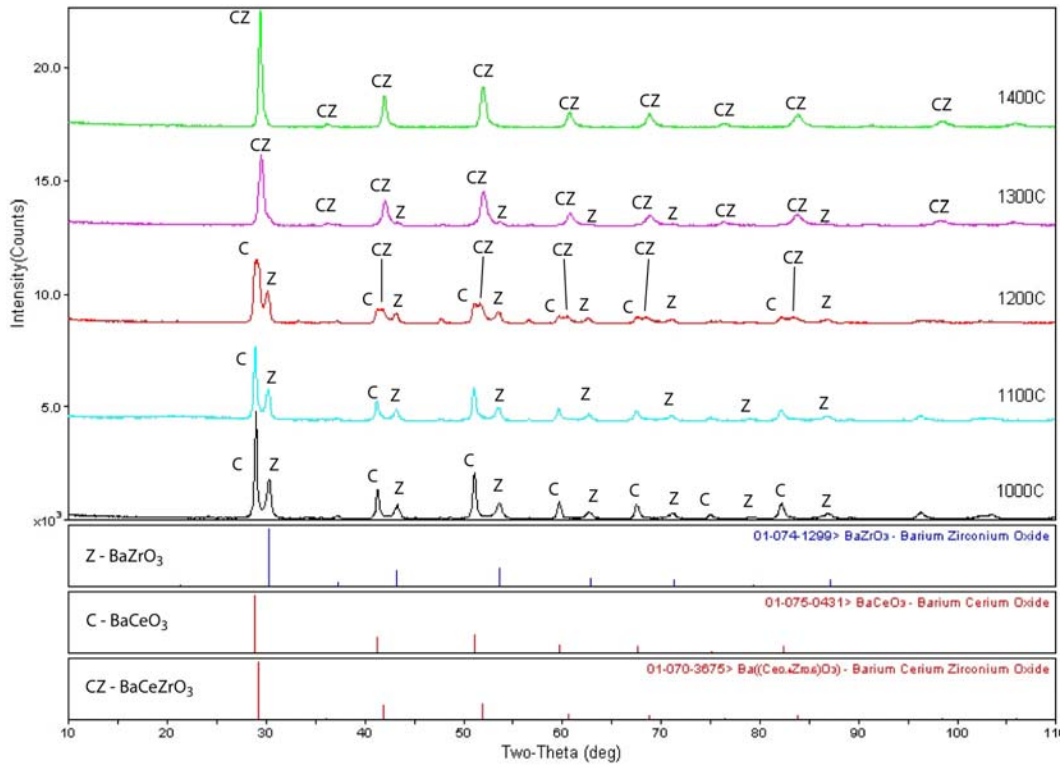


Figure 60: XRD patterns of BCZY precursor powders reacted at different temperatures

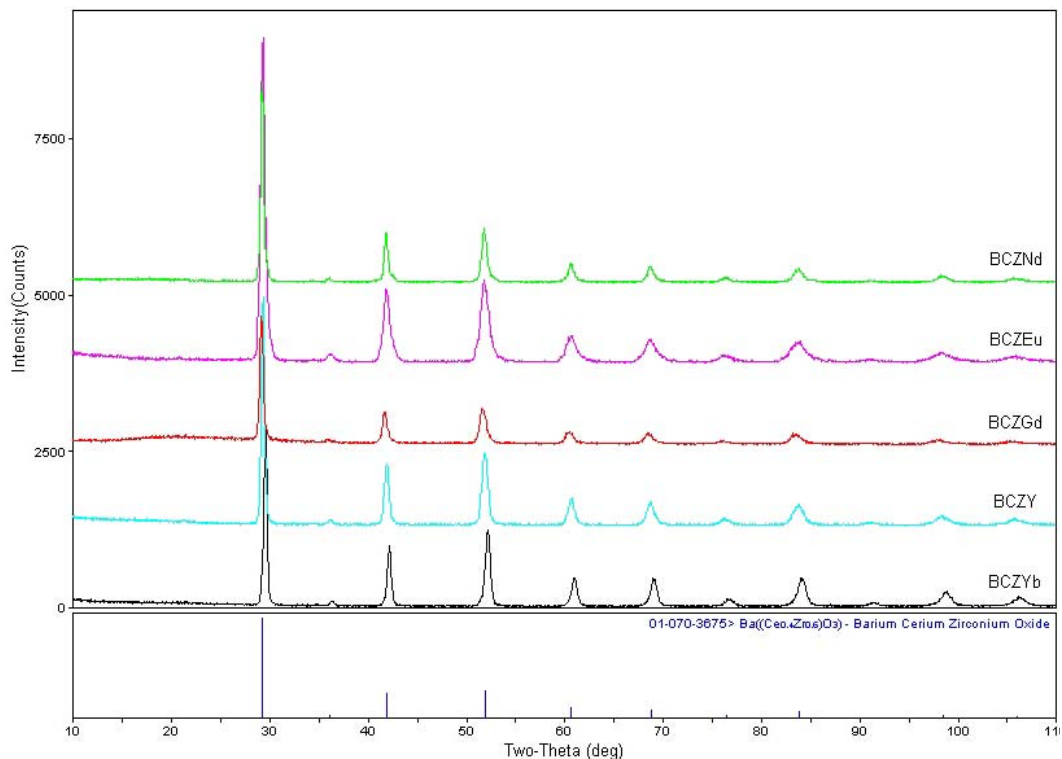


Figure 61: XRD patterns of all doped barium cerate-zirconate compositions

5.4.2 Powder Size Reduction

Initial tests were run involving the sintering of the BCZY powder into pellets to determine a pressing and sintering procedure. Initial sintered pellets were in the range of 67% of theoretical density even at the maximum temperature available for sintering, 1600°C (1650°C was available for the final BCZYb samples). It quickly became apparent that in order to achieve a high enough density, the powders would need to be modified. Since near maximum theoretical density was required in the final sintered pellets, the particle size of the powders needed to be reduced. For this purpose, a RETSCH PM100 planetary ball mill was used with colloidal or wet grinding. Powders were placed into polypropylene jars with ethanol and 5 mm zirconia milling balls that were placed into a custom made stainless steel metal housing that fit inside the ball mill. It was found that the

ratio of milling balls to powder to ethanol was very important for the final powder properties. Too much ethanol led to a smaller particle size reduction and less sinterability. Retsch recommends a solid to liquid ratio of 2:1 (vol. %) [78] and this was followed during subsequent ball millings. Retsch also shows that by using their planetary ball mills with the right parameters and equipment, particle sizes of less than 100 nm can be achieved [79]. However, using the setup described, the barium cerate-zirconate powders were found to have high enough sinterability (i.e., particle size low enough) after 24 h of milling at 500 rpm. The particle size analyses of the BCZYb before and after particle size reduction were carried out using two methods: the Fraunhofer method and a pseudo-Fraunhofer method. The plots of the particle size analyses for the Fraunhofer method can be seen in Figure 62 (before milling) and Figure 63 (after milling). The plots of the pseudo-Fraunhofer method can be seen for the unmilled powder in Figure 64 and in Figure 65 for the milled powder.

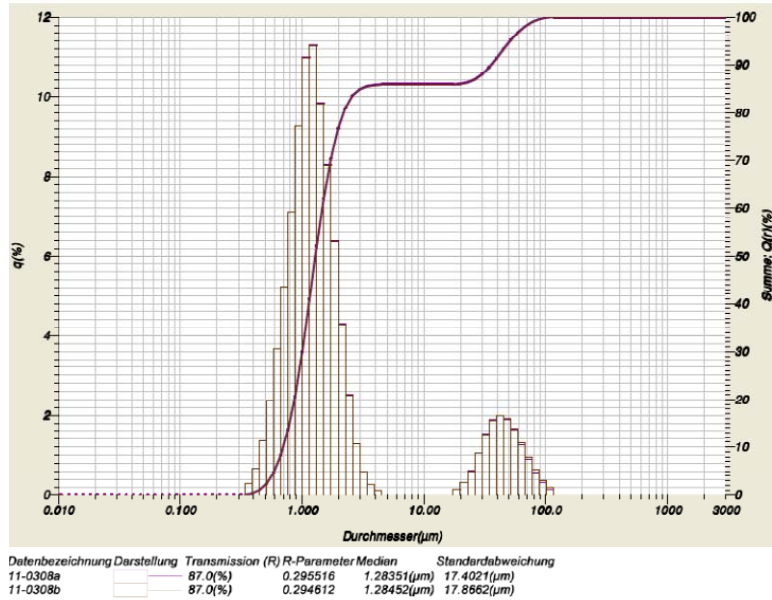


Figure 62: Particle size analysis of unmilled BCZYb powder (Fraunhofer method)

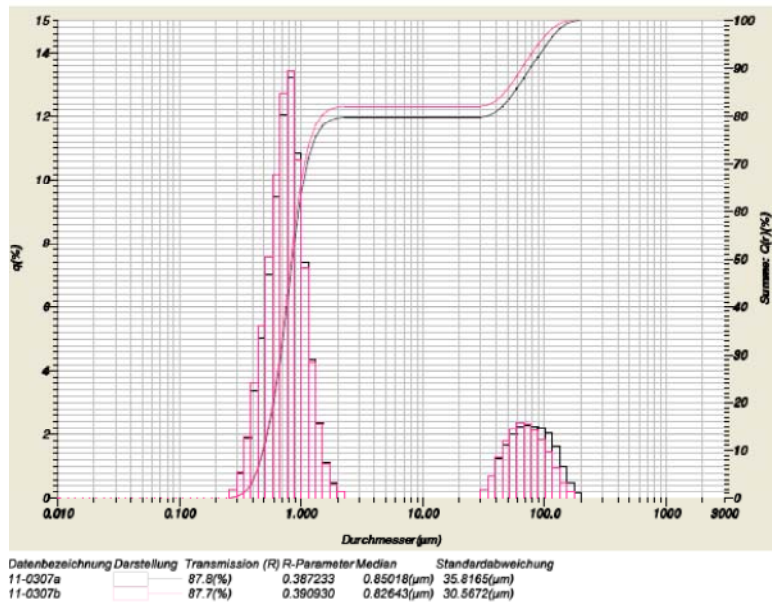


Figure 63: Particle size analysis of planetary ball milled BCZYb powder (Fraunhofer method)

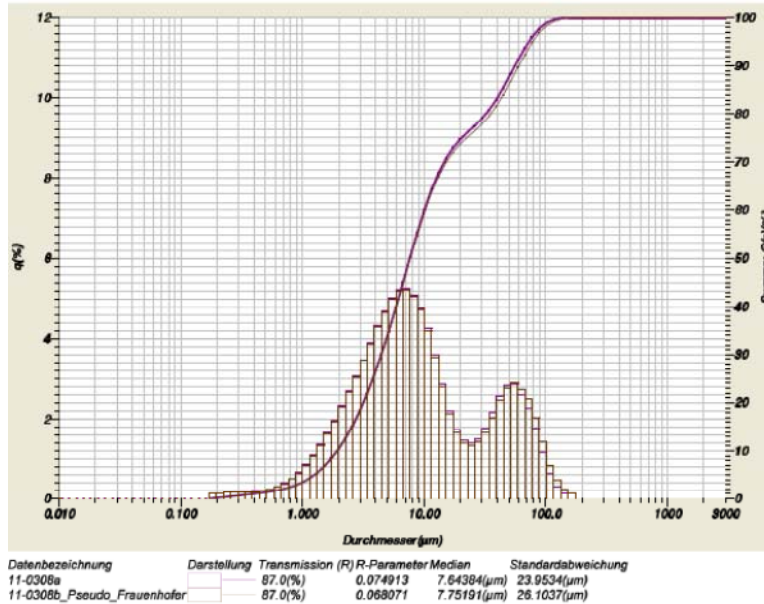


Figure 64: Particle size analysis of unmilled BCZYb powder (pseudo-Fraunhofer method)

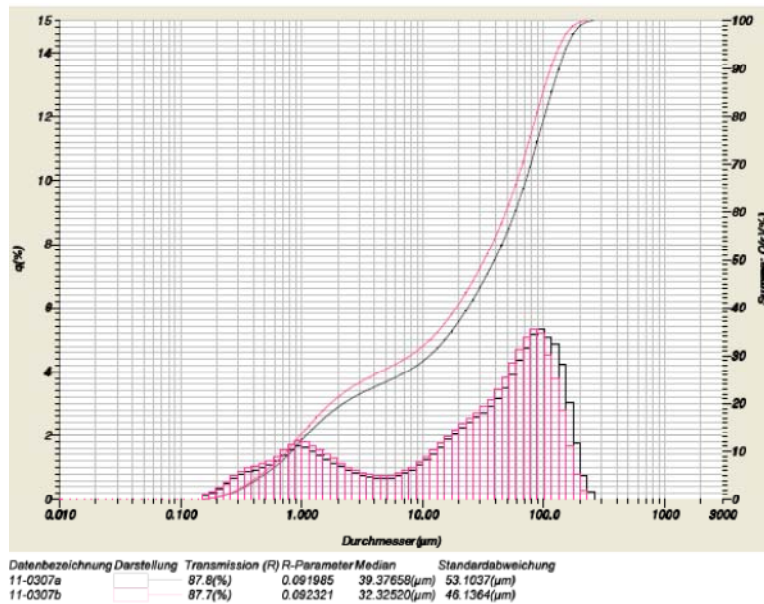


Figure 65: Particle size analysis of planetary ball milled BCZYb powder (pseudo-Fraunhofer method)

A clear difference in particle size distribution can be seen between the two methods and this may be an indication that the lower particle size limit ($\sim 1 \mu\text{m}$) is being reached. Regardless, the two methods both show that there is a particle size reduction in at least the smaller size fraction of particles. The larger

particles in the plots (i.e., around 100 μm) are likely indicative of some larger agglomerates. The real indicator that the particle size reduction step was successful was the effect it had on sinterability. The sintered pellets made from the non-planetary ball milled powders were only ~75% theoretically dense. However, after planetary ball milling for 24 h at 500 rpm with ethanol and 5 mm zirconia milling balls, densities of over 90% were obtained. Future work, however, should be targeted at using a commercial colloidal milling jar and multiple size stages of milling balls to achieve lower particle sizes and better results. At the high rotational speeds, the polypropylene jars were unable to withstand the forces that would have resulted from filling them to the recommendations of the planetary ball mill manufacturer, RETSCH. It is recommended that 60% of the volume of the milling jar be filled with milling balls [78] and the polypropylene jars were unable to maintain their seal at even a fraction of this amount.

5.4.3 Pellet Fabrication and Sintering

During the course of the initial pressing and sintering trials, it was found that a press mold lubricant would be beneficial to the pressing process. The pellets were difficult to smoothly extract and, therefore, often were cracked when they were removed. Ceramic particles tend to stick to the metal parts of the mold and make it difficult to remove and, therefore, a mold lubricant is beneficial [80]. Sheinin and Belostotskaya tested a variety of mold lubricants and coatings and found that satisfactory results were obtained by using a mixture of kerosene and stearine in a 2:1 ratio [80]. It was found that “stearine” referred to “stearin” and was either of the two closely related compounds, glyceryl tristearate or stearic acid. Both lubricants were mixed with odorless kerosene and tested as mold lubricants. Both mixtures needed to be heated to approximately 60°C before the white glyceryl tristearate or stearic acid solids homogenized with the kerosene into a clear mixture. After the heated mixtures were applied to the

metal molds using a cotton swab, the lubricant coatings were examined. The application of the glyceryl tristearate mixture resulted in a smooth homogenous coating that was ideal for mold lubrication. The coating made with the stearic acid mixture was not smooth or homogenous after application so the glyceryl tristearate mixture was used as a mold lubricant.

It was also observed during the pressing of the powders, that the mold used has a large effect on the pellet final properties. The initial 25.4 mm diameter mold used resulted in sintered pellets with lower density and circular cracking regardless of the procedure or heat treatment followed. However, the 6.35 mm ($\frac{1}{4}$ ") and 19.05 mm ($\frac{3}{4}$ ") molds used resulted in higher densities and better pellet properties. The pellets made with the smaller molds had a lower diameter to thickness ratio allowing pressure to be more evenly applied. The 19.05 mm ($\frac{3}{4}$ ") mold had a less exact fit (i.e., fractionally larger space between mold cylinder and housing) which may have allowed for air to escape more easily resulting in higher quality pressed samples.

To optimize the planetary ball milling, pressing and sintering parameters, 6.35 cm ($\frac{1}{4}$ ") pellets of BCZY were synthesized. In an attempt to achieve higher densities, the ramp rate of the 1600°C sintering treatment was tested at 1, 5 and 10 K/min. It was found that the ramp rate did not have a noticeable effect on final density and it was decided to use 5 K/min. It was found that pressing at 138 MPa (20000 psi) was sufficient to achieve high green densities. Best results were achieved by using lower pressure stages first and then moving up to 138 MPa (20000 psi). It was determined that 34.5 MPa (5000 psi) for one minute followed by 69 MPa (10000 psi) for another minute before raising the pressure to 138 MPa (20000 psi) and holding for two minutes produced high quality green samples. Care had to be taken during each stage of the pressing procedure as the pellets, themselves, were extremely fragile. For this reason, a binder (PVB)

and plasticizer (butyl benzyl phthalate) were added to the powders. This resulted in a substantially improved pressing process as green strength was greatly increased with an additional benefit of mold lubrication slightly improving. Most importantly, the binder and plasticizer additions to the powder did not result in a lower density in the final sintered product. An additional stage was added to the sintering procedures to volatilize or burn off the binder and plasticizer, and it was found that 500°C for one hour was sufficient for this purpose.

The largest effect on density was found to be temperature and the milling procedure used. Holding the sintering treatment constant (1600°C for 10 h), the duration of planetary ball milling, the rotational speed, and the powder to milling ball to ethanol ratio were adjusted. It was found that an approximate 2:1 weight ratio of powder to milling balls (maximum ~18 g of powder) and a ratio of ~1.4 mL ethanol per gram of powder could be used in the 120 mL polypropylene jars at 500 rpm for 24 h without loss of sealing in the jars.

Using the powders modified with this milling procedure, the binder and plasticizer, and the 1600°C sintering treatment, densities of >90% were achieved with all powders except for BCZYb. After sintering at 1650°C for 10 h (heat treatment Sinter3 in Table 2), densities greater than 90% were achieved in the BCZYb samples. The lower sinterability of the BCZYb powder could be due to its higher solid state reaction temperature of 1500°C which could have resulted in a larger initial particle and grain size.

The synthesis parameters and densities of the final samples intended for conductivity testing are shown in Table 14. After sintering at 1600°C, the BCZYb samples only reached ~85% of theoretical density, while the samples sintered at 1650° were over 90% theoretically dense. It can be seen from the densities that

there is some variability, but both measurement methods seem to support that the densities of the samples intended for conductivity testing were indeed greater than 90%.

Table 14: Synthesis methods and densities of final sintered samples for conductivity measurements

Sample	Manufacturing Method	Sintering Temperature	Densities		
			Approx. Green (% of theor.)	Geometric (% of theor.)	Archimedes (% of theor.)
BCZY_FS_6	Hand Press, 6.35 mm (¼") Mold	1600°C (Sinter2)	52%	91%	97%
BCZY_FS_8	Hand Press, 6.35 mm (¼") Mold	1600°C (Sinter2)	50%	91.5%	97%
BCZY_FS_9	Hand Press, 6.35 mm (¼") Mold	1600°C (Sinter2)	52.5%	93%	86.5%
BCZEu_FS_1	Hand Press, 6.35 mm (¼") Mold	1600°C (Sinter2)	58%	93%	97.5%
BCZEu_FS_3	Hand Press, 6.35 mm (¼") Mold	1600°C (Sinter2)	55%	94.5%	97.5%
BCZEu_FS_5	Hand Press, 6.35 mm (¼") Mold	1600°C (Sinter2)	54.5%	92.5%	96.5%
BCZNd_FS_1	Hand Press, 6.35 mm (¼") Mold	1600°C (Sinter2)	57%	91%	92%
BCZNd_FS_2	Hand Press, 6.35 mm (¼") Mold	1600°C (Sinter2)	54%	97%	97%
BCZNd_FS_3	Hand Press, 6.35 mm (¼") Mold	1600°C (Sinter2)	53%	93%	93%
BCZGd_FS_11	Hand Press, 6.35 mm (¼") Mold	1600°C (Sinter2)	55%	94%	97%
BCZGd_FS_13	Hand Press, 6.35 mm (¼") Mold	1600°C (Sinter2)	55%	94%	97%
BCZGd_FS_14	Hand Press, 6.35 mm (¼") Mold	1600°C (Sinter2)	54%	93%	97%
BCZYb_FS_15	Hand Press, 6.35 mm (¼") Mold	1600°C (Sinter2)	58%	88%	96%
BCZYb_FS_16	Hand Press, 20 mm Mold	1650°C (Sinter3)	-	91.5%	-
BCZYb_FS_17	Hand Press, 20 mm Mold	1650°C (Sinter3)	-	91.5%	-
BCZYb_FS_18	Hand Press, 20 mm Mold	1650°C (Sinter3)	-	91.5%	-

Initial sintering tests conducted with samples placed directly on porous zirconia plates resulted in a reaction or inter-diffusion between the plate and the sample resulting in a contaminated bottom layer in the samples. To avoid this contamination, future samples were sintered on top of larger pre-sintered disks of the same barium cerate-zirconate composition which were then placed on the porous zirconia plates. It was noticed that the surface layers of the pellets (the layers that were in contact with air during sintering) looked darker or discoloured. To remove any surface contamination or secondary phases caused by secondary reactions or from the evaporation of BaO during the high

temperature sintering process [11,22,81], the surface of the pellets was polished with alumina grit paper (180 and 400 grit).

5.4.4 Conductivity

AC impedance spectra of the samples were analyzed to provide conductivity data. Four Pt wires were connected to the electrodes in pairs in the measurement cell (Figure 8B) for performing AC conductivity experiments. The sintered sample with two identical applied electrodes can be considered a capacitor consisting of two conducting plates (the Pt electrodes) with radius, r , separated by a dielectric medium (the sample) with thickness, d [69]. Dimensions of the sintered samples were used to calculate cell constants as shown in Equation 21 and the normalized conductance calculation is shown in Equation 22:

$$k = \frac{L}{A} = \frac{d}{\pi \cdot r^2} [cm^{-1}] \quad (21)$$

$$\sigma = kG = \frac{k}{R} [S \cdot cm^{-1}] \quad (22)$$

where k is the cell constant, L is the length of the sample which is, in the usual case, equal to the sample thickness, d , and A is the area of the conducting plate used for normalizing the conductance (G) or resistance (R) to calculate conductivity (σ).

The measurement principle (Figure 8C) consisted of applying an alternating voltage (U^*) at a fixed frequency and measuring the resulting current (I^*) that flowed through the sample. The complex impedance of the sample capacitor is equal to the ratio of the applied voltage and output current as shown in Equation 23.

$$Z^* = Z' + iZ'' = \frac{U^*}{I^*} \quad (23)$$

where Z' is the real contribution to the complex impedance and Z'' is the imaginary contribution. The real contribution, Z' , corresponds to resistance, R , and the imaginary contribution corresponds to the capacitance, C [66,69].

Two different approaches can be followed when determining AC conductivity. The first is simply to measure the total conductivity at a fixed frequency (i.e. 50 Hz, 12 kHz and 126 kHz) and the second is to try to deconvolute the data by trying to discern individual contributions to conductivity by interpreting measurements over a wide range of frequencies (i.e., bulk, grain boundary and electrode contributions via equivalent circuit modelling). Typically, electrode contributions may be eliminated from the measurements at sufficiently high frequencies such as 10 kHz if electrode impedance is not too high [64]. The relatively high temperatures in this study (300-900°C) made separating individual conductivity contributions difficult at the lower temperatures and impossible at higher temperatures and, therefore, only the total conductivity was obtained. The total conductivity was sufficient to allow for comparison of effects from the different dopants and atmospheres. The total conductivity is the sum of all of the contributions from the charge carriers present and can thus be written as:

$$\sigma_T = \sigma_H + \sigma_O + \sigma_n + \sigma_h \quad (24)$$

where the total conductivity (σ_T) is the sum of the proton (σ_H), oxygen ion vacancies (σ_O), electron (σ_n) and electron hole (σ_h) conductivities [61,82].

Equations 11 and 12 show the protonic defect formation reactions in the presence of water vapour and hydrogen gas. Equations 13 and 14 show the defect reactions for the formation of p- and n-type defects.

5.4.4.1 Total AC Conductivity

Conductivity tests were performed on three samples of each composition. The second set of measurements was inconsistent due to measurement equipment failure and was discarded. Only one set of results from the BCZY sample was obtained, again, due to measurement equipment failure. The remaining two sets of data for the BCZNd, BCZEu, BCZYb and BCZGd compositions were averaged. Arrhenius plots of the total conductivity for all the compositions in the wet 4% H₂-Ar atmosphere are shown Figure 66. Conductivities increase with temperature as expected.

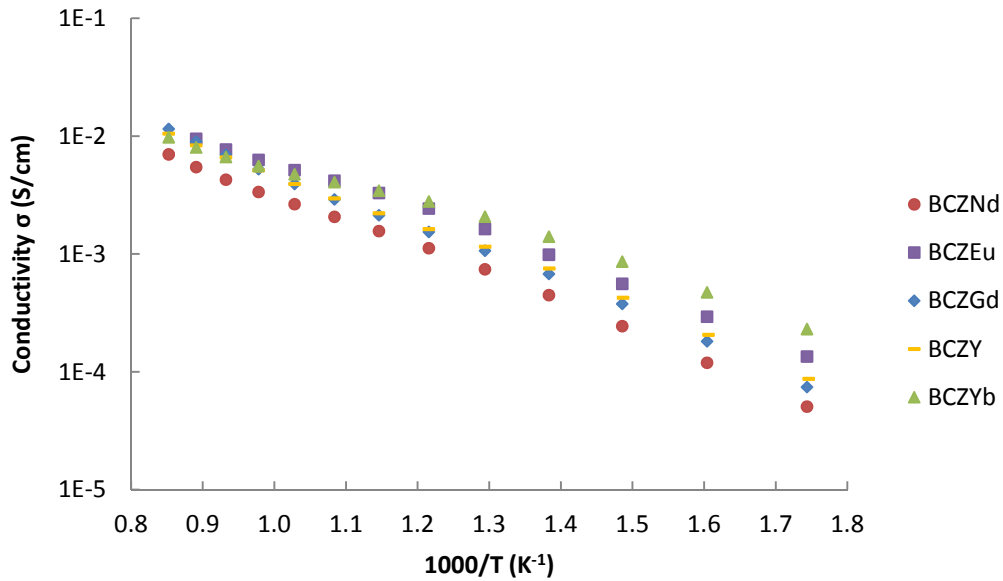


Figure 66: Comparison of total conductivities of the doped samples in wet Ar-4%H₂ measured at 126 kHz

Starting from the lowest temperature at the right (300°C), one can see that the BCZYb composition has the highest conductivity throughout the intermediate

temperature range. BCZEu shows the next highest conductivity in this range with the remaining compositions all slightly lower and all showing a similar trend. BCZNd clearly shows the lowest conductivity. One can see similar trends for relative conductivities when comparing the different compositions in the plots of the conductivity results for the dry Ar/4%H₂ (Figure 67) and dry Ar (Figure 68) atmospheres with the major difference being that BCZY shows the highest conductivity. Other studies on Zr-substituted BaCeO₃ and doped BaCeO₃ have shown similar trends and similar ranges of conductivities [19,26].

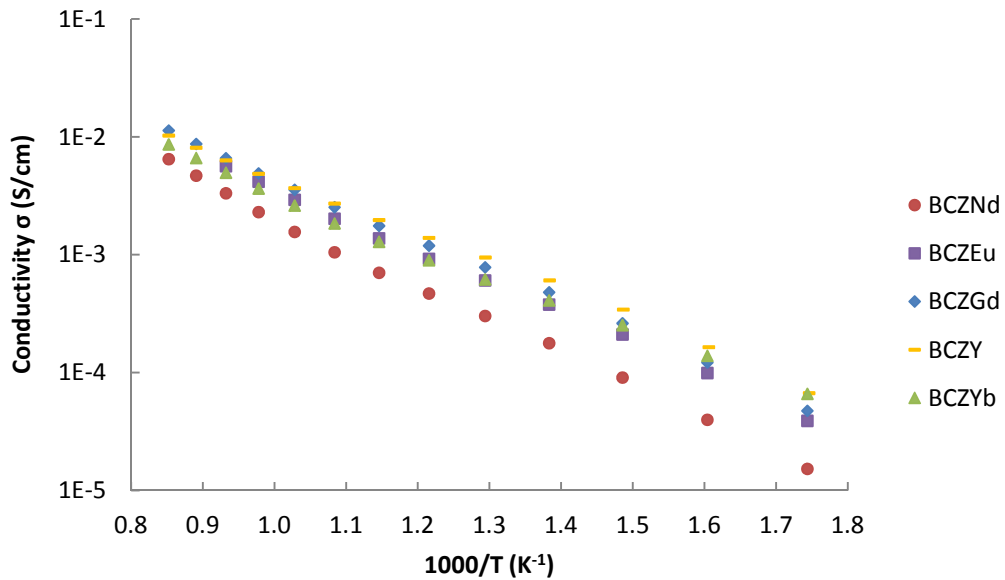


Figure 67: Comparison of total conductivities of the doped samples in dry Ar-4%H₂ measured at 126 kHz

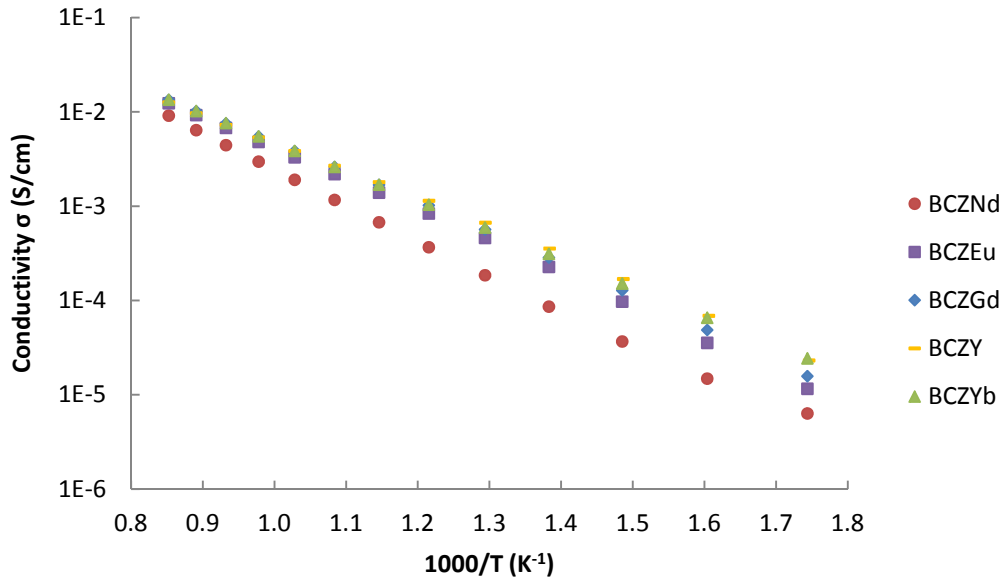


Figure 68: Comparison of total conductivities of the doped samples in dry Ar measured at 126 kHz

The frequency dependence of the AC conductivity is shown in Figure 69. Similar results were obtained for the other compositions which show that there is not a large difference in conductivity values in the range of frequencies from 50 Hz to 126 kHz and that the overall trend for dopant comparison is unchanged.

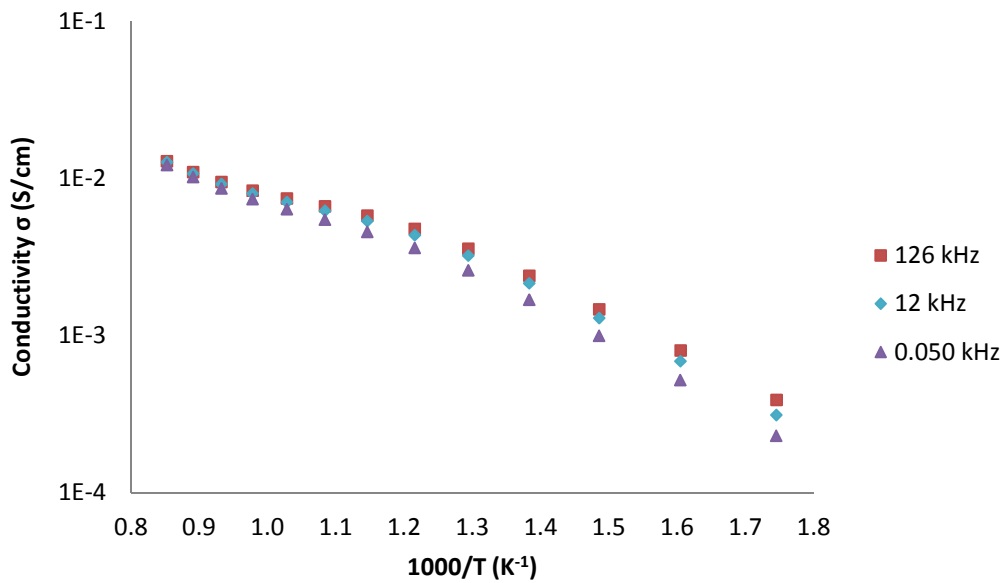


Figure 69: Effect of frequency on measured total conductivity (BCZYb in wet Ar-4% H₂)

When comparing slopes of the plots (i.e., the activation energies), it should be noted that the slopes are not always the same over the entire temperature range. This is especially true for the conductivity plots in the wet Ar/4% H₂ atmosphere. One can see almost completely linear relationships in dry Ar, but increasingly non-linear as hydrogen and finally as both hydrogen and water vapour are present. This could indicate the dominance of one type (or unchanging combination) of conduction mechanism(s) in the dry Ar atmosphere over the entire temperature range and a competition between conducting mechanisms in the other atmospheres. The data in Table 15 show numerically how the differences in conductivity among the atmospheres are the greatest at low temperatures and approach similar values at the highest temperatures studied. The conductivity values for BCZEu at 900°C for the hydrogen containing atmospheres were extrapolated as conductivity readings failed after 800-850°C in the third measurement set. Total conductivities in wet/hydrogen containing atmospheres at 600°C are all around 10⁻³ S/cm, which are close to the values found in the literature for similar compositions [12,19].

Table 15: Conductivities of all compositions in different atmospheres at different temperatures

Composition	Atmosphere	σ @ 300°C (S/cm)	σ @ 600°C (S/cm)	σ @ 900°C (S/cm)
BCZNd	Wet Ar/H ₂	1.89E-05	7.40E-04	6.23E-03
	Dry Ar/H ₂	1.52E-05	7.02E-04	6.47E-03
	Dry Ar	6.35E-06	6.76E-04	9.14E-03
BCZEu	Wet Ar/H ₂	5.00E-05	1.47E-03	1.17E-02*
	Dry Ar/H ₂	3.90E-05	1.38E-03	1.14E-02*
	Dry Ar	1.16E-05	1.40E-03	1.24E-02
BCZGd	Wet Ar/H ₂	7.10E-05	1.98E-03	1.10E-02
	Dry Ar/H ₂	4.73E-05	1.76E-03	1.13E-02
	Dry Ar	1.58E-05	1.69E-03	1.34E-02
BCZY	Wet Ar/H ₂	8.72E-05	2.22E-03	1.05E-02
	Dry Ar/H ₂	2.32E-05	1.80E-03	1.27E-02
	Dry Ar	6.70E-05	1.97E-03	1.03E-02
BCZYb	Wet Ar/H ₂	7.24E-05	1.11E-03	6.68E-03
	Dry Ar/H ₂	6.60E-05	1.29E-03	8.63E-03
	Dry Ar	2.43E-05	1.69E-03	1.35E-02

*extrapolated values

5.4.4.2 Atmospheric Effects

The atmospheric effects on conductivity can be clearly seen in the plot of the conductivities measured in the different atmospheres for BCZYb in Figure 70 (atmospheric comparisons for the other compositions can be found in Appendix II). It can be seen that there are significant differences among the conductivities in the different atmospheres over most of the temperature range. The conductivities for all the compositions over almost the entire temperature range were the highest in wet Ar-4% H₂ atmosphere showing the large contribution of protons to conduction. At temperatures less than ~600°C, the tests in the dry Ar-4% H₂ showed the next highest conductivities, but at temperatures greater than ~600°C, conductivities were higher in dry Ar. This increased high temperature conductivity in dry Ar could be explained by examining the potential oxygen partial pressure difference between dry Ar and dry Ar-4% H₂ atmospheres. At high temperatures, these oxides show significant p-type conduction in the presence of oxygen [26]. At the temperatures tested, any oxygen present in the

hydrogen containing atmosphere would likely react to form water vapour resulting in a lower oxygen partial pressure (but higher water vapour content) and, therefore, lower p-type conduction. It can also be seen that the conductivities in all the atmospheres approach similar values as temperatures approach 900°C. This can be explained by protonic defects being replaced by electron holes and oxygen ion vacancies as temperatures increase [9] and will be discussed further in terms of activation energies.

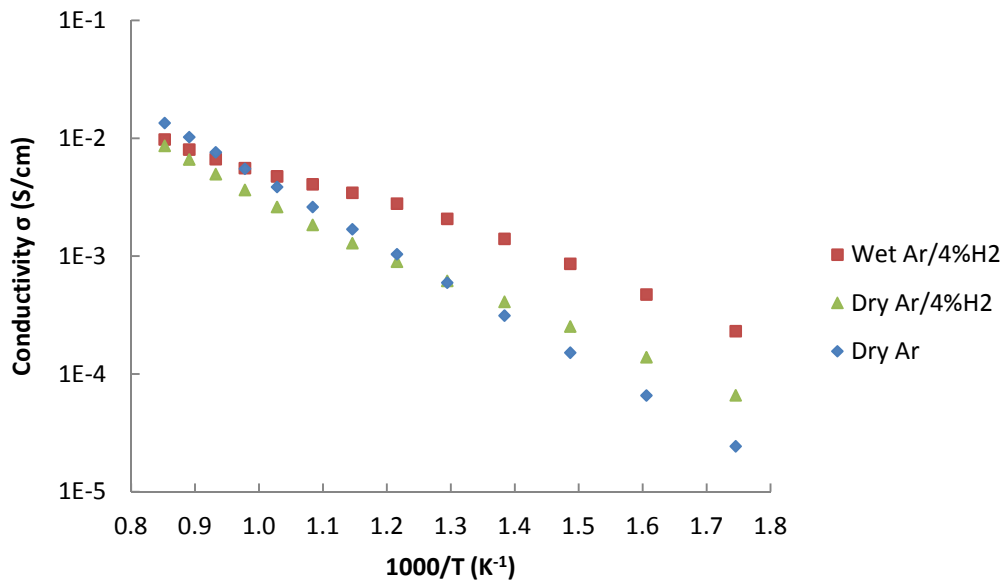


Figure 70: Comparison of total conductivities of BCZYb in different atmospheres measured at 126 kHz

5.4.4.3 Activation Energies

Table 16 shows the activation energies calculated from the linear lower temperature portion of the Arrhenius plots (see Appendix II for plots) as well as the conductivities of each composition in each atmosphere at 600°C. In all cases, the activation energies in the dry Ar atmosphere were the highest, but were lowered with the addition of hydrogen and further lowered by the addition of hydrogen and water vapour. These activation energies are within expected

ranges for barium cerate-zirconates of similar compositions previously studied [12,83]. As expected from the conductivity results, BCZYb showed the lowest activation energies in the low temperature range for the hydrogen containing atmospheres. BCZY had the lowest activation energy in the dry Ar atmosphere and the second lowest activation energies in the hydrogen containing atmospheres.

Table 16: Low temperature activation energies

Composition	Atmosphere	Temperature Range	E* (kJ/mol)	E* (eV)	σ @ 600°C (S/cm)
BCZNd	Wet Ar/H ₂	300-500°C	54	0.56	7.40E-04
	Dry Ar/H ₂	300-500°C	56	0.58	7.02E-04
	Dry Ar	300-500°C	63	0.65	6.76E-04
BCZEu	Wet Ar/H ₂	300-500°C	51	0.52	1.47E-03
	Dry Ar/H ₂	300-500°C	51	0.53	1.38E-03
	Dry Ar	300-500°C	70	0.72	1.40E-03
BCZGd	Wet Ar/H ₂	300-500°C	55	0.57	1.98E-03
	Dry Ar/H ₂	300-500°C	52	0.54	1.76E-03
	Dry Ar	300-500°C	66	0.69	1.69E-03
BCZY	Wet Ar/H ₂	300-500°C	53	0.55	2.22E-03
	Dry Ar/H ₂	300-500°C	49	0.51	1.80E-03
	Dry Ar	300-500°C	62	0.64	1.97E-03
BCZYb	Wet Ar/H ₂	300-500°C	46	0.48	1.11E-03
	Dry Ar/H ₂	300-500°C	41	0.43	1.29E-03
	Dry Ar	300-500°C	66	0.68	1.69E-03

It can be seen that the Arrhenius plots are fairly linear for all atmospheres in the temperature region from 300-500°C. As temperature increases, the hydrogen containing atmospheres deviate from this linear relationship as the slopes plateau slightly in the 550-750°C temperature region before increasing as temperatures reach the maximum. The dry Ar plot shows a linear relationship for the entire temperature range and fairly constant activation energy among the different compositions whereas the other two do not. The transition seen above 500°C for the hydrogen containing atmospheres corresponds to

dehydration of the samples and the resulting competition between decreasing proton conduction and increasing oxygen ion conduction [84–86]. In doped barium cerates, maximum levels of hydration in H₂O containing atmospheres occur at ~200°C [84]. As governed by Equation 11, the maximum levels of hydration also correlate with a maximum concentration of protonic defects within the material. Since the majority of the oxygen ion vacancies are then occupied by hydroxyl ions, and limited long-range oxygen ion vacancy transport can occur [84,87]. Therefore, the transport of protons through the Grotthuss or lone proton transport method must dominate as the vehicle method (the transport of OH⁻ ions) would require the counter diffusion of oxygen ion vacancies (Equation 11). However, as the material begins to dehydrate with increasing temperature, increasing number of free oxygen ion vacancies would exist allowing for increased oxygen ion vacancy diffusion [84]. Increased oxygen ion vacancy mobility also allows for increased proton transport via the vehicle method (all at the expense of lone proton migration) [57,84]. As temperatures increase even further, the material becomes dehydrated and oxygen ion vacancies dominate as positive defects resulting in the predominance of long range oxide ion transport [84]. Thus, the linear conductivity vs. temperature profile in dry Ar can likely be attributed to predominantly the conduction of oxide vacancies and perhaps electron holes. In wet and/or H₂ containing atmospheres, protonic conduction plays the predominant role in low to intermediate temperatures before the onset of dehydration. As temperatures reach maximum and the material becomes completely dehydrated, the conductivity and activation energy converges with those measured in the dry Ar atmosphere suggesting the predominance of oxide ion conduction in all atmospheres at high temperatures.

The addition of H₂O seemed to have a much larger effect on increasing proton transport when compared to simply adding H₂. It is likely that since the

formation of protonic defects in dry H₂ atmospheres required the reduction of lattice oxygens (Equation 12) and not diffusion into oxygen ion vacancies, the material was hydrated to a lesser extent. If the material was not fully hydrated, proton transport via lone proton migration would be more difficult as there would be fewer protonic defects within the material. Thus, even with a likely larger contribution of the vehicle method, oxygen ion vacancies likely played a much larger role as mobile positive defects within the material. The lower total conductivities in the low to intermediate temperature range in dry H₂ atmospheres could then be a function of a greater contribution of oxygen ion conduction, which has a higher activation energy in these types of acceptor doped oxides [12].

Since the dehydration temperature and the amount of water that can be incorporated into the perovskite lattice (via oxygen ion vacancies) increases with trivalent dopant level [84,86], it is likely that increasing the dopant level would lead to more proton conduction over a wider range of temperatures.

Zhang et al. [86] found that for samarium doped barium cerates (BaCe_{1-x}Sm_xO_{3-σ}) in wet 5% H₂/Ar atmospheres, a similar plateau or change of slope transition was found at low samarium concentrations ($x = 0.01-0.10$) at around 500°C, but not at higher samarium concentrations. Although complete samarium solubility was found up to $x = 0.30$, based on its higher conductivity, a samarium level of $x = 0.20$ was found to be the most promising [86]. Thus, it is likely that an increase in trivalent dopant concentrations to around this level would be beneficial to the conductivities of the barium cerate-zirconates studied here although this depends on dopant and atmosphere [85]. Since proton concentration increases with the partial pressure of water in the atmosphere [86], it may also be possible to achieve higher conductivities if the partial pressure of water is increased from the value used here (0.025 atm).

In a study of protonic conductivities of terbium doped strontium cerates, Wei and Lin [88] found higher total conductivity when increasing hydrogen content in a dry atmosphere from 5% to 15%. Given the similar defect chemistry, it is possible that increasing the hydrogen content in the test atmosphere would also increase the conductivity in the doped barium cerate-zirconates.

5.4.4.4 Dopant Effects

A comparison of the conductivity at 600°C versus dopant ionic radii in the wet Ar-4% H₂ atmosphere is shown in Figure 71. It can be seen that the highest conductivity was found for the composition with the dopant with the smallest ionic radius (Yb) and the lowest conductivity was found with the dopant with the largest ionic radius (Nd). In barium cerate type oxides, the increase in dopant trivalent cation ionic radius results in an increased orthorhombic distortion and lowers the proton transport number [89]. A similar distortion is likely present in the barium cerate-zirconate compositions studied here as increasing the ionic radius of the dopant results in a lower perovskite tolerance factor (Figure 58). The highest conductivities were found for the composition with the highest tolerance factor (BCZYb) and the lowest conductivities were found with the composition with the lowest tolerance factor (BCZNd).

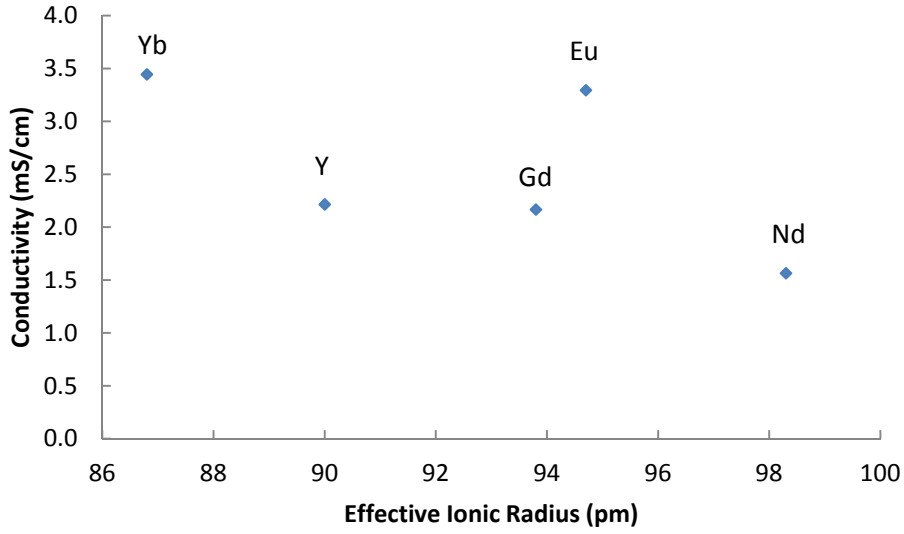


Figure 71: Comparison of total AC conductivities (126 kHz/wet Ar-4% H_2 /600°C) versus ionic radii of the dopants

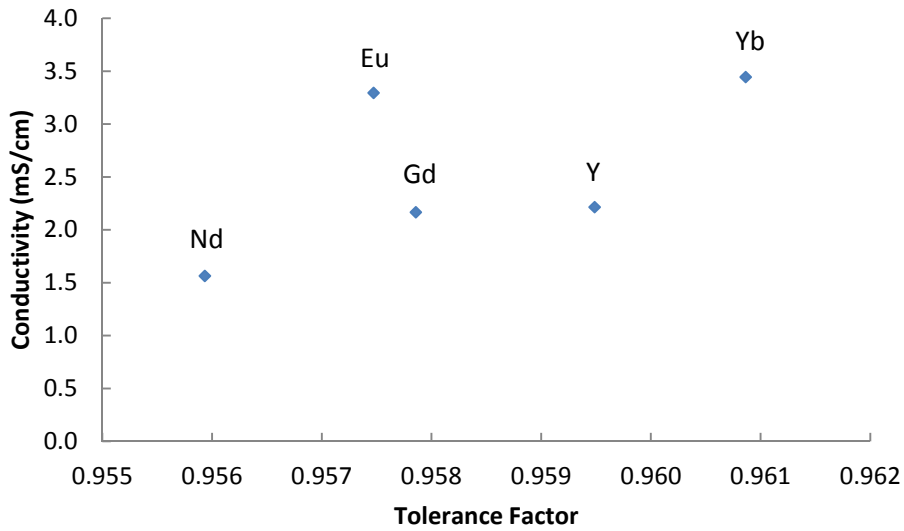


Figure 72: Comparison of total AC conductivities (126 kHz/Wet Ar-4% H_2 /600°C) versus tolerance factors of the doped compounds

Amsif et al. [26] discuss how although the tolerance factor decreases as the ionic radii of the dopant increases, the free volume (lattice cell volume minus the volume of the constituent ions) increases. Therefore, dopants with larger ionic radii resulting in a lower tolerance factor should decrease the ionic mobility, but

a larger free volume should increase the ionic mobility. Amsif et al. predicted and showed that dopant cations with a compromise between high tolerance factors and large free volumes would give the best ionic conductivities in barium cerates. In a comparison of Yb, Y, Gd, Sm, Nd and La as dopants, it was found that Gd-doped compositions of barium cerate resulted in the highest conductivities [26]. However, since a substantial amount of Zr^{4+} is substituted in place of Ce^{4+} in the barium cerate-zirconates, the average ionic radii of the B-site is much lower than in barium cerates. This may result in a requirement for a dopant with a smaller ionic radius than Gd.

In a study on doped barium cerate, Wu et al. [35] found that as the ionic radius of the dopant increases, there is a tendency to partially substitute onto the A-site (Ba) as well as the B-site (Ce). In their study, they found that partial doping on the A-site was unfavourable for small dopants such as Y, Yb and Gd, but becomes favourable for larger dopants such as La. Nd was found to be in the middle of this range with significant distribution over both sites. If a trivalent ion were to dope onto the A-site instead of the B-site, a cation vacancy would result instead of an anion (oxygen) vacancy. Fewer oxygen vacancies would lead to lower hydration, lower proton uptake and lower protonic conductivity [35,84]. Similarly, Haile et al. [90] discuss how that in $ACeO_3 - AZrO_3$ solid solutions (A = Sr or Ba), the decrease in conductivity caused by the introduction of Zr depends on the trivalent dopant used [90]. The impact of Zr addition (on the reduction of conductivity) increases in the order of $Yb \rightarrow Gd \rightarrow Nd$ [90]. Not only does the impact change, but the conductivities were found to follow the same order for a given Zr content [i.e., $\sigma(Yb) > \sigma(Gd) > \sigma(Nd)$] [90]. Therefore, since Yb has the smallest ionic radius and is about the same size as cerium, it does not dope onto the A-site even in the presence of the much smaller Zr^{4+} ion and has no negative effect on conductivity [90]. Figure 71 shows that the conductivities of BCZYb, BCZGd, BCZY and BCZNd follow this trend with the only exception being the

higher conductivity of BCZEu. This suggests that higher conductivities may result for $\text{BaCe}_{0.5}\text{Zr}_{0.4}\text{M}_{0.1}\text{O}_{2.95}$ compositions with the use of dopants with even smaller ionic radii than Yb (eg. Lu^{3+}).

6.0 Summary

Using the solid state synthesis method, yttrium, gadolinium and samarium were successfully doped into the ceria fluorite matrix in various concentrations to form monophasic powders. Using the mixed oxide (MO) variant of the solid state synthesis method for perovskite production, monophasic $\text{BaCe}_{0.90}\text{Y}_{0.10}\text{O}_{2.95}$ powders were produced. The procedure used resulted in difficulties in achieving other monophasic doped cerate powders.

Attempts were made to synthesize dense layers composed of yttrium doped barium, strontium and calcium cerates via screen printing and solid state reaction/sintering of a porous yttrium doped ceria first layer and a BaCO_3 , SrCO_3 or CaCO_3 second layer on NiO-8YSZ and NiO-CGO porous substrates with graded porosity. Both types of substrates studied as potential membrane supports were further processed to achieve a gas tight electrolyte layer of 8YSZ in the case of the NiO-8YSZ substrates and of CGO in the case of the NiO-CGO substrates.

Dense layers of yttrium doped barium cerates were produced on both substrates. On the NiO-8YSZ substrates, extended BaO reaction into the 8YSZ electrolyte layer resulted in a layer of $\text{Ba}(\text{Ce}_{1-x}\text{Zr}_x)_{1-y}\text{Y}_y\text{O}_{3-\delta}$ being formed with the Ce content progressively decreasing further into the substrate. This layer potentially combines the stability of barium zirconate with the higher protonic conductivity of barium cerate. Extended reaction with the CGO electrolyte layer on the NiO-CGO substrates resulted in the synthesis of a gadolinium doped barium cerate layer below the thicker yttrium doped barium cerate layer. Dense layers of yttrium doped strontium cerates were produced only on the NiO-CGO substrates, while again extended reaction into the CGO electrolyte resulted in a gadolinium doped strontium cerate layer. On the NiO-8YSZ substrates, a dense yttria doped zirconate was produced due to preferential reaction with the 8YSZ

electrolyte layer. Dense layers of doped calcium cerate were not produced on either substrate. The stabilities and formation of the perovskites were closely related to the calculated perovskite tolerance factors. The higher the tolerance factor, the more readily the perovskite formed by reaction of the carbonate with the doped ceria layer.

To investigate the potential of combining barium cerates (high conductivity) and zirconates (high chemical stability) with a variety of dopants, near theoretically dense sintered pellets of the composition $\text{BaCe}_{0.5}\text{Zr}_{0.4}\text{M}_{0.1}\text{O}_{2.95}$ (M = Nd, Eu, Gd, Y, Yb) were produced and electrical conductivity was measured under different atmospheres. With slight modifications to the solid state synthesis method used for the doped cerates, including higher reaction temperatures and mixing of the precursor powders using a planetary ball mill, monophasic powders with five different dopants were produced. XRD analyses of the powders reacted at temperatures from 1000-1500°C for 10 h showed that barium cerates and zirconates first form individually and then combine at higher temperatures to form a single phase cubic barium cerate-zirconate. Single phase powders were produced at 1400°C for Gd and Y doped samples, 1450°C for Eu and Nd doped samples, and at 1500°C for Yb doped samples.

Sintering and pressing procedures were found to have a very large effect on final sintered sample quality. Long milling times (24 h), high energy input (>450 rpm) and precise control of powder to liquid ratios (2:1) were required during planetary ball milling to achieve significant particle size reduction for high enough density in the final sintered samples. It is likely that better milling results (i.e., smaller particle size) could be achieved by using smaller milling balls (less than 3 mm in diameter) and industry supplied colloidal milling containers. Powder to mold adhesion was reduced by using a lubricant composed of a 2:1 ratio of odourless kerosene and glyceryl tristearate heated to 60°C and applied

to the mold before the pressing of each pellet. A multistage pressing procedure with a maximum pressure of 138 MPa (20000 psi) produced adequate green densities. Green strength of the pellets was greatly improved with the addition of a binder (PVB) and a plasticizer (butyl benzyl phthalate) to the powders. High sintering temperatures of 1600°C or greater were required to obtain near theoretical densities and these temperatures could possibly be reduced with a more effective milling procedure. Secondary reactions at the high temperatures were a concern and sintering had to be carried out on pre-sintered plates of similar composition to the pressed samples. Samples had to be polished using alumina grit sand paper to remove discoloured surface layers that were in contact with air during the high temperature sintering.

Conductivity tests showed that there are likely multiple conduction processes occurring in the samples including conduction via protons, electron holes and oxygen ion vacancies. In dry argon, low levels of conduction can likely be attributed to oxygen ion vacancies and electron holes. In wet and/or dry hydrogen containing atmospheres, there is a combination of conduction processes which seem to occur over different temperature ranges, with an increase in conductivity versus dry argon at low to intermediate temperatures (300-600°C) suggesting the predominance of a proton conduction contribution. The addition of water vapour and hydrogen to argon increased conductivity by approximately an order of magnitude in the low to intermediate temperature range. Conductivities were increased to a much lesser extent with the addition of hydrogen in a dry atmosphere in this temperature range which suggests that water vapour gave the highest contribution to conduction. This can be attributed to the water dissociating and forming protonic defects within the oxygen deficient samples. At high temperatures in different atmospheres, conductivities and activation energies approach similar values, which is likely due to oxygen ion vacancies becoming an important charge carrier.

Upon comparison of the differently doped compositions, the Yb doped sample had the highest conductivities in the low to intermediate temperature range in the hydrogen containing atmospheres. The Yb doped composition also had the highest calculated tolerance factor which shows it had the best fit within the perovskite lattice (better lattice symmetry) which could possibly explain its high conductivity. It was also discussed how the lower conductivities found in compositions with larger dopant ions (i.e., Nd^{3+}) could be due to partial substitution on the A-site (Ba^{2+}) and the production of cation vacancies. A-site substitution would reduce the number of oxygen ion vacancies and the potential for proton conduction. Since the ionic radius of Yb is very similar to that of Ce, substitution onto the A-site is unlikely resulting in no reduction of oxygen ion vacancies. It is possible that using a dopant with an ionic radius between those of Zr and Ce could result in further improvement of low temperature conductivities.

The activation energies calculated from linear fits to the low temperature range of the Arrhenius plots reinforced the conductivity results. They were the highest in the dry argon atmosphere and the lowest in the wet hydrogen containing atmosphere; however, it was the lowest in the dry hydrogen containing atmospheres with Yb as the dopant. It is possible that increasing the dopant level could result in a higher protonic conductivity over a larger temperature range as more oxygen vacancies would be present leading to more water incorporation. It is also possible that increasing the water vapour and hydrogen content in the atmosphere could also lead to higher protonic conductivities.

7.0 Conclusions

- The layer processing method employed proved to be a good method for producing thin and dense layers of doped barium cerates with the potential for a variety of dopants. The method also showed great potential for the production of thin and dense strontium cerates as well as barium, strontium and calcium zirconates. The formation of dense barium, strontium and calcium zirconate layers occurred at lower temperatures than previously reported for the synthesis of dense sintered samples.
- The dopant used and the powder processing conditions had a large effect on the temperatures required for the production of single phase $\text{BaCe}_{0.5}\text{Zr}_{0.4}\text{M}_{0.1}\text{O}_{2.95}$ powders and dense sintered samples.
- At high temperatures, conduction was dominated by oxygen ion vacancies. At lower temperatures in wet and/or hydrogen containing atmospheres, a distinct and substantial increase in conductivity can be attributed to the increased contribution of proton conduction.
- Dopants with smaller ionic radii resulted in higher conductivities. This could be attributed to higher tolerance factors (higher lattice symmetry) and the reduced likelihood of A-site doping (therefore higher oxygen vacancy concentration).
- $\text{BaCe}_{0.5}\text{Zr}_{0.4}\text{Yb}_{0.1}\text{O}_{2.95}$ seems to be a viable composition for proton conducting fuel cells due to its stability and predominantly protonic conduction in the low to intermediate temperature range in wet hydrogen containing atmospheres.

8.0 Suggestions for Future Work

Ceramic processing and electrochemical testing are very complex processes and there are many areas that can be focused on in future work. Some of these areas include:

- Firstly, conductivity tests of the doped barium cerate-zirconates should be repeated on further samples to confirm results. It would also be beneficial to test conductivities at lower temperatures and lower frequencies so that grain boundary and bulk contributions can be obtained via equivalent circuit modeling.
- Further optimization of the ball milling procedure for particle size reduction of the powders. Instead of using polypropylene jars during planetary ball milling, commercially manufactured colloidal milling containers can be purchased from companies such as RETSCH. Research has shown that with multiple milling steps, smaller milling balls and high rotational speeds, nano-sized particles can be attained [79]. These smaller particles would likely result in higher sinterability and improved density of sintered products.
- In the research described here, 1650°C was the highest available sintering temperature. Although sintering temperatures in this range are already inconveniently high, a slight increase in maximum temperature would be beneficial to densification in further sintering tests. Hopefully, with improved milling procedures, the temperatures required to achieve near theoretical density in barium cerate-zirconate compositions tested here will actually be lowered and higher temperatures will not be required.
- It has been found that the microstructure and electrochemical performance of sintered proton conducting samples are highly dependent on the processing and synthesis method [66]. Future tests

should attempt to control the structure, morphology and grain size of samples through precise processing, manufacturing and sintering techniques. Alternative methods of powder synthesis could be investigated should precise control with the solid state synthesis method described here be unattainable. For example, the freeze drying process for the synthesis of precursor powders described by Amsif et al. [36] was found to be useful in obtaining polycrystalline powders of BaCO_3 at low temperatures that had high reactivity and sinterability.

- It is possible that increasing the dopant level in the barium cerate-zirconate samples could potentially lead to higher conductivities. Future work on these compositions should focus on testing the effects of higher concentrations of Yb dopants (perhaps $\text{BaCe}_{0.5}\text{Zr}_{0.3}\text{Yb}_{0.2}\text{O}_{2.90}$ or $\text{BaCe}_{0.4}\text{Zr}_{0.4}\text{Yb}_{0.2}\text{O}_{2.90}$) on protonic conduction. Previous studies by Ryu and Haile [20] showed that the trivalent dopant used has an effect on the amount of Zr required for stability versus CO_2 . The studies showed that a Nd doped barium cerate-zirconate sample ($\text{BaCe}_{0.7}\text{Zr}_{0.2}\text{Nd}_{0.1}\text{O}_{3-\delta}$) required a lower Zr content for adequate stability compared to one that was doped with Gd ($\text{BaCe}_{0.5}\text{Zr}_{0.4}\text{Gd}_{0.1}\text{O}_{3-\delta}$). Since the addition of Zr to $\text{BaCe}_{1-x}\text{M}_x\text{O}_3$ compounds reduces the protonic conductivity [19], it would be beneficial to use as little Zr as possible to achieve adequate chemical stability. Therefore, the stability of these compounds would have to be studied in order to find the lowest amount of Zr required for adequate stability when the trivalent dopant concentration is increased.
- It would also be interesting to study the effects of using a trivalent dopant with a smaller ionic radius than Yb (i.e., Lu^{3+}). The resulting composition would have a higher tolerance factor than BCZYb (higher lattice symmetry) and an even higher unlikelihood of doping onto the A-site instead of the B-site (higher oxygen vacancy concentration).

- To move forward with the layer synthesis method, it is recommended that the method be further optimized to produce electrolyte layers of the barium cerate-zirconates. The layer synthesis method involved the reaction of alkaline earth carbonates with a doped ceria layer. Research will have to be conducted to determine if a doped ceria-zirconia powder can be synthesized (perhaps based on the $\text{Ce}_2\text{Zr}_2\text{O}_7$ phase detected in the SCY10-2020-YSZ sample) and deposited as a layer to react with barium carbonate. Another possible method for the production of barium cerate-zirconate layers could be based on procedure described by Bi et al. [46]. In the procedure for producing thin and dense $\text{BaCe}_{0.8}\text{Sm}_{0.2}\text{O}_{3-\delta}$ membranes, a well mixed suspension of the precursor powders (BaCO_3 , Sm_2O_3 and CeO_2) was sprayed directly onto a heated anode substrate and reacted in-situ. It is possible that this procedure could be modified to produce electrolyte layers of doped barium cerium-zirconates.

Bibliography

- [1] S. C. Singhal and K. Kendal, "Introduction to SOFCs," in *High Temperature Solid Oxide Fuel Cells: Fundamentals, Design, and Applications*, S. C. Singhal and K. Kendal, Eds. Amsterdam: Elsevier Science, 2003, pp. 1-19.
- [2] S. Yamaguchi, S. Yamamoto, B. Tsuchiya, S. Nagata, and T. Shishido, "Construction of fuel reformer using proton conducting oxides electrolyte and hydrogen-permeable metal membrane cathode," *J. Power Sources*, vol. 145, 2005, pp. 712-715.
- [3] N. Maffei, L. Pelletier, and A. Mcfarlan, "A high performance direct ammonia fuel cell using a mixed ionic and electronic conducting anode," *J. Power Sources*, vol. 175, 2008, pp. 221-225.
- [4] L. Pelletier, A. Mcfarlan, and N. Maffei, "Ammonia fuel cell using doped barium cerate proton conducting solid electrolytes," *J. Power Sources*, vol. 145, 2005, pp. 262-265.
- [5] N. Maffei, L. Pelletier, J. P. Charland, and A. Mcfarlan, "An intermediate temperature direct ammonia fuel cell using a proton conducting electrolyte," *J. Power Sources*, vol. 140, 2005, pp. 264-267.
- [6] N. Maffei, L. Pelletier, J. P. Charland, and A. Mcfarlan, "An ammonia fuel cell using a mixed ionic and electronic conducting electrolyte," *J. Power Sources*, vol. 162, 2006, pp. 165-167.
- [7] N. Bonanos, B. Ellis, K. S. Knight, and M. N. Mahmood, "Ionic conductivity of gadolinium-doped barium cerate perovskites," *Solid State Ionics*, vol. 35, 1989, pp. 179-188.
- [8] S. D. Flint and R. C. T. Slade, "Comparison of calcium-doped barium cerate solid electrolytes prepared by different routes," *Solid State Ionics*, vol. 77, 1995, pp. 215-221.
- [9] K. D. Kreuer, "On the development of proton conducting materials for technological applications," *Solid State Ionics*, vol. 97, 1997, pp. 1-15.
- [10] E. Gorbova, V. Maragou, D. Medvedev, A. Demin, and P. Tsiakaras, "Investigation of the protonic conduction in Sm doped BaCeO₃," *J. Power Sources*, vol. 181, 2008, pp. 207-213.

- [11] K. D. Kreuer, "Proton-conducting oxides," *Annu. Rev. Mater. Res.*, vol. 33, 2003, pp. 333-359.
- [12] E. Fabbri, A. D'Epifanio, E. Di Bartolomeo, S. Licocchia, and E. Traversa, "Tailoring the chemical stability of $\text{Ba}(\text{Ce}_{0.8-x}\text{Zr}_x)\text{Y}_{0.2}\text{O}_{3-\delta}$ protonic conductors for Intermediate Temperature Solid Oxide Fuel Cells (IT-SOFCs)," *Solid State Ionics*, vol. 179, 2008, pp. 558-564.
- [13] H. Iwahara, T. Esaka, H. Uchida, and N. Maeda, "Proton conduction in sintered oxides and its application to steam electrolysis for hydrogen production," *Solid State Ionics*, vol. 3-4, 1981, pp. 359-363.
- [14] P. I. Dahl, R. Haugsrud, H. Lein, T. Grande, T. Norby, and M. Einarsrud, "Synthesis, densification and electrical properties of strontium cerate ceramics," *J. Eur. Ceram. Soc.*, vol. 27, 2007, pp. 4461-4471.
- [15] H. Matsumoto, I. Nomura, S. Okada, and T. Ishihara, "Intermediate-temperature solid oxide fuel cells using perovskite-type oxide based on barium cerate," *Solid State Ionics*, vol. 179, 2008, pp. 1486-1489.
- [16] H. Iwahara, "Technological challenges in the application of proton conducting ceramics," *Solid State Ionics*, vol. 77, 1995, pp. 289-298.
- [17] H. Iwahara, T. Yajima, T. Hibino, K. Ozaki, and H. Suzuki, "Protonic conduction in calcium, strontium and barium zirconates," *Solid State Ionics*, vol. 61, 1993, pp. 65-69.
- [18] J. Lu, L. Wang, L. Fan, Y. Li, L. Dai, and H. Guo, "Chemical stability of doped BaCeO_3 - BaZrO_3 solid solutions in different atmospheres," *J. Rare Earths*, vol. 26, 2008, pp. 505-510.
- [19] K. Katahira, Y. Kohchi, T. Shimura, and H. Iwahara, "Protonic conduction in Zr-substituted BaCeO_3 ," *Solid State Ionics*, vol. 138, 2000, pp. 91-98.
- [20] K. H. Ryu and S. M. Haile, "Chemical stability and proton conductivity of doped BaCeO_3 - BaZrO_3 solid solutions," *Solid State Ionics*, vol. 125, 1999, pp. 355-367.
- [21] S. V. Bhide and A. V. Virkar, "Stability of $\text{AB}'_{1/2}\text{B}''_{1/2}\text{O}_3$ -type mixed perovskite proton conductors," *J. Electrochem. Soc.*, vol. 146, 1999, pp. 4386-4392.

- [22] J. Li, J.-L. Luo, K. T. Chuang, and A. R. Sanger, "Chemical stability of Y-doped Ba(Ce,Zr)O₃ perovskites in H₂S-containing H₂," *Electrochim. Acta*, vol. 53, 2008, pp. 3701-3707.
- [23] Y. Liu, X. Tan, and K. Li, "Mixed conducting ceramics for catalytic membrane processing," *Catalysis Reviews*, vol. 48, 2006, pp. 145-198.
- [24] A. S. Bhalla, R. Guo, and R. Roy, "The perovskite structure - a review of its role in ceramic science and technology," *Mater. Res. Innovations*, vol. 4, 2000, pp. 3-26.
- [25] V. M. Goldschmidt, *Geochemische Verterlungsgesetze der Elemente*, vol. 1-8. Oslo: Kristiania, 1923.
- [26] M. Amsif, D. Marrero-Lopez, J. C. Ruiz-Morales, S. N. Savvin, M. Gabás, and P. Nunez, "Influence of rare-earth doping on the microstructure and conductivity of BaCe_{0.9}Ln_{0.1}O_{3-δ} proton conductors," *J. Power Sources*, vol. 196, 2011, pp. 3461-3469.
- [27] G. Meng, "Preparation and characterization of barium cerate-based thick membranes using a screen printing process," *Solid State Ionics*, vol. 136-137, 2000, pp. 209-213.
- [28] J. M. Serra, V. B. Vert, M. Betz, V. A. C. Haanappel, W. A. Meulenber, and F. Tietz, "Screening of A-substitution in the system A_{0.68}Sr_{0.3}Fe_{0.8}Co_{0.2}O_{3-δ} for SOFC cathodes," *J. Electrochem. Soc.*, vol. 155, 2008, p. B207-B214.
- [29] L. Bi, S. Zhang, B. Lin, S. Fang, C. Xia, and W. Liu, "Screen-printed BaCe_{0.8}Sm_{0.2}O_{3-δ} thin membrane solid oxide fuel cells with surface modification by spray coating," *J. Alloys Compd.*, vol. 473, 2009, pp. 48-52.
- [30] K. Xie, R. Yan, Y. Jiang, X. Liu, and G. Meng, "A simple and easy one-step fabrication of thin BaZr_{0.1}Ce_{0.7}Y_{0.2}O_{3-δ} electrolyte membrane for solid oxide fuel cells," *J. Membr. Sci.*, vol. 325, 2008, pp. 6-10.
- [31] L. Zhang, S. P. Jiang, W. Wang, and Y. Zhang, "NiO/YSZ, anode-supported, thin-electrolyte, solid oxide fuel cells fabricated by gel casting," *J. Power Sources*, vol. 170, 2007, pp. 55-60.
- [32] W. A. Meulenber, J. M. Serra, and T. Schober, "Preparation of proton conducting BaCe_{0.8}Gd_{0.2}O₃ thin films," *Solid State Ionics*, vol. 177, 2006, pp. 2851-2856.

- [33] I. Ahmed, S. M. H. Rahman, P. Steegstra, S. T. Norberg, S.-G. Eriksson, E. Ahlberg, C. S. Knee, and S. Hull, "Effect of co-doping on proton conductivity in perovskite oxides $\text{BaZr}_{0.9}\text{In}_{0.05}\text{M}_{0.05}\text{O}_{3-\delta}$ (M = Yb³⁺ or Ga³⁺)," *Int. J. Hydrogen Energy*, vol. 35, 2010, pp. 6381-6391.
- [34] H. Iwahara, H. Uchida, K. Ona, and K. Ogaki, "Proton conduction in sintered oxides based on BaCeO_3 ," *Journal of the Electrochemical Society: Solid-State Science and Technology*, vol. 135, 1988, p. 529.
- [35] J. Wu, R. A. Davies, M. S. Islam, and S. M. Haile, "Atomistic study of doped BaCeO_3 : dopant site-selectivity and cation nonstoichiometry," *Chem. Mater.*, vol. 17, 2005, pp. 846-851.
- [36] M. Amsif, D. Marrero-López, a. Magrasó, J. Peña-Martínez, J. C. Ruiz-Morales, and P. Núñez, "Synthesis and characterisation of BaCeO_3 -based proton conductors obtained from freeze-dried precursors," *J. Eur. Ceram. Soc.*, vol. 29, 2009, pp. 131-138.
- [37] J. Wu, L. P. Li, W. T. P. Espinosa, and S. M. Haile, "Defect chemistry and transport properties of $\text{Ba}_{x}\text{Ce}_{0.85}\text{M}_{0.15}\text{O}_{3-\delta}$," *J. Mater. Res.*, vol. 19, 2004, pp. 2366-2376.
- [38] M. J. Scholten, J. Schoonman, J. C. van Miltenburg, and H. A. J. Oonk, "Synthesis of strontium and barium cerate and their reaction with carbon dioxide," *Solid State Ionics*, vol. 61, 1993, pp. 83-91.
- [39] T. Hibino, A. Hashimoto, M. Suzuki, and M. Sano, "A solid oxide fuel cell using Y-doped BaCeO_3 with Pd-loaded FeO anode and $\text{Ba}_{0.5}\text{Pr}_{0.5}\text{CoO}_3$ cathode at low temperatures," *J. Electrochem. Soc.*, vol. 149, 2002, p. A1503.
- [40] V. V. Kharton, I. P. Marozau, G. C. Mather, E. N. Naumovich, and J. R. Frade, "Transport numbers and oxygen permeability of $\text{SrCe}(\text{Y})\text{O}_3$ -based ceramics under oxidising conditions," *Electrochim. Acta*, vol. 51, 2006, pp. 6389-6399.
- [41] E. Gorbova, V. Maragou, D. Medvedev, A. Demin, and P. Tsiakaras, "Influence of sintering additives of transition metals on the properties of gadolinium-doped barium cerate," *Solid State Ionics*, vol. 179, 2008, pp. 887-890.
- [42] R. Gerhardt, W.-K. Lee, and A. S. Nowick, "Anelastic and dielectric relaxation of scandia-doped ceria," *J. Phys. Chem. Solids*, vol. 48, 1987, pp. 563-569.

- [43] X. Qi and Y. S. Lin, "Electrical conducting properties of proton-conducting terbium-doped strontium cerate membrane," *Solid State Ionics*, vol. 120, 1999, pp. 85–93.
- [44] S.-J. Song, E. D. Wachsman, S. E. Dorris, and U. Balachandran, "Electrical properties of p-type electronic defects in the protonic conductor $\text{SrCe}_{0.95}\text{Eu}_{0.05}\text{O}_{3-\delta}$," *J. Electrochem. Soc.*, vol. 150, 2003, p. A790.
- [45] M. Elbaccouch, S. Shukla, N. Mohajeri, S. Seal, and A. T-Raissi, "Microstructural analysis of doped-strontium cerate thin film membranes fabricated via polymer precursor technique," *Solid State Ionics*, vol. 178, 2007, pp. 19-28.
- [46] L. Bi, S. Zhang, S. Fang, L. Zhang, K. Xie, C. Xia, and W. Liu, "Preparation of an extremely dense $\text{BaCe}_{0.8}\text{Sm}_{0.2}\text{O}_{3-\delta}$ thin membrane based on an in situ reaction," *Electrochem. Commun.*, vol. 10, 2008, pp. 1005-1007.
- [47] V. Grover, A. Banerji, P. Sengupta, and A. K. Tyagi, "Raman, XRD and microscopic investigations on $\text{CeO}_2\text{-Lu}_2\text{O}_3$ and $\text{CeO}_2\text{-Sc}_2\text{O}_3$ systems: A sub-solidus phase evolution study," *J. Solid State Chem.*, vol. 181, 2008, pp. 1930-1935.
- [48] D. Hassan, S. Janes, and R. Clasen, "Proton-conducting ceramics as electrode/electrolyte materials for SOFC's—part I: preparation, mechanical and thermal properties of sintered bodies," *J. Eur. Ceram. Soc.*, vol. 23, 2003, pp. 221-228.
- [49] F. Chen, O. T. Sørensen, G. Meng, and D. Peng, "Preparation of Nd-doped barium cerate through different routes," *Solid State Ionics*, vol. 100, 1997, pp. 63–72.
- [50] S. Barison, M. Battagliarin, S. Boldrini, G. Chiodelli, L. Doubova, M. Fabrizio, R. Gerbasi, L. Malavasi, and C. Mortalò, "Proton conductors: the role of the synthetic route on their properties," *ECS Transactions*, vol. 11, 2008, pp. 89-96.
- [51] J. Eschenbaum, J. Rosenberger, R. Hempelmann, D. Nagengast, and A. Weidinger, "Thin films of proton conducting SrZrO_3 -ceramics prepared by the sol-gel method," *Solid State Ionics*, vol. 77, 1995, pp. 222-225.
- [52] S. J. Skinner and J. A. Kilner, "Oxygen ion conductors," *Materials Today*, vol. 6, 2003, pp. 30-37.

- [53] H. Hayashi, H. Inaba, M. Matsuyama, N. G. Lan, M. Dokiya, and H. Tagawa, "Structural consideration on the ionic conductivity of perovskite-type oxides," *Solid State Ionics*, vol. 122, 1999, pp. 1-15.
- [54] A. Trovarelli, "Structural properties and nonstoichiometric behavior of CeO₂," in *Catalysis by Ceria and Related Materials*, vol. 2, A. Trovarelli, Ed. Imperial College Press, 2002, pp. 15-50.
- [55] A. Potier, "The hydrogen bond and chemical parameters favouring proton mobility in solids," in *Proton Conductors: Solids, Membranes, and Gels - Materials and Devices*, P. Colomban, Ed. Cambridge, U.K.: Cambridge University Press, 1992, pp. 1-16.
- [56] J. V. Manca, W. Wondrak, K. Croes, W. De Ceuninck, V. D'Haeger, L. De Schepper, and L. Tielemans, "The Arrhenius relation for electronics in extreme temperature conditions," in *HITEN 99. Third European Conference on High Temperature Electronics. (IEEE Cat. No.99EX372)*, 1999, pp. 29-32.
- [57] K. D. Kreuer, "Proton conductivity: materials and applications," *Chem. Mater.*, vol. 8, 1996, pp. 610-641.
- [58] T. Norby, "Proton conduction in oxides," *Solid State Ionics*, vol. 40/41, 1990, pp. 857-862.
- [59] T. Norby, "Solid-state protonic conductors: principles, properties, progress and prospects," *Solid State Ionics*, vol. 125, 1999, pp. 1-11.
- [60] J. M. Serra and W. A. Meulenber, "Thin-film proton BaZr_{0.85}Y_{0.15}O₃ conducting electrolytes: toward an intermediate-temperature solid oxide fuel cell alternative," *J. Am. Ceram. Soc.*, vol. 90, 2007, pp. 2082-2089.
- [61] R. J. Phillips, N. Bonanos, F. W. Poulsen, and E. O. Ahlgren, "Structural and electrical characterisation of SrCe_{1-x}Y_xO₃," *Solid State Ionics*, vol. 125, 1999, pp. 389-395.
- [62] W. A. Meulenber, "Ceramic proton conductors – from materials to application," *WiSe IEF-1 presentation (personal communication)*. Forschungszentrum Jülich, Germany, 2009.
- [63] J. R. Macdonald and W. B. Johnson, "Fundamentals of Impedance Spectroscopy," in *Impedance Spectroscopy: Theory, Experiment, and Application*, Second Edi., E. Barsoukov and J. R. Macdonald, Eds. Hoboken, New Jersey: John Wiley & Sons, Inc., 2005, pp. 1-20.

- [64] *ProboStat™ Manual*. NorECs Norwegian Electro Ceramics AS, 2007.
- [65] W. I. Archer and R. D. Armstrong, "The application of AC impedance methods to solid electrolytes," in *Electrochemistry*, vol. 7, H. R. Thirsk, Ed. London: The Royal Society of Chemistry, 1980, pp. 157–202.
- [66] S. M. Haile, D. L. West, and J. Campbell, "The role of microstructure and processing on the proton conducting properties of gadolinium-doped barium cerate," *J. Mater. Res.*, vol. 13, 1998, pp. 1576-1595.
- [67] FRITSCH Website, "Brief introduction to laser particle size measurement," *FRITSCH GmbH*, 2011. [Online]. Available: http://www.fritsch-laser.de/uploads/media/Brief_Introduction_to_laser_Particle_Size_Measurement.pdf. [Accessed: 20-Jun-2011].
- [68] A. Annapragada, "An analysis of the fraunhofer diffraction method for particle size distribution analysis and its application to aerosolized sprays," *Int. J. Pharm.*, vol. 127, 1996, pp. 219-227.
- [69] M. E. Ivanova, "D-INNER project update," in *D-INNER Presentation (personal communication)*, 2011.
- [70] J. Mertens, "Screen printing diagram," *Institute of Energy and Climate Research, Forschungszentrum Juelich Website*, 2004. [Online]. Available: <http://www2.fz-juelich.de/iwv/iwv1/datapool/page/42/Sieb5.jpg>. [Accessed: 11-Aug-2011].
- [71] K. Takeuchi, C. K. Loong, J. W. Richardson Jr., J. Guan, S. E. Dorris, and U. Balachandran, "The crystal structures and phase transitions in Y-doped BaCeO₃: their dependence on Y concentration and hydrogen doping," *Solid State Ionics*, vol. 138, 2000, pp. 63–77.
- [72] G. Wright and J. Yeomans, "The influence of screen-printing parameters on the microstructure and gas permeance of a zirconia electrolyte," *J. Eur. Ceram. Soc.*, vol. 28, 2008, pp. 779-785.
- [73] S. Wienströer and H. D. Wiemhöfer, "Investigation of the influence of zirconium substitution on the properties of neodymium-doped barium cerates," *Solid State Ionics*, vol. 101, 1997, pp. 1113–1117.
- [74] P. A. Stuart, T. Unno, J. A. Kilner, and S. J. Skinner, "Solid oxide proton conducting steam electrolyzers," *Solid State Ionics*, vol. 179, 2008, pp. 1120-1124.

- [75] T. Schober and H. G. Bohn, "Water vapor solubility and electrochemical characterization of the high temperature proton conductor BaZr_{0.9}Y_{0.1}O_{2.95}," *Solid State Ionics*, vol. 127, 2000, pp. 351–360.
- [76] P. S. Murti and M. V. Krishnaiah, "Investigation of the thermal conductivity of calcium cerate and calcium zirconate," *Mater. Chem. Phys.*, vol. 31, 1992, pp. 347-350.
- [77] R. D. Shannon, "Revised effective ionic radii and systematic studies of interatomic distances in halides and chalcogenides," *Acta Crystallographica Section A: Crystal Physics, Diffraction, Theoretical and General Crystallography*, vol. 32, 1976, pp. 751–767.
- [78] Retsch, "Colloidal grinding," 2005. [Online]. Available: http://www.retsch.com/dltmp/www/2142-041c0f127a4f/tips_colloidal_grinding_en.pdf. [Accessed: 01-Mar-2012].
- [79] Retsch, "Planetary ball mills: extremely fast - extremely fine," *The Sample*. [Online]. Available: http://www.retsch.com/dltmp/www/240951-f15486e80510/tr_sample36_PM_nanogrinding_en.pdf. [Accessed: 01-Mar-2012].
- [80] E. I. Sheinin and N. S. Belostotskaya, "Selecting compositions for coatings to prevent ceramic powders sticking to molds," *Glass and Ceramics*, vol. 24, 1967, pp. 260-261.
- [81] M. Khandelwal, A. Venkatasubramanian, T. R. S. Prasanna, and P. Gopalan, "Correlation between microstructure and electrical conductivity in composite electrolytes containing Gd-doped ceria and Gd-doped barium cerate," *J. Eur. Ceram. Soc.*, vol. 31, 2011, pp. 559-568.
- [82] X. Qi and Y. S. Lin, "Electrical conduction and hydrogen permeation through mixed proton-electron conducting strontium cerate membranes," *Solid State Ionics*, vol. 130, 2000, pp. 149–156.
- [83] S. Ricote, N. Bonanos, and G. Caboche, "Water vapour solubility and conductivity study of the proton conductor BaCe_(0.9-x)Zr_xY_{0.1}O_(3-δ)," *Solid State Ionics*, vol. 180, 2009, pp. 990-997.
- [84] A. Kruth, "Water incorporation studies on doped barium cerate perovskites," *Solid State Ionics*, vol. 162-163, 2003, pp. 83-91.
- [85] N. Bonanos, "Perovskite solid electrolytes: structure, transport properties and fuel cell applications," *Solid State Ionics*, vol. 79, 1995, pp. 161-170.

- [86] C. Zhang, H. Zhao, and S. Zhai, "Electrical conduction behavior of proton conductor $\text{BaCe}_{1-x}\text{Sm}_x\text{O}_{3-\delta}$ in the intermediate temperature range," *Int. J. Hydrogen Energy*, vol. 36, 2011, pp. 3649-3657.
- [87] K. D. Kreuer, E. Schoenherr, and J. Maier, "Proton and oxygen diffusion in BaCeO_3 based compounds: a combined thermal gravimetric analysis and conductivity study," *Solid State Ionics*, vol. 1, 1994, pp. 278-284.
- [88] X. Wei and Y. S. Lin, "Protonic and electronic conductivities of terbium doped strontium cerates," *Solid State Ionics*, vol. 178, 2008, pp. 1804–1810.
- [89] H. Iwahara, T. Yajima, and H. Ushida, "Effect of ionic radii of dopants on mixed ionic conduction ($\text{H}^{++}\text{O}_2^-$) in BaCeO_3 -based electrolytes," *Solid State Ionics*, vol. 70-71, 1994, pp. 267-271.
- [90] S. M. Haile, G. Staneff, and K. H. Ryu, "Non-stoichiometry, grain boundary transport and chemical stability of proton conducting perovskites," *J. Mater. Sci.*, vol. 6, 2001, pp. 1149 - 1160.

Appendix I: EDX Analysis

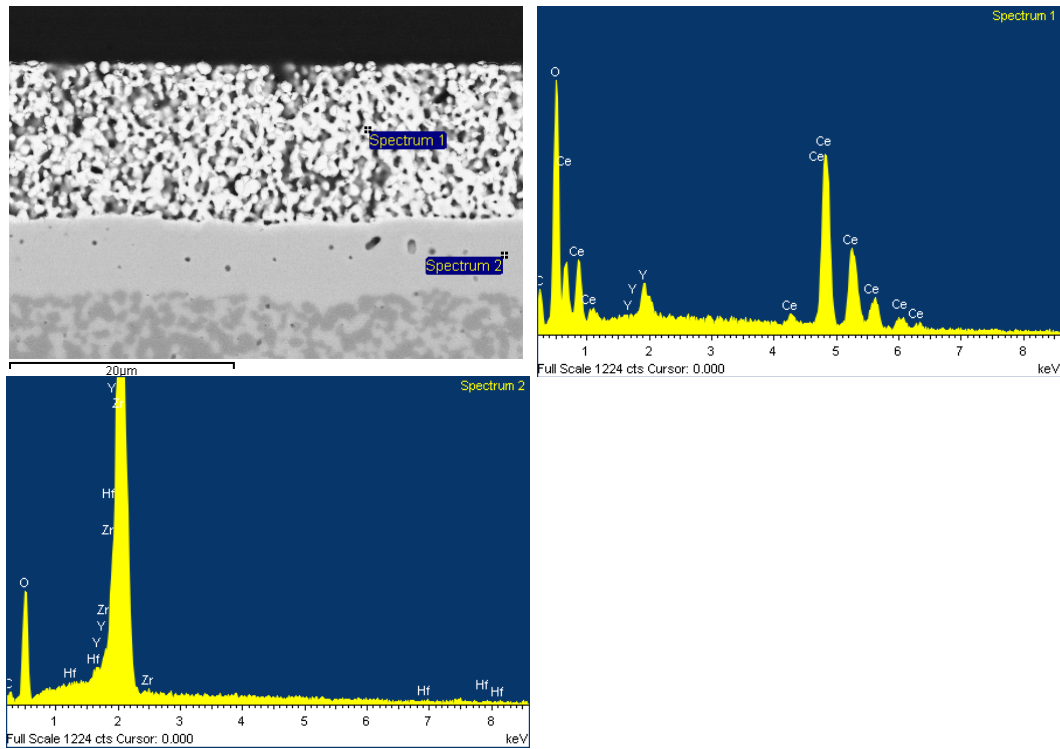


Figure 73: EDX analysis of sample CeY10-YSZ

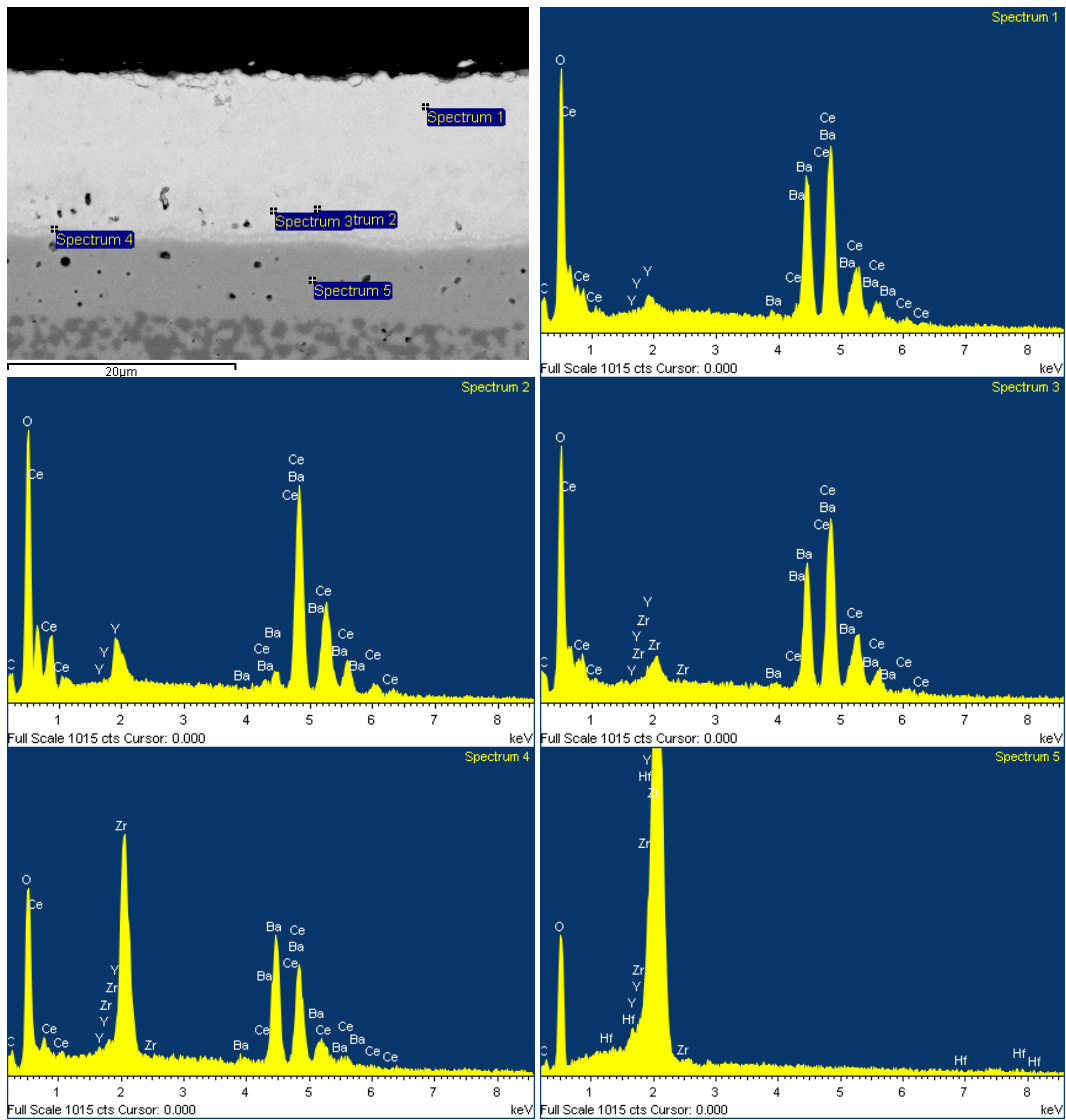


Figure 74: EDX analysis of sample BCY10-2020-YSZ

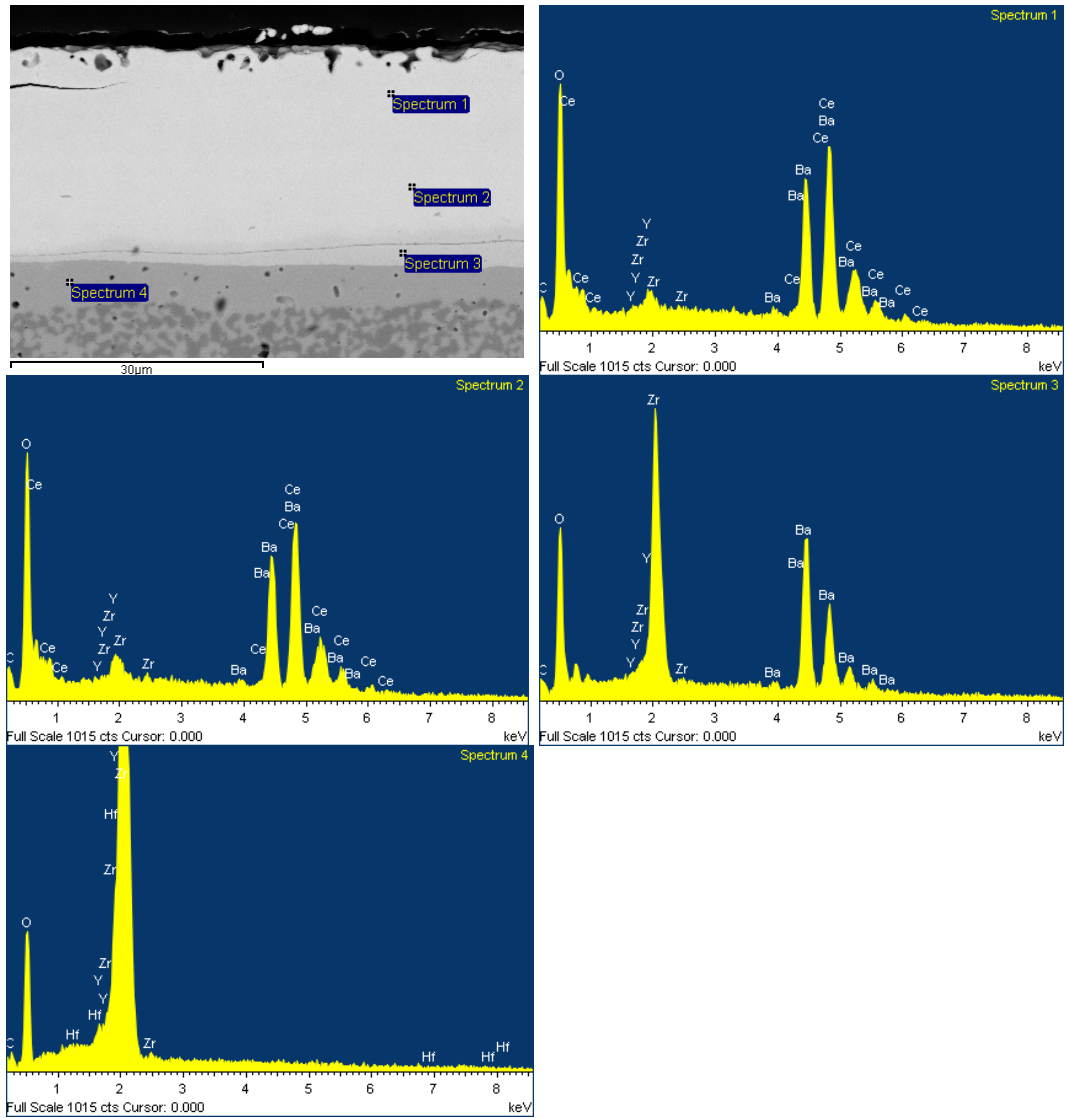


Figure 75: EDX analysis of sample BCY10-2040-YSZ

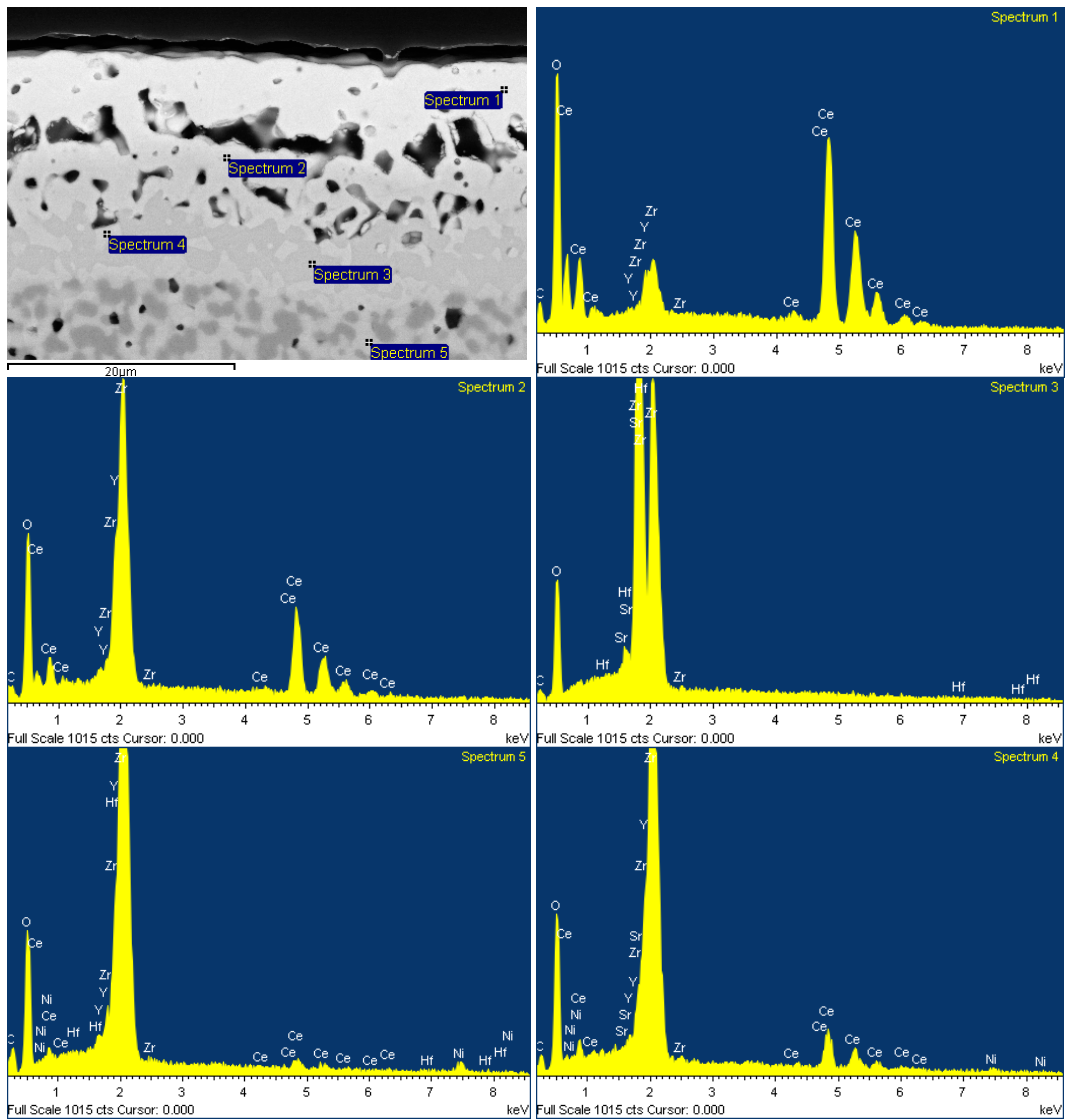


Figure 76: EDX analysis of sample SCY10-2020-YSZ

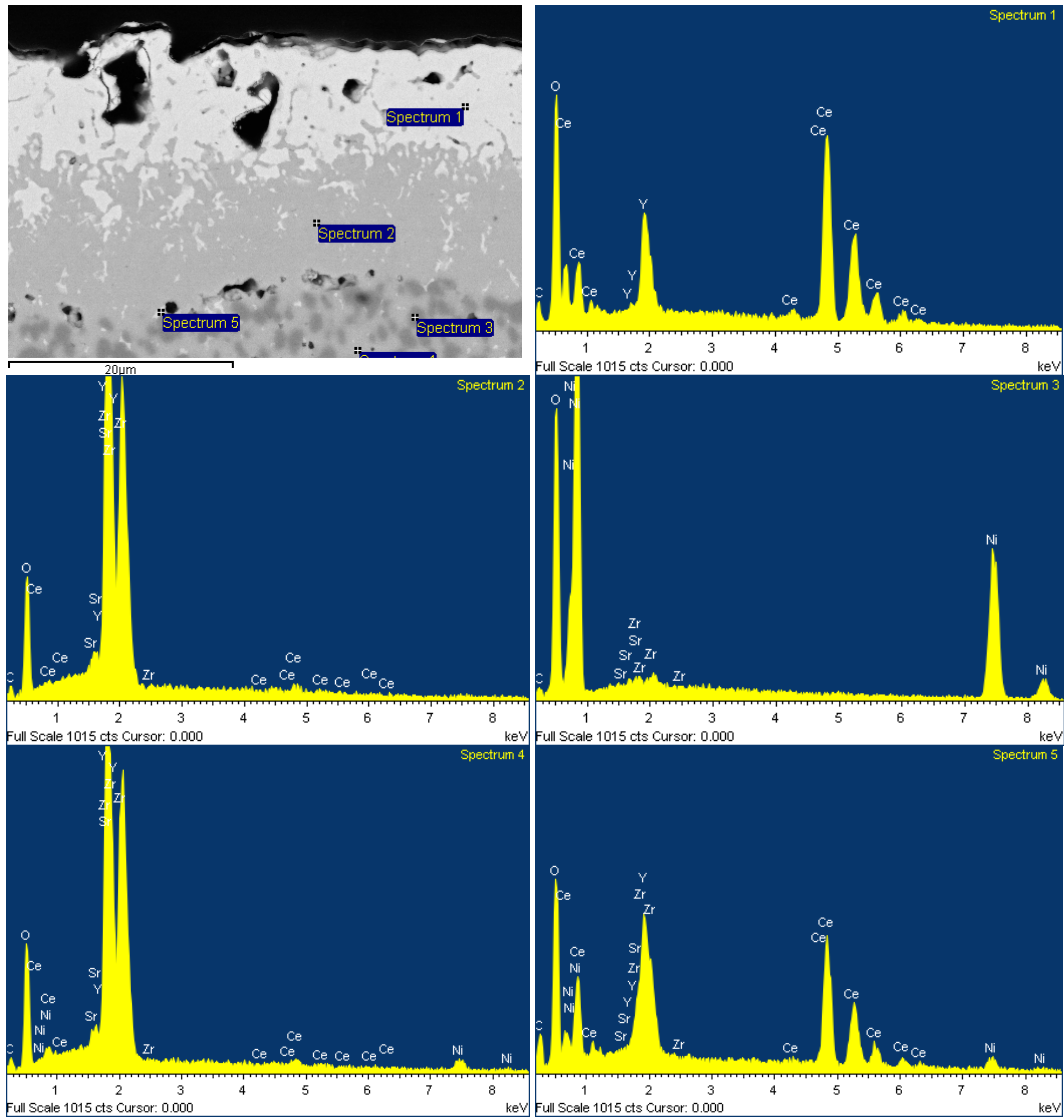


Figure 77: EDX analysis of sample SCY10-2040-YSZ

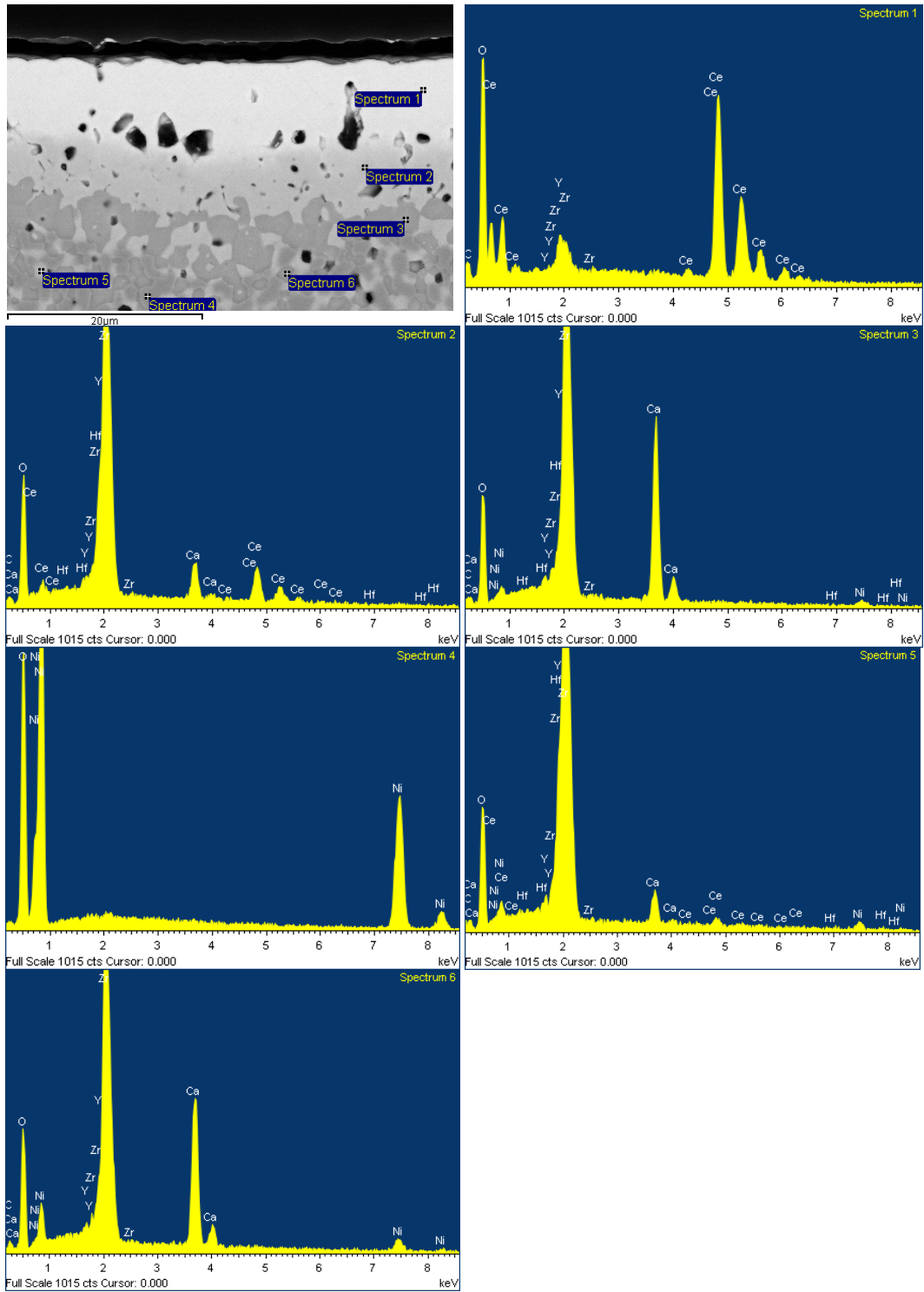


Figure 78: EDX analysis of sample CCY10-2020-YSZ

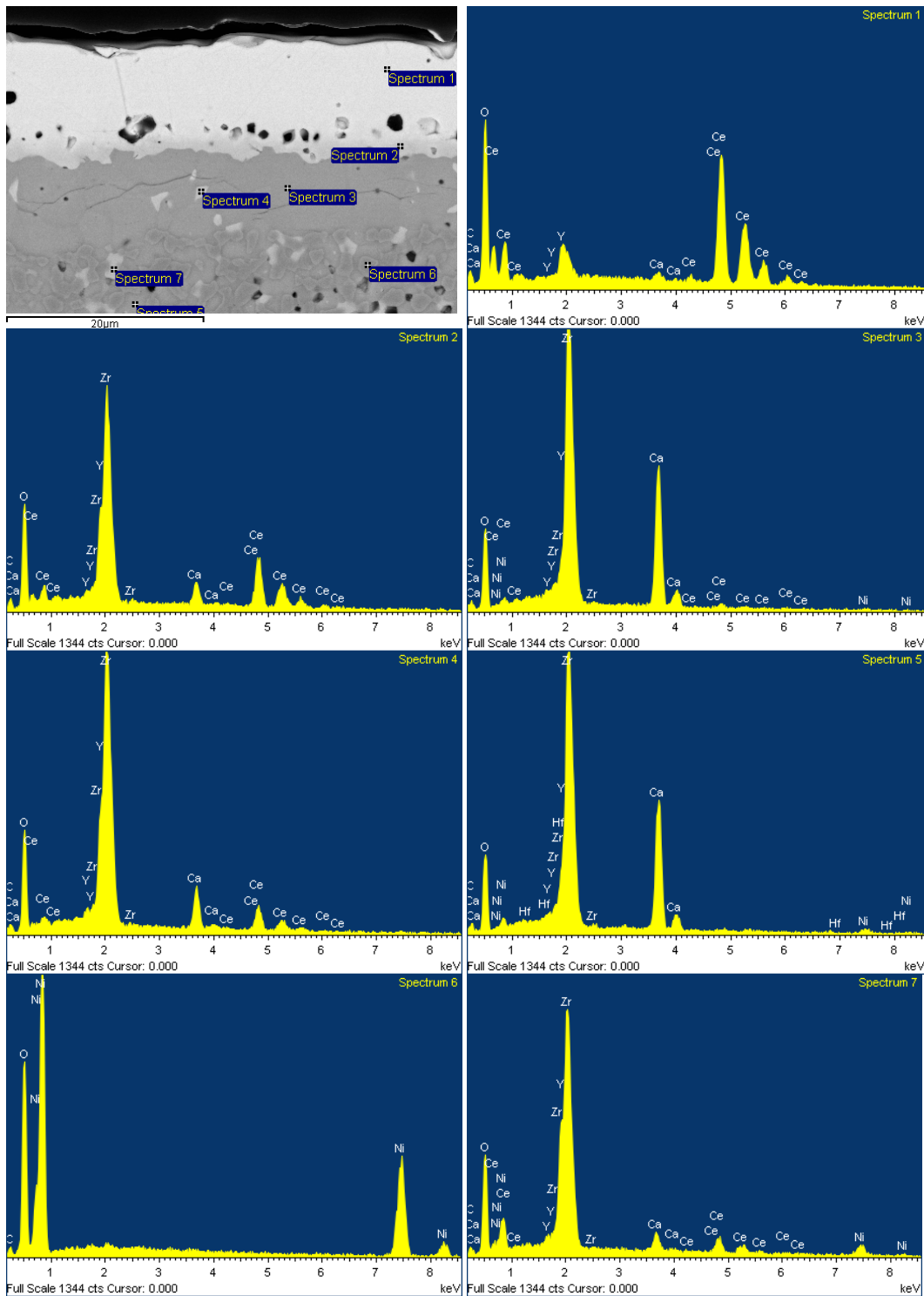


Figure 79: EDX analysis of sample CCY10-2040-YSZ

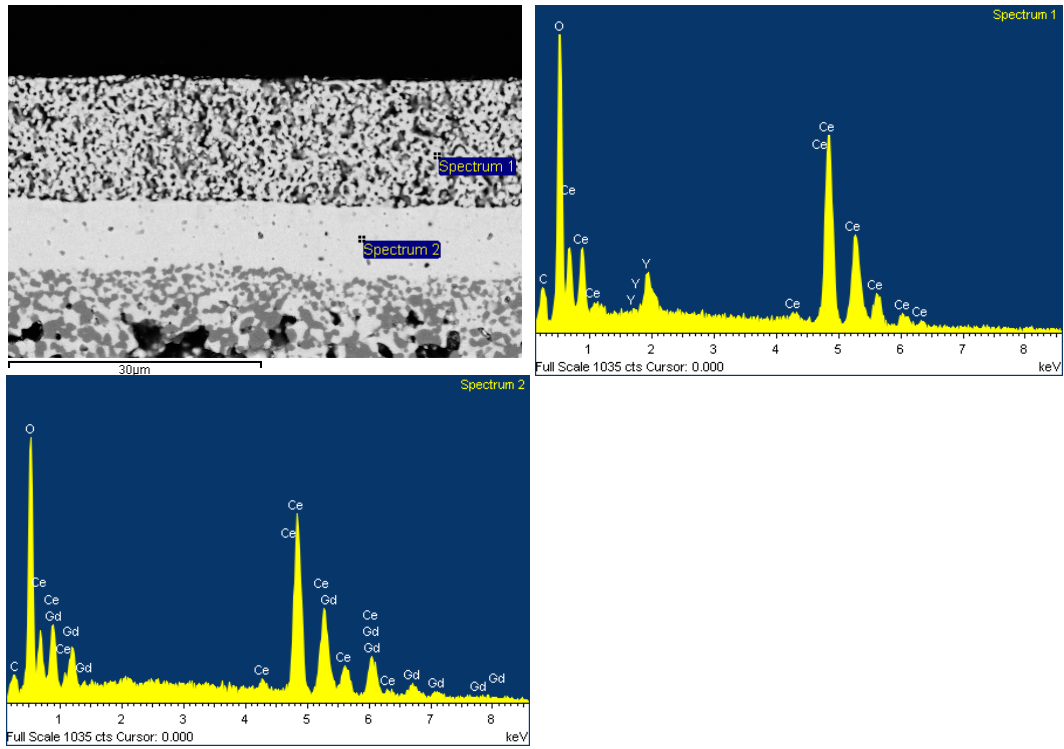


Figure 80: EDX analysis of sample CeY10-CGO

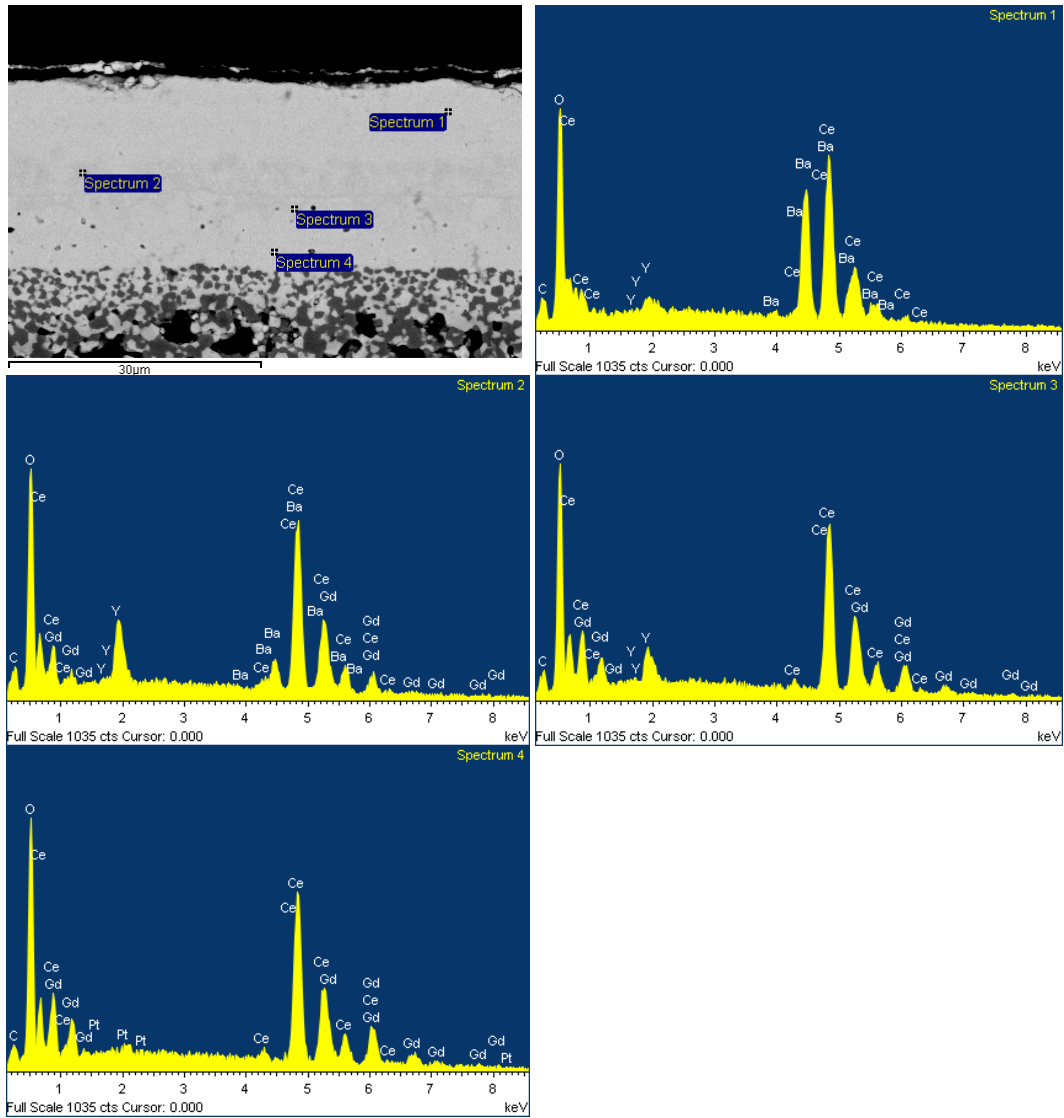


Figure 81: EDX analysis of sample BCY10-2020-CGO

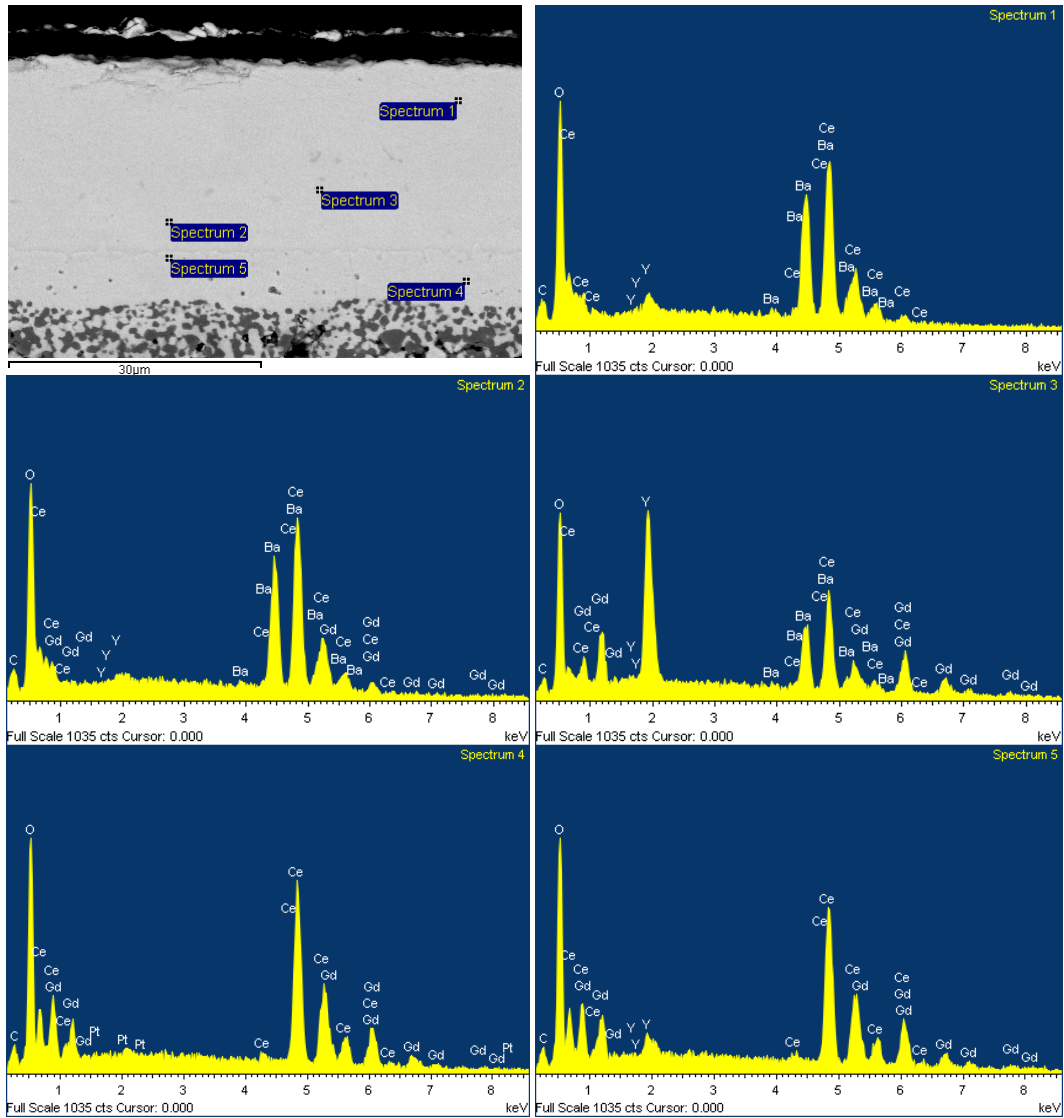


Figure 82: EDX analysis of sample BCY10-2040-CGO

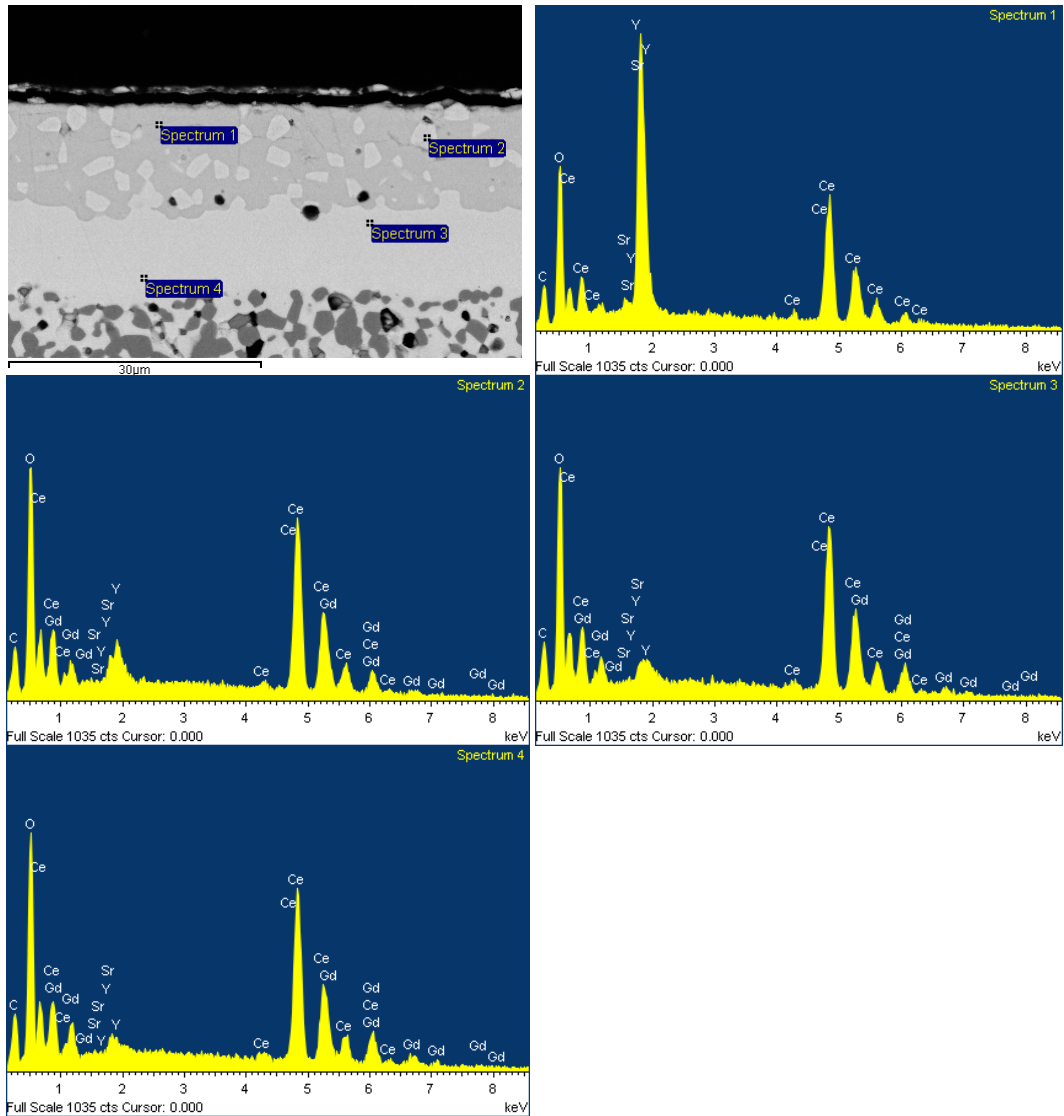


Figure 83: EDX analysis of sample SCY10-2020-CGO

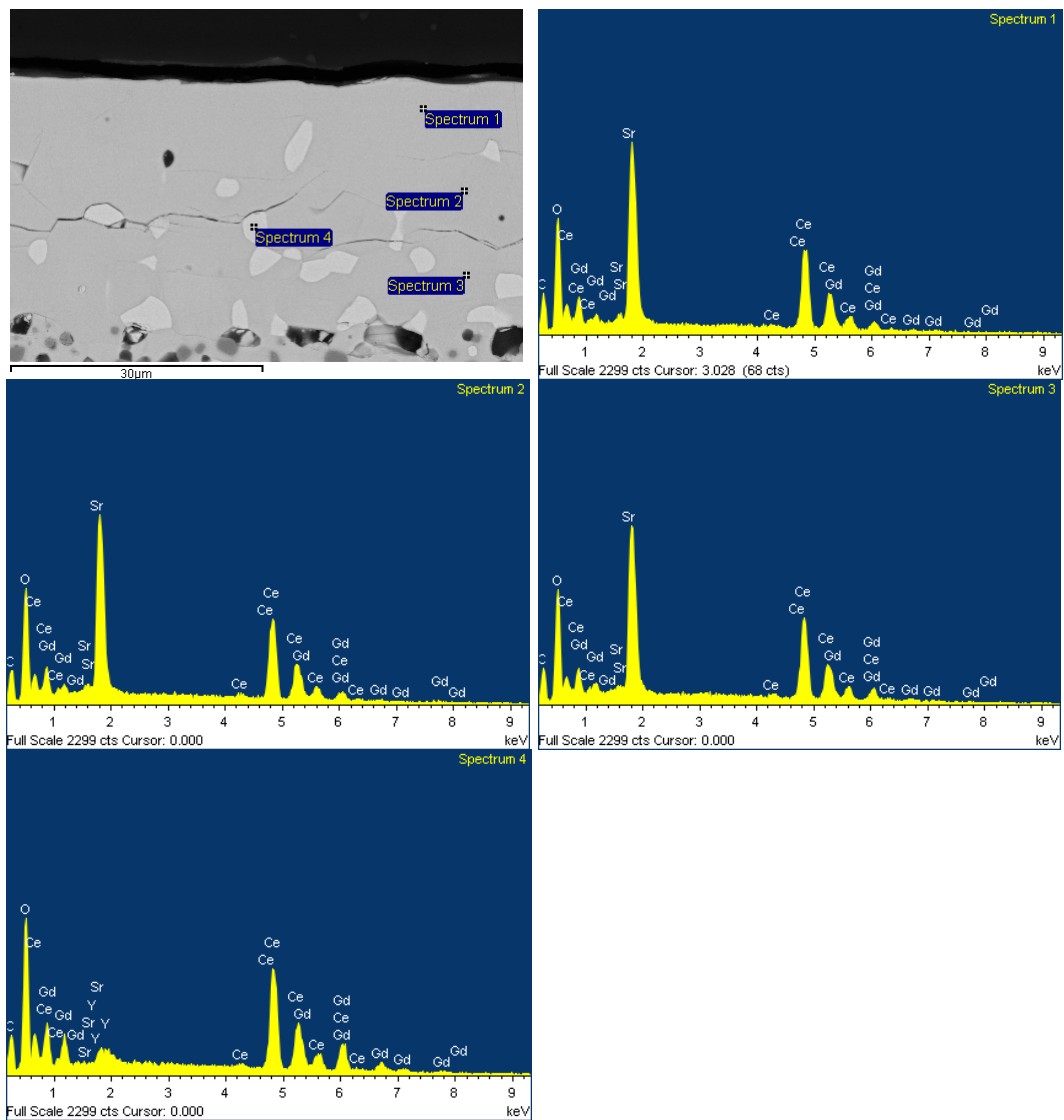


Figure 84: EDX analysis of sample SCY10-2040-CGO

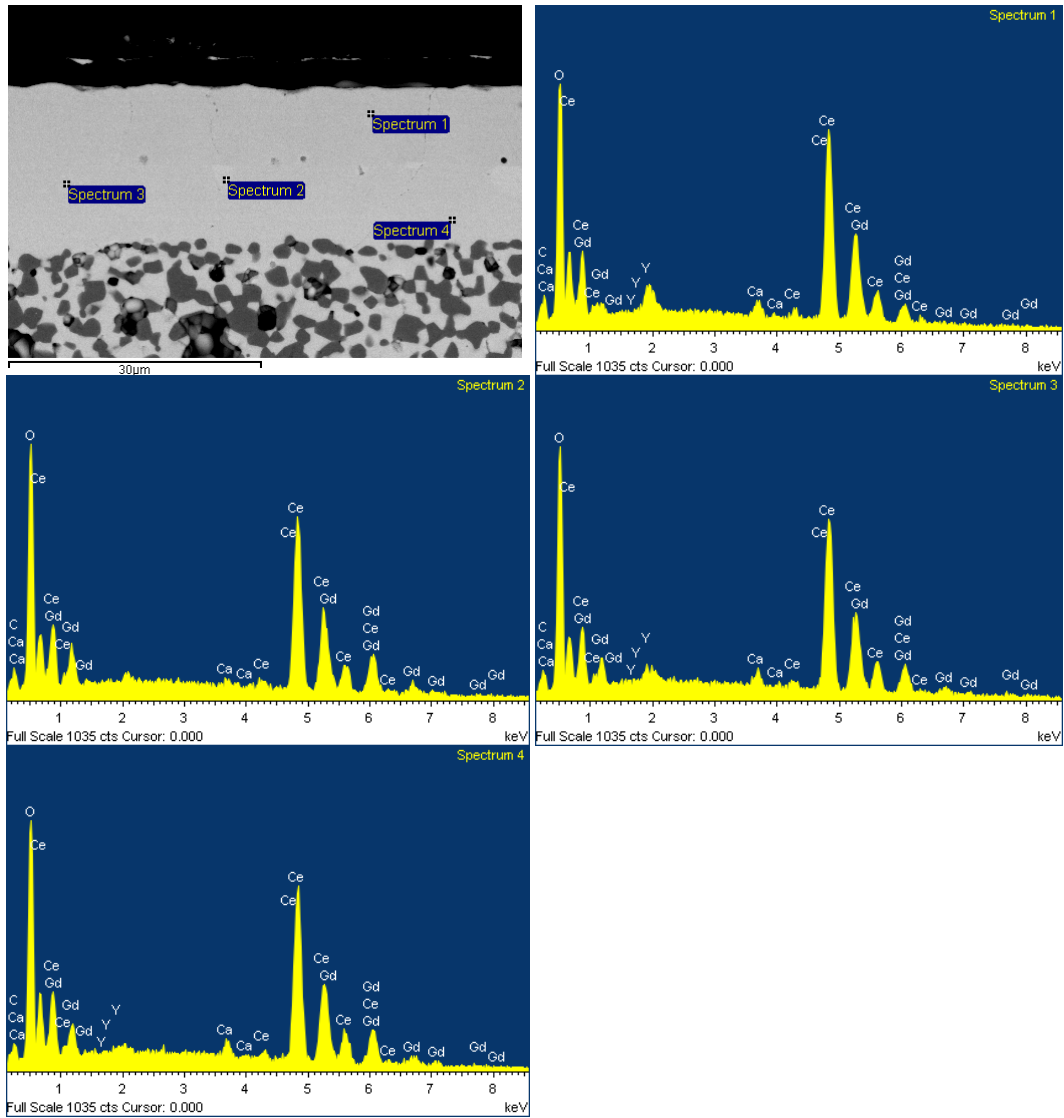


Figure 85: EDX analysis of sample CCY10-2020-CGO

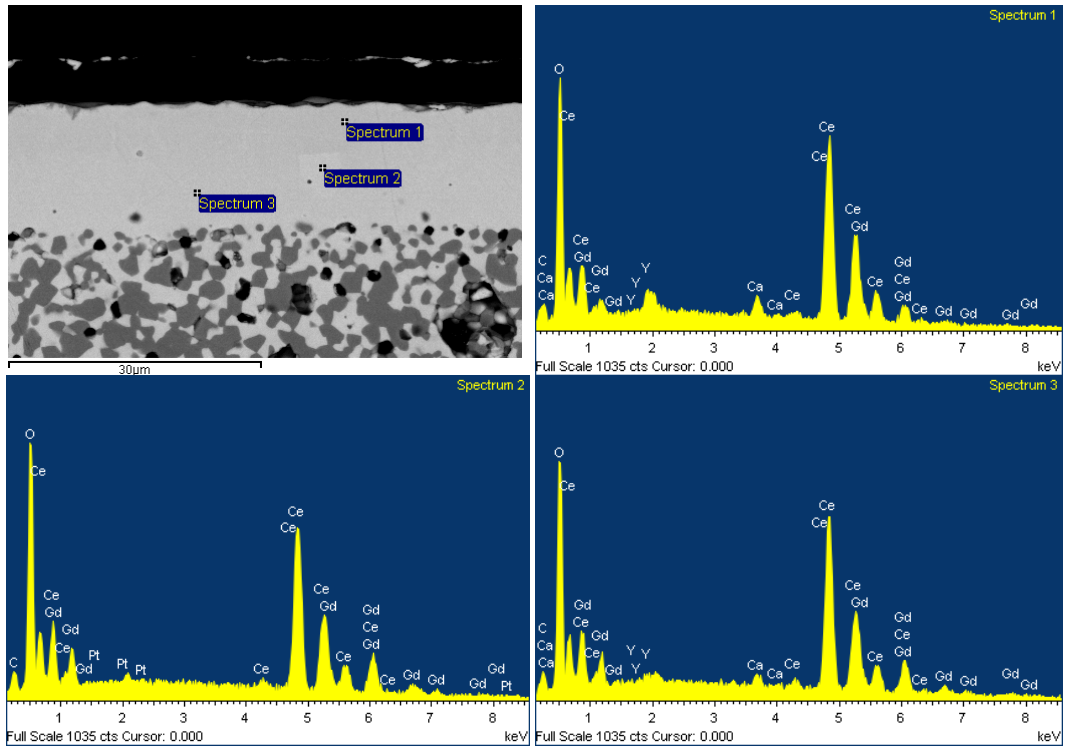


Figure 86: EDX analysis of sample CCY10-2040-CGO

Appendix II: Additional Conductivity and Impedance Data

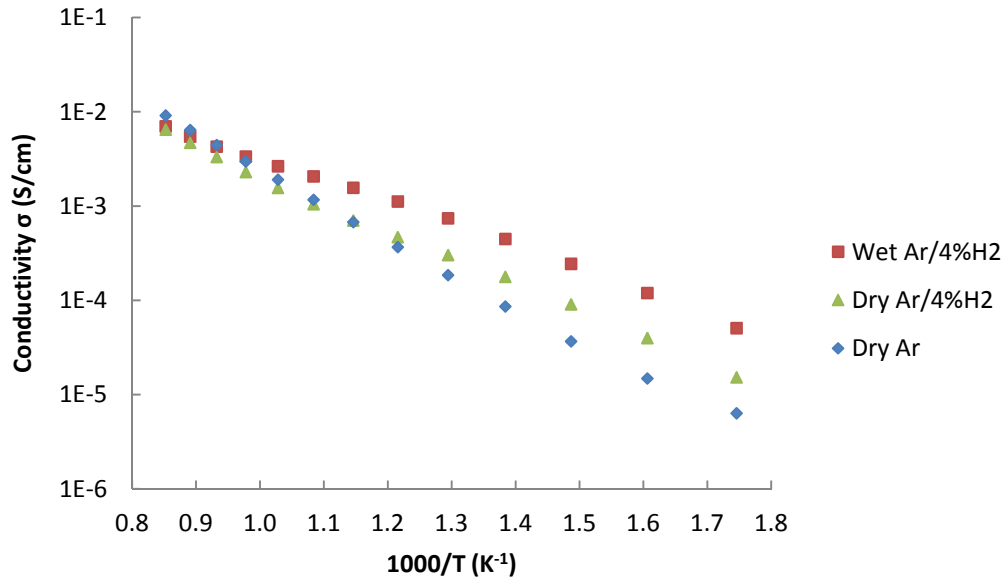


Figure 87: AC conductivities of BCZNd in different atmospheres measured at 126 kHz

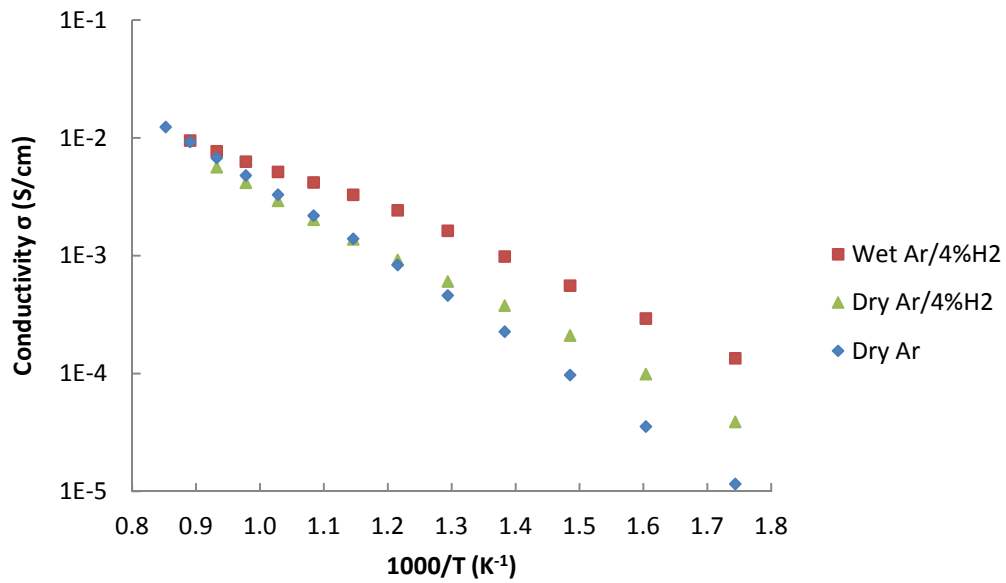


Figure 88: AC conductivities of BCZEu in different atmospheres measured at 126 kHz

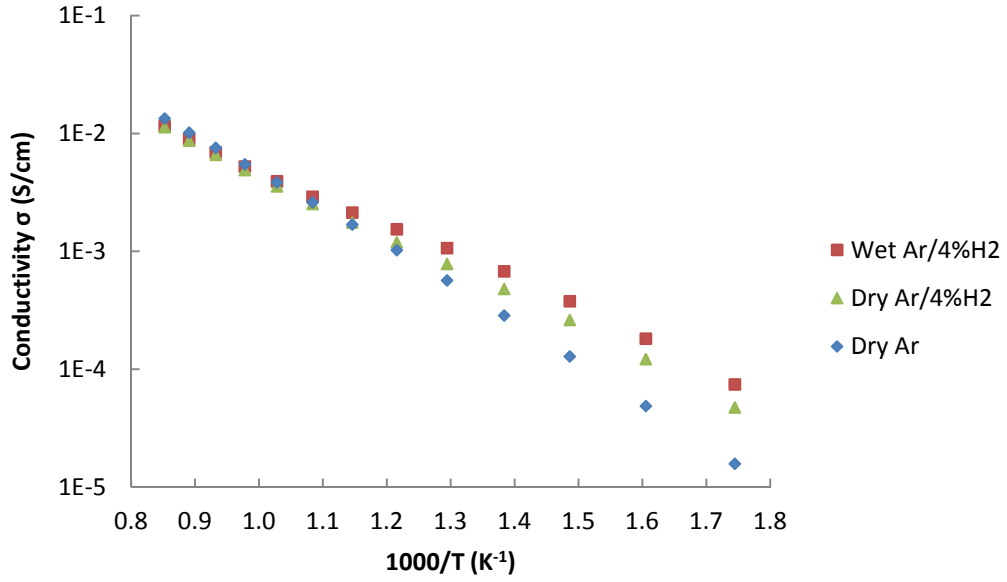


Figure 89: AC conductivities of BCZGd in different atmospheres measured at 126 kHz

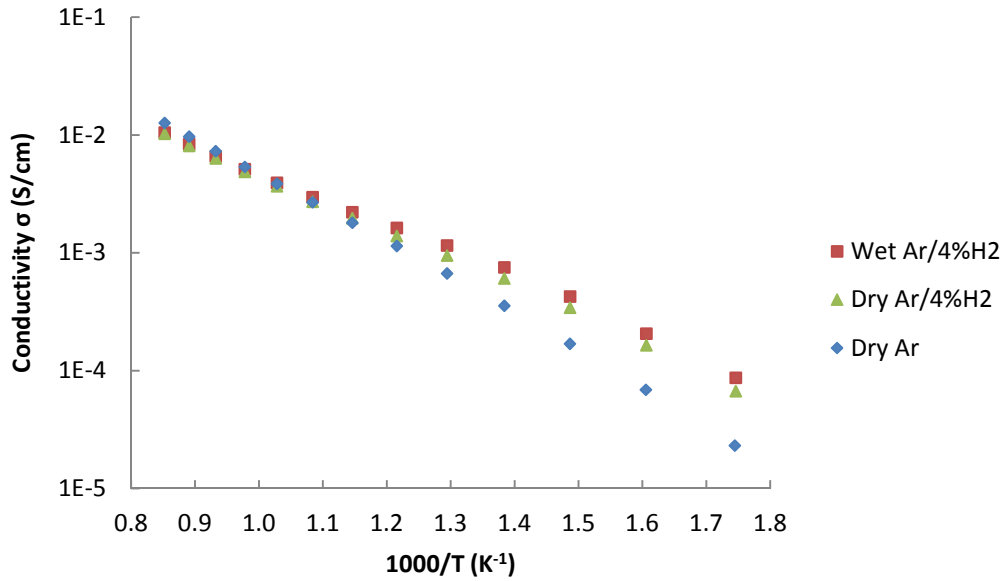


Figure 90: AC conductivities of BCZY in different atmospheres measured at 126 kHz

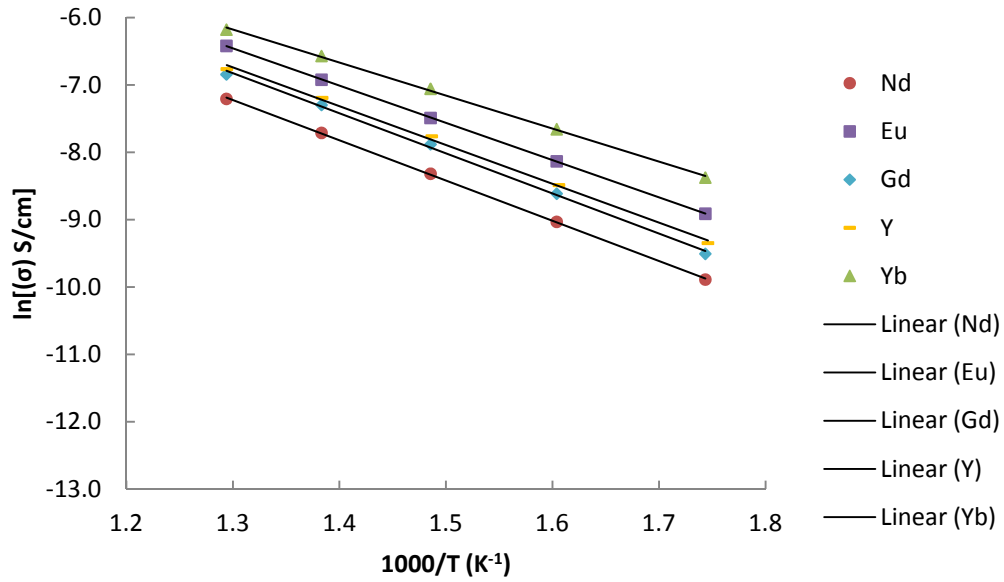


Figure 91: Low temperature conductivities at 126 kHz in wet Ar/4% H₂

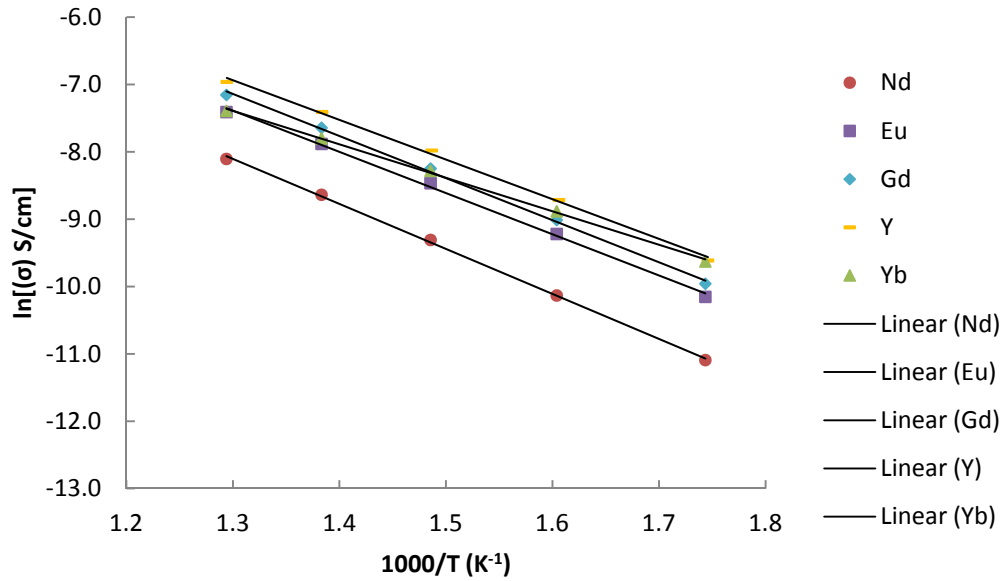


Figure 92: Low temperature conductivities at 126 kHz in dry Ar/4% H₂

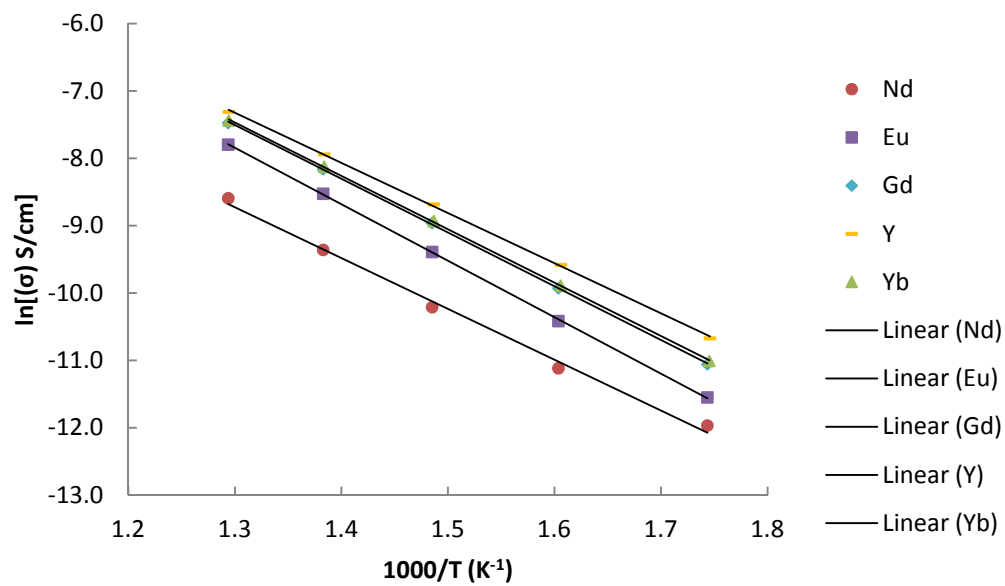


Figure 93: Low temperature conductivities at 126 kHz in dry Ar